Electric field control of magnetic anisotropy and domail wall motion

van den Brink, A.

Award date:
2012

Eindhoven University of Technology
Department of Applied Physics
Group Physics of Nanostructures (FNA)

Electric field control of magnetic anisotropy and domain wall motion

A. van den Brink
April, 2012

Supervisors:

ir. A.J. Schellekens
prof.dr.ir. B. Koopmans

Abstract

Modern magnetic devices generally employ either magnetic fields or electric currents to change the magnetisation direction. A novel third method of magnetisation manipulation was discovered recently: experiments have shown that *electric fields* can affect magnetic properties in thin film systems. This provides new technological possibilities, and could lead to ultra-low power magnetic devices.

The application of electric fields was found to significantly modify the domain wall creep velocity in thin magnetic films; a phenomenon previously unreported in the literature. This velocity modification was linked to an anisotropy modification using creep theory. The magnetic anisotropy was found to vary linearly as a function of the applied voltage, at -1.9 % per applied V/nm for a Pt/Co(1 nm)/Al_2O_3(3.8 nm)/Pt junction. This corresponds to an electric field induced anisotropy modification of $-14 \pm 2\,\mathrm{fJV^{-1}m^{-1}}$, comparable to similar data reported in the literature. Based on the leakage current magnitude and symmetry arguments, heating and magnetic field-like effects were excluded as the origin of the observed effect, which was therefore attributed unambiguously to the electric field.

A ligand field model of interfacial anisotropy in thin films was extended to include electric field effects. This model produced an estimated order of magnitude of such effects that agrees with both the experimental findins and more advanced calculations in the literature.

The electric field effect was found to be larger in a Pt/$Co_{68}B_{32}$(0.8 nm)/Ta_2O_5(7 nm)/Pt junction, which allowed for control of the domain wall velocity over an order of magnitude. Comparison to anisotropy modification values reported in the literature suggests that voltage control of the domain wall velocity should be possible over many orders of magnitude. This creates exciting new prospects for spintronics applications.

Contents

Chapter 1

Introduction

Advances in information technology have transformed the modern world, affecting the way we live and work. The ever-growing demand for computing power and storage capacity has fuelled tremendous scientific research efforts, developing new technologies and fundamental insights at the same time. The research goal remains to make devices faster, smaller, cheaper, and less power consuming.

A striking example of the advances made over the past decades is found in storage applications. Since the introduction of the first hard disk drive (HDD) in 1956, storing 3.75 megabytes in a volume of roughly two refrigerators, the data density has grown formidably. Present-day HDDs store terabytes of information in the volume of a pack of butter. This would not have been possible without the discovery of the giant magnetoresistance (GMR) effect in 1988 [1, 2], enabling the detection of magnetic bits at the scale of nanometres. The discovery of the GMR effect gave rise to an exciting new research field; that of spintronics.

1.1 Spintronics

Spintronic devices make use of two properties of electrons; the *charge* and the *spin*. The quantum-mechanical concept of spin can semi-classically be viewed as rotation of an electron around its central axis. Movement of electric charge induces a magnetic field; electrons thus carry an intrinsic magnetic moment associated with their spin. Macroscopic alignment of electron spins in certain materials causes the well-known phenomenon of ferromagnetism. In spintronics, both charge and spin are exploited in the storage and manipulation of ferromagnetic bits of information. The GMR effect, for instance, arises from spin-dependent scattering of conduction electrons in magnetic multilayers. The similar tunnelling magnetoresistance (TMR) effect is used in all modern HDD read heads, determining the orientation of magnetic bits through a simple resistance measurement.

One of the more recent technological goals in spintronics is to create magnetic

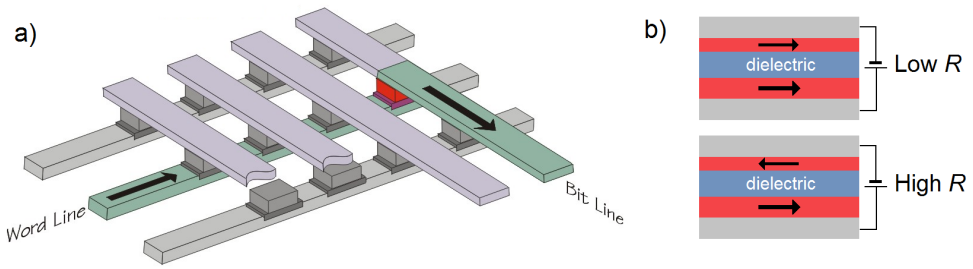

Figure 1.1: *a) Basic layout of a magnetic random access memory. A grid of metallic leads allows for individual bits to be addressed. b) Individual bits consist of two magnetic layers separated by a dielectric barrier: a magnetic tunnel junction (MTJ). The resistance of an MTJ depends on the relative orientation of the two magnetisations; the TMR effect. Applying a large current can change a bit's magnetisation through STT.*

random access memory (MRAM), storing information in an array of magnetic bits as depicted in Fig. 1.1. A common scheme uses magnetic tunnel junctions (MTJs): two magnetic layers separated by a dielectric barrier. The resistance of such an MTJ depends on the relative orientation of the magnetisation directions (the TMR effect) allowing for binary information to be stored. Reading and writing are both achieved using currents: a strong spin-polarised current can change a layer's magnetisation through spin-transfer torque (STT) [3], while smaller currents can read out the magnetic state using TMR. Compared to capacitor-based random access memory, MRAM provides non-volatility (data retention when powered down) and a great reduction in power consumption, while offering similar reading and writing speeds. Furthermore, in permanent storage applications, MRAM features a much faster and non-destructive writing process than Flash memory [4]. For these reasons, MRAM and spintronics in general have attracted great scientific and commercial interest since the 1990s.

An interesting alternative approach to magnetic storage is the magnetic racetrack memory (MRM), proposed by IBM in 2006 [5, 6], depicted in Fig. 1.2. The key concept of this device is that many bits of information are stored in a single magnetic wire. Individual bits are represented by magnetic domains; regions of material magnetised in a specific direction representing either a '0' or a '1'. The interface between two neighbouring domains, a domain wall (DW), can be displaced by an electric current using the STT effect [7]. Magnetic bits can thus be moved along a wire using current pulses. This allows one reading and one

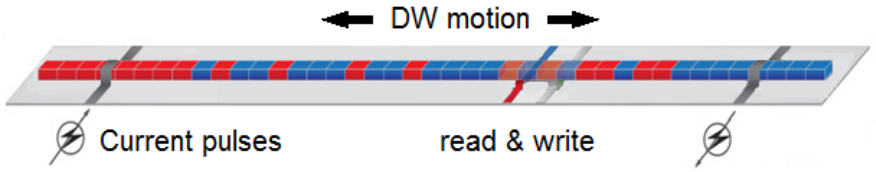

Figure 1.2: *Artist impression of magnetic racetrack memory. The blue and red sections of the wire represent domains of opposite magnetisation, which are used to store binary information. Domains can be moved along the wire towards the reading and writing elements by applying current pulses.*

writing element to address many bits, sacrificing some speed for increased data density. The MRM concept and other devices such as magnetic logic [8] have triggered considerable research effort aiming to realise reproducible and efficient domain wall motion.

Two methods are generally employed to change the magnetisation in spintronics devices: magnetic fields and electric currents. These methods are sketched in the first two panels of Fig. 1.3, acting on a magnetic domain wall in a wire. An applied magnetic field can obviously be used to change the magnetisation direction, but this method is power-consuming and cannot be scaled down to small dimensions. In multi-domain applications such as MRM, magnetic fields are unsuitable as they grow and shrink domains rather than moving them. Alternatively, spin-polarised currents can be used to displace domain walls or to switch magnetic bits through STT, as mentioned before.

A novel third method of magnetisation manipulation is the subject of this thesis. Experiments have shown that *electric fields* can affect magnetic properties in thin film systems [9], providing an interesting addition to the spintronics toolbox. Technologically, the use of electric fields rather than currents could lead to ultra-low power magnetic devices. Magnetic switching using voltage pulses has been envisioned [9] and realised [10] within a few years time. This work aims to reproduce such electric field effects, and to provide a contribution to the field by linking such effects to magnetic domain wall motion as illustrated in the third panel of Fig. 1.3.

In this introductory chapter, a phenomenon unique to thin films called perpendicular magnetic anisotropy is first introduced. The concept of magnetic anisotropy is crucial in understanding electric field effects in magnetic thin films, as explained

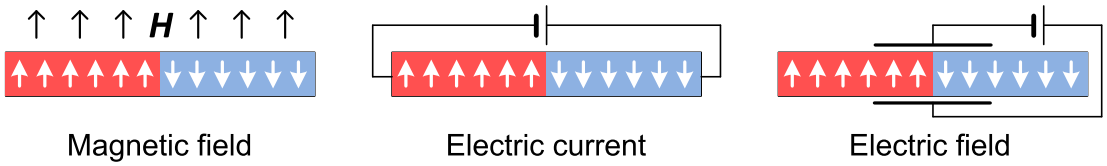

Figure 1.3: *Sketch of three different mechanisms to control magnetism. From left to right, these mechanisms include an applied magnetic field, an electric current, and an electric field. The magnetisation is depicted by arrows in sample; a domain wall is present in the middle of the wire.*

in section 1.3. An overview of recent research is included, describing both material research and first moves towards applications. Following this discussion of electric field effects, more background on domain wall motion is given in section 1.4. Finally, an overview of this thesis is presented in section 1.5.

1.2 Perpendicular magnetic anisotropy

In traditional magnetic storage devices, including early MRAM designs, layers were magnetised along their surface as sketched in Fig. 1.1b. This so-called *in-plane* magnetisation comes natural to conventional magnetic systems; the well-known bar magnet for example is always magnetised along its long axis. The existence of such a preferential direction for the magnetisation is referred to as *magnetic anisotropy*.

In the past two decades, advances in material growth techniques have allowed scientists to fabricate ultrathin magnetic films (only a few atomic layers thick) which display unique properties. The magnetisation in very thin films can point *out-of-plane*, as depicted in for example Fig. 1.3. This *perpendicular magnetic anisotropy* (PMA) is caused by electronic interactions at the interfaces between the magnetic material and the surrounding layers, as will be explained in detail in this report. The interfacial origin of the effect explains why it is mostly observed in extremely thin films.

The use of PMA materials has important technological advantages. The magnetisation in perpendicular magnetic multilayers is more stable than in in-plane configurations, allowing devices to be scaled down to the 10 nm regime while maintaining room-temperature stability [11]. This implies a significant increase in data density compared to in-plane materials. Furthermore, perpendicularly

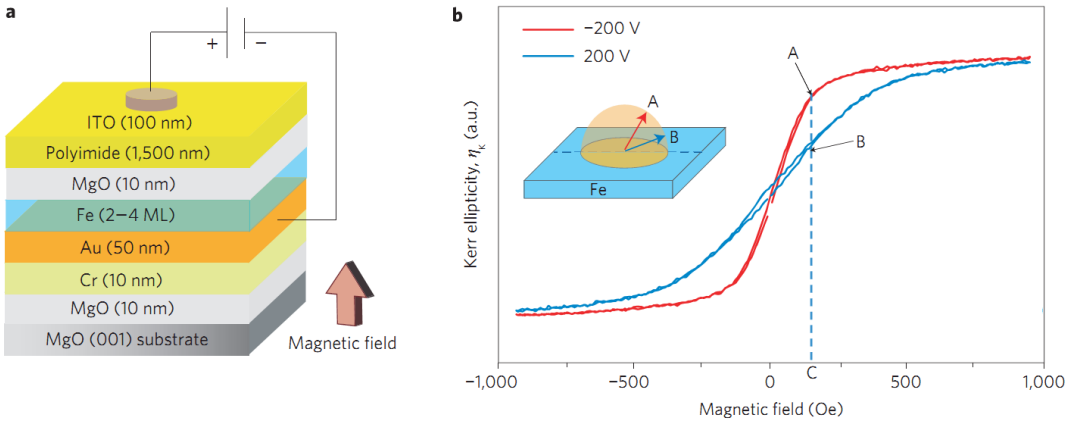

Figure 1.4: *Demonstration of electric field effects in a solid-state device at room temperature by Maruyama et al. a) Sketch of the used sample composition. The crucial part of this stack is the Au/Fe(2-4 ML)/MgO sandwich; the magnetisation points in-plane. b) Perpendicular magnetisation component as a function of magnetic field, for two different applied voltages. A negative voltage is seen to tilt the magnetisation out-of-plane. Figure taken from [9].*

magnetised layers are expected to be readily switched using STT [12], leading to worldwide efforts to realise perpendicularly magnetised MRAM [11]. Domain wall motion devices may also benefit from perpendicularly magnetised materials, as explained in section 1.4.

1.3 Changing magnetic properties using an electric field

Magnetic properties, including the anisotropy, are in principle determined during fabrication: the material composition and deposition parameters can be varied to create desirable properties. During the operation of a device, these properties could traditionally only be modified through heating. Raising the temperature of a magnetic material reduces its magnetic anisotropy, which is for example used in thermally assisted MRAM [13]. An alternative approach to real-time control of magnetic properties was first discovered in 2000 by Ohno *et al.* [14], who demonstrated electric-field control of ferromagnetism in semiconductors at cryogenic temperatures. The first observation of such an effect at room temperature in a solid-state device was reported by Maruyama *et al.* in 2009 [9], who managed to change the magnetic anisotropy in an Fe/MgO junction by as much as 40% by

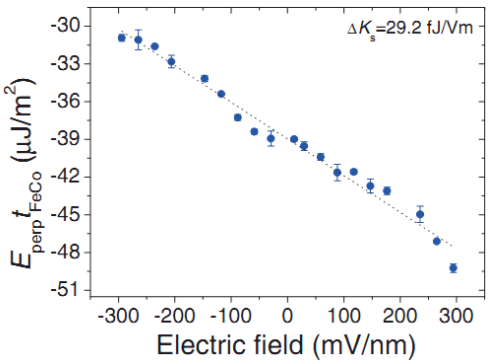

Figure 1.5: *Surface anisotropy as a function of applied electric field in an Au/FeCo(0.68 nm)/MgO junction. The electric field effect is found to be linear. Note that the anisotropy energy density E_{perp} is multiplied by the magnetic film thickness t_{FeCo} to obtain a surface anisotropy defined per square metre. Figure taken from [15].*

applying an electric field of 100 mV/nm. Their measurement, shown in Fig. 1.4, is discussed here as an introduction to the electric field effect in magnetic films.

In the experiment by Maruyama *et al.*, a thin Fe layer is sandwiched between Au and MgO layers, as depicted in Fig. 1.4a. The magnetisation of this Fe layer points in-plane. The MgO layer features a high electrical resistance, so that electrons injected from the bottom contact stop at the Fe/MgO interface. Electronic interactions at this interface can cause PMA, as mentioned in the previous section. The main outcome of the experiment is shown in Fig. 1.4b: the application of a voltage affects the magnetisation angle in an applied magnetic field. This indicates that the magnetic anisotropy of the Fe layer is affected by the presence of charges at the Fe/MgO interface, a spectacular result. The same research group later quantified the anisotropy modification as a function of applied electric field, as depicted in Fig. 1.5, and found it to be linear.

In the remainder of this section, other relevant experimental results on electric-field control of magnetism are discussed.

1.3.1 Materials

Since its first discovery, different groups have studied voltage control of ferromagnetism in many different materials. This section provides an overview of their results.

The first demonstration of direct electric field control of ferromagnetism was given by Ohno *et al.* in 2000 [14]. Experiments were carried out on (In,Mn)As, a III-IV semiconductor which exhibits hole-induced ferromagnetism below $T_C \approx 30\,K$. The mechanism is quite different from the one discussed in this report, and the required cryogenic temperatures limit the applicability of the effect. Voltage control in transition metals, at room temperature, was first demonstrated by Weisheit *et al.* in 2007 [16]. They demonstrated reversible modification of the coercivity in an applied electric field in FePt and FePd compounds immersed in an electrolyte. The use of an electrolyte, however, makes this particular application impractical for integration into existing technology.

The first observation of voltage control over magnetism in an all solid-state device at room temperature was reported by Maruyama *et al.* in 2009 [9]. A relatively small electric field (less than 100 mV/nm) was seen to cause a large change (40%) in the magnetic anisotropy of a Fe(001)/MgO(001) junction. Notably, this publication included a simple simulation showing the switching of magnetic bits using a voltage pulse, further stimulating research efforts. Shortly after, the same group realised [17] switching of the magnetic easy axis between the in-plane and out-of-plane directions using $Fe_{80}Co_{20}$(001)/MgO(001) junctions. Voltage-induced magnetization switching under the assistance of magnetic fields was demonstrated, but switching by a voltage pulse alone remained a challenge. This was finally achieved in 2012 [10]; see section 1.3.2.

Further efforts showed voltage control of magnetic anisotropy in many different systems. So far, FeCo [9, 17, 18, 15], CoFeB [19, 20], FePd [21], CoPd [22], and CoCrPt–TiO_2 [23] have been studied. For an overview of all this experimental data, the reader is referred to the compilation by Fowley *et al.* [20]. It should be noted that FeCo and CoFeB are of primary interest for magnetic tunnel junctions, because they provide a large tunnel magnetoresistance when coupled to MgO(001) [24, 25]. On the other hand, Pd- and Pt-based alloys are choice materials for recording media because of their large PMA [21].

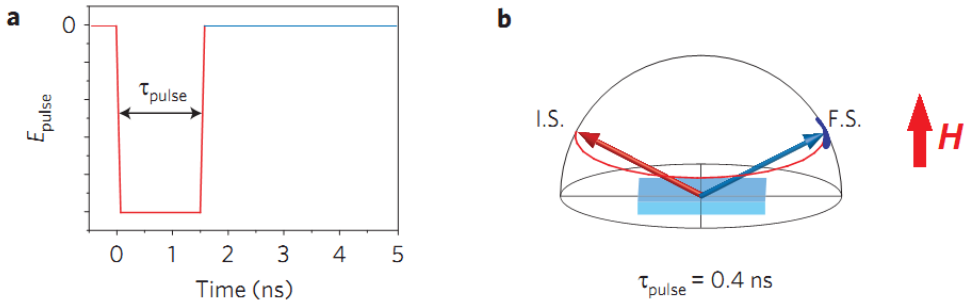

Figure 1.6: *Simulation of precessional switching using an applied voltage pulse. a) Shape of the applied pulse. b) Precessional switching process in a constant applied magnetic field H, from initial state I.S. to final state F.S. Figure taken from [10].*

1.3.2 Applications

One can safely state that electric field effects in magnetic thin films have attracted significant scientific interest in a short amount of time. The reason for this is probably the technological applicability; the demonstrated effects promise new possibilities while being fully compatible with current-day solid state technology.

Very soon after the first demonstration of the electric field effect in thin films by Maruyama *et al.* in 2009 [9], the effect was demonstrated in a present-day hard disk recording medium (CoCrPt–TiO_2) by Zhou *et al.* [23]. Through application of 3 V across the head-media gap, a 13% reduction of the writing current was achieved as well as a 3 dB improvement in read back signal-to-noise ratio. Similar to heat-assisted recording, such improvements are highly interesting to the billion dollar hard disk industry.

Another possible application of the effect lies in magnetic tunnel junctions (MTJs). These devices have been a main research area in spintronics since the field first emerged, mainly because of their application in hard-disk drive read heads. A promising new application of MTJs lies in non-volatile magnetic random access memory (MRAM). Electric field modification of the anisotropy in such MTJs was first demonstrated in 2010 by Nozaki *et al.* [18]. In 2012, Wang *et al.* reported [26] electric-field-assisted reversible switching in CoFeB/MgO/CoFeB MTJs with interfacial perpendicular magnetic anisotropy. Their results include an average switching current density of $2.4 \times 10^4 \mathrm{A/cm^2}$; much lower than the $10^6 - 10^8 \mathrm{A/cm^2}$ required in conventional current-induced MTJ switching.

Even more promising than electric-field-assisted writing is the prospect of switching through anisotropy modification alone. This could be realised by precessional switching using nanosecond voltage pulses (see Fig. 1.6), as envisioned by Maruyama *et al.* in their first publication on the electric field effect [9]. Shiota *et al.* [10] first managed to achieve this in 2012: they demonstrated coherent precessional magnetization switching using electric field pulses in nanoscale magnetic cells. Crucially, bistable toggle switching was achieved in a constant magnetic bias field, so that no power was required to generate varying magnetic fields. The estimated power consumption for single switching in the ideal equivalent switching circuit was estimated to be of the order of $10^4\, k_{\mathrm{B}}T$; 500 times smaller than required in the spin-current-injection switching process. This achievement alone justifies extensive further research into the electric-field control of thin film magnetism.

1.4 Domain wall motion

As mentioned before, magnetic racetrack memory and other device concepts have triggered considerable research effort into magnetic domain wall motion. Domain walls have successfully been moved using electric currents [6], but many practical issues remain to be solved. Remaining challenges include improving the reproducibility of the induced motion and reducing the required current densities. A common strategy to increase DW motion reproducibility is to create *pinning sites* [6]; preferred positions for DWs such as geometrical constrictions. A drawback of this strategy is that strong pinning further increases the current density required to induce DW motion.

Perpendicularly magnetised materials offer several advantages in DW motion applications. A large PMA reduces the DW width, increasing data density potential. Narrow DWs are also more strongly affected by spin-polarised currents, which scales with the local magnetisation gradient. In general, however, current-induced DW motion is difficult in PMA materials due to strong pinning effects [27]. High DW velocities were recently reported in a specific material, Pt/Co/AlOx [28], apparently induced by an effect other than STT [29]. This perpendicularly magnetised material is highly interesting for DW motion research, and will also be used in this research project.

Electric field control of PMA could prove to be a useful tool in DW motion applications. As an example, local variations in the magnetic anisotropy could

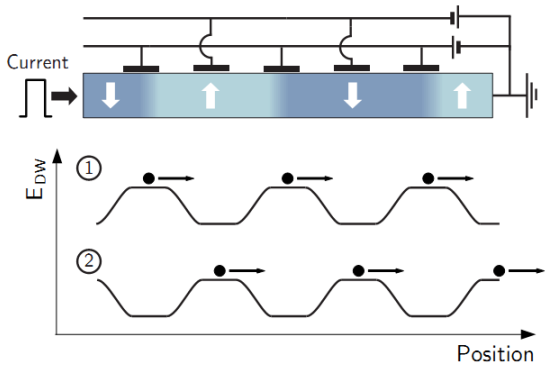

Figure 1.7: *Device concept using electric fields to reversibly create local domain wall pinning sites. Domain walls are moved using current pulses. During each current pulse, the anisotropy is locally varied using electric fields, generating the DW energy landscapes sketched in the bottom panel. The polarity of the applied voltage is alternated between subsequent current pulses (indicated as '1' and '2'), so that domain walls always move towards a lower-energy position.*

be used to stabilise domain wall motion without increasing the required current density, as illustrated in Fig. 1.7. Many more applications are possible; electric field induced modification of magnetic anisotropy is a unique tool, providing new ways of designing spintronics devices.

1.5 This thesis

In this thesis, the topics of electric field-induced magnetic anisotropy modification and magnetic domain wall motion are combined, resulting in experimental observations previously unreported in the literature.

A theoretical description of perpendicular magnetic anisotropy is first presented in Chapter 2, leading to an intuitive picture of electric field effects in thin magnetic films. The described concepts are used to develop a model of electric-field induced anisotropy modification, yielding an estimate of the expected order of magnitude of such effects. Domain wall propagation is also described in Chapter 2, deriving a relation between the domain wall velocity and the applied voltage that can be used to understand experimental results.

Chapter 3 gives a short description of the experimental techniques that were used in this research project. The sample fabrication procedure is described, as

well as the equipment that was used to probe the magnetisation.

The obtained experimental results are presented in Chapter 4. This includes a description of the performed material research, followed by the first observation of a voltage-induced effect in the form of a coercivity modification. A study of the magnetic switching using Kerr microscopy subsequently reveals that domain wall motion is key in the magnetisation reversal process. Measurement of the domain wall velocity under application of a voltage subsequently yields an unprecedented view of the electric field effect: clear and quantitative evidence of voltage-controlled domain wall motion is presented. This observation, previously unreported in the literature, promises exciting new capabilities for domain wall motion devices.

Finally, conclusions based on the theoretical and experimental work are presented in Chapter 5, followed by a research outlook in Chapter 6.

Chapter 2

Theory

This chapter aims to explain the origin of magnetic anisotropy, and to demonstrate theoretically how an electric field can alter its magnitude. A model developed to predict the order of magnitude of this effect is also discussed, along with more advanced first-principles calculations described in the literature. Finally, the magnetisation reversal process in thin films is discussed, with emphasis on domain wall motion, as an understanding of this process is crucial to the analysis of performed experiments.

2.1 Magnetic anisotropy

To understand the electric-field-induced modification of magnetic anisotropy, a basic understanding of the origin of this anisotropy is required. The current section introduces relevant concepts and terminology to the general reader, and elaborates to form an intuitive picture of magnetic anisotropy.

The transition metals Fe, Co, and Ni display a spontaneous magnetisation $\mathbf{M}$ below their Curie temperature T_C; a phenomenon known as *ferromagnetism*. Heisenberg first recognised the mechanism behind this spontaneous ordering as the Pauli principle, which prevents two electrons from occupying the same state. Two electrons of parallel spin cannot occupy the same orbital, decreasing the effective Coulomb repulsion between the two. This mechanism, known as the *exchange interaction*, makes the parallel spin state energetically favourable. The energy associated with the exchange interaction is of the order of $k_B T_C$/atom $\approx$ 0.1 eV/atom [30].

The magnetisation in ferromagnets generally points in some preferred direction with respect to the crystalline axes and/or the shape of the magnetic body. The lowest energy orientation is referred to as the *easy axis*, whereas the high energy orientation is referred to as the *hard axis*. The *magnetic anisotropy* (symbol K, dimensions [energy/volume], units $\mathrm{J\,m^{-3}}$) is defined as the energy that it takes

to rotate the magnetisation from the easy into the hard direction [31]. For an arbitrary angle θ between the magnetisation direction and the easy axis, the *magnetic anisotropy energy* (MAE) density is in first order given by

$$E_{ani} = K \sin^2 \theta. \tag{2.1}$$

Conventionally, in thin films, a positive value of K denotes an out-of-plane easy axis, whereas a negative K denotes an in-plane easy axis. The MAE is small compared to the total magnetic energy associated with the exchange interaction; typically 10^{-6} to 10^{-3} eV/atom [30]. Expressed in units of magnetic field, the MAE is of the order of 10 mT - 10 T; magnetic field strengths typically accessible in experimental situations and technological applications. Magnetic anisotropy therefore plays a crucial role in for example magnetic information storage.

A clear distinction can be made between two types of magnetic anisotropy. Suppose we take a magnetic material with cubic crystalline structure and cut two samples out of it; a perfect sphere and a thin slab in the xy-plane. The sphere will exhibit three easy axes of magnetisation; the three cubic crystal axes. Since the sample is perfectly spherical and thus isotropic, this anisotropy must arise from the crystal itself. This intrinsic anisotropy is referred to as *magneto-crystalline anisotropy*. For the slab, on the other hand, the z-axis is reported to become a hard axis. Since the three cubic axes are crystallographically equivalent, this anisotropy must arise from the shape of the sample, hence the name *shape anisotropy*. For an arbitrary sample, the easy axis is determined by a competition between the magneto-crystalline anisotropy and the shape anisotropy. Both types of anisotropy are discussed in more detail in following sections.

In thin films, it is useful to separate *volume* and *surface* contributions to the total anisotropy. The total anisotropy in a slab can be written as

$$K = K_V + 2K_S/t, \tag{2.2}$$

where K_V and K_S denote the volume and surface anisotropies, respectively, and t is the slab thickness. The factor 2 in the surfaces term results from the top and bottom contributions. The volume anisotropy includes the shape anisotropy (scaling with $|\mathbf{M}|$) and a weak magneto-crystalline anisotropy. The surface term is due to magneto-crystalline anisotropy, which is significantly enhanced at surfaces due to interfacial bonding effects, as explained in section 2.1.2.

From Eq. 2.2, it is evident that the balance between volume and surface contributions to the total anisotropy depends on the film thickness. For relatively

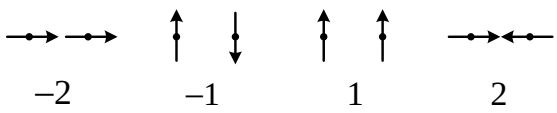

Figure 2.1: *Dipole-dipole interaction energies for four different relative alignments. The numbers below the drawings denote the energy in multiples of* $\frac{\mu_0 m^2}{4\pi r^3}$.

thick films, the volume contribution is dominant. This volume anisotropy mainly consists of shape anisotropy, pulling the magnetisation in-plane, so that thick films exhibit an in-plane easy axis. In very thin films, on the other hand, the surface term dominates over the volume term. This surface anisotropy arises from enhanced magneto-crystalline anisotropy at interfaces, which can favour an out-of-plane magnetisation. The easy axis in very thin films can thus point out-of-plane despite the shape anisotropy; a phenomenon referred to as *perpendicular magnetic anisotropy* (PMA). More insight into PMA is essential to an understanding of electric-field effects in thin films. To this end, the origins of shape anisotropy and magneto-crystalline anisotropy are discussed in more detail in the following sections.

2.1.1 Shape anisotropy

As mentioned before, neighbouring electrons in overlapping orbitals assume parallel spin states due to the exchange interaction. Although this mechanism establishes a preferred *relative* spin orientation, the magnetisation direction remains intrinsically isotropic. Dipolar coupling between the magnetic moments associated with the spins, however, introduces magnetic anisotropy. The potential energy associated with the dipole-dipole interaction for two spins is given by:

$$E_{\mathrm{dip-dip}} = -\frac{\mu_0}{4\pi r^3}\left[\mathbf{m_1}\cdot\mathbf{m_2} - 3\left(\mathbf{m_1}\cdot\hat{\mathbf{r}}\right)\left(\mathbf{m_2}\cdot\hat{\mathbf{r}}\right)\right], \tag{2.3}$$

where $\mathbf{m_i}$ denotes a magnetic moment, r is the distance between the moments, and $\hat{\mathbf{r}}$ is the unit vector connecting the two moments. The anisotropic effect of this interaction is demonstrated in Fig. 2.1 using four different relative alignments. Clearly, the dipole-dipole interaction energy is smallest when both spins align parallel to the internuclear axis. Macroscopically, this implies that a magnetic body is preferably magnetised along its longest axis. This macroscopic effect of the dipole-dipole interaction is commonly described using an effective magnetic

field inside the material called the *demagnetising field* $\mathbf{H_d}$. In general, this demagnetising field $\mathbf{H_d}$ is written as

$$\mathbf{H_d} = -N\mathbf{M}, \tag{2.4}$$

where N is a *demagnetisation factor*, which depends on the geometry of the sample. For thin films, the demagnetisation factor can be easily derived in the limiting cases of in-plane and out-of-plane magnetisation. Applying Ampere's law to an in-plane magnetised thin film yields $\mathbf{H_d} = 0$, so that $N = 0$ in this case. For an out-of-plane magnetised sample, a Gaussian box can be used to show that the perpendicular component of $\mathbf{B} = \mu_0 (\mathbf{H} + \mathbf{M})$ must be continuous across the interface. This implies that $\mathbf{H_d} = -\mathbf{M}$ so that $N = 1$ for an out-of-plane magnetised thin film. For thin films, we thus find a clear anisotropy in the demagnetisation field: it tends to pull the magnetisation in-plane. This *shape anisotropy* is actually a macroscopic manifestation of the microscopic dipole-dipole interaction favouring spin alignment along internuclear axes.

The dipolar interaction, which is essential to the existence of shape anisotropy, also contributes to crystalline anisotropy. This can be intuitively understood from Fig. 2.1: the dipole-dipole interaction energy is smallest when both spins align parallel to the internuclear axis. For bulk hcp cobalt, the dipolar crystalline anisotropy has been determined to be $K^V_{\text{dip}} \approx 4 \cdot 10^{-7}$ eV/atom [32]. This contribution is small compared to experimentally observed anisotropy energies (see Table 2.1). A different mechanism must be responsible for this large crystalline anisotropy, as discussed in the next section.

2.1.2 Magneto-crystalline anisotropy

Crystalline ferromagnetic materials have been shown to posses large bulk anisotropies; preferred magnetisation directions with respect to the crystalline axes. Some reported values are given in Table 2.1. As mentioned in the previous section, dipole-dipole interactions are too weak to explain these large experimentally observed anisotropies. It was first proposed by Van Vleck [33] in 1937 that this magneto-crystalline anisotropy (MCA) arises from the spin-orbit interaction, coupling the isotropic spin magnetic moment to the anisotropic lattice. He noted that, because of spin-orbit coupling, the spins feel slightly the anisotropy in orbital angular momenta caused by bonding orbitals. The detectable effect of this is

Table 2.1: *Bulk anisotropy energies for the transition metals at 4.2 K. Listed are the crystal structure, shape anisotropy constant $K_s = -\frac{1}{2}\mu_0 M^2$, magneto-crystalline anisotropy constant K_u, and the easy axis. Adapted from [31], p. 509.*

metal	structure	K_s [eV/atom]	K_u [eV/atom]	easy axis
Fe	bcc	-1.4×10^{-4}	4.0×10^{-6}	[100]
Co	hcp	-9.3×10^{-5}	5.3×10^{-5}	c-axis
Ni	fcc	-1.2×10^{-5}	8.6×10^{-6}	[111]

Figure 2.2: *Semiclassical explanation of spin-orbit coupling. Traditionally, an atom is represented as a stationary nucleus with orbiting electrons, as shown on the left-hand side. In an electron's rest frame, as shown on the right-hand side, the nucleus is in motion and generates an orbital magnetic moment, depicted here as an effective magnetic field* **B**.

an apparent dipole-dipole coupling between spins on different atoms which is about fifty times larger than results from the pure magnetic forces discussed in the previous section.

The current section aims to explain in more detail the origin of orbital angular momentum anisotropy in crystals, and the role of spin-orbit coupling. A short discussion of spin-orbit coupling and bonding in crystals leads to the introduction of a ligand field model, which provides an intuitive explanation of this anisotropy. This ligand field model has been extended to estimate the magnitude of the electric-field-induced anisotropy modification, as discussed in section 2.2.1.

2.1.2.1 Spin-orbit interaction

The existence of a coupling between the electron spin and its orbital motion can be intuitively understood using semiclassical concepts, as illustrated in Fig. 2.2. In the rest frame of the nucleus, an orbiting electron does not experience any magnetic field. In the rest frame of the electron, however, the positively charged nucleus executes an orbital motion which creates a magnetic field. The electron

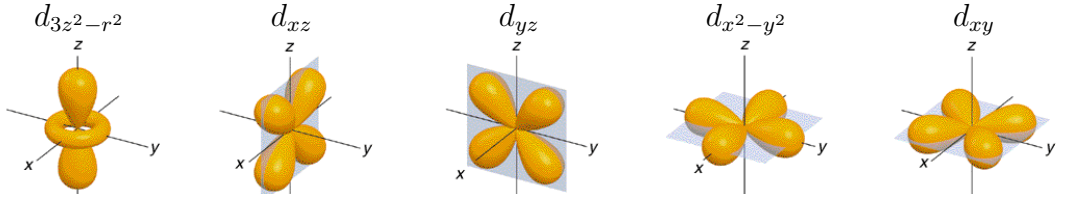

Figure 2.3: *The 3d orbitals, described as linear combinations of L_z eigenfunctions denoted by their eigenvalue $|m_l\rangle$.*

also carries an intrinsic magnetic moment, associated with its spin, which couples to this magnetic field. The spin-orbit interaction therefore modifies the electron energy according to the general Hamiltonian

$$\mathbf{H}_{\mathrm{SO}} = \xi\,(\mathbf{L}\cdot\mathbf{S})\,, \tag{2.5}$$

where ξ is the material-dependent *spin-orbit constant* (order 0.05 eV), $\mathbf{L}$ the electron orbital moment, and $\mathbf{S}$ the electron spin in units of $\hbar$. Note that $\mathbf{L}$ points in the opposite direction from the orbital magnetic moment, so that E_{SO} is minimal if $\mathbf{S}$ and $\mathbf{L}$ are anti-parallel.

With this coupling established, explaining magneto-crystalline anisotropy becomes a task of finding preferential directions for $\mathbf{L}$ caused by the crystal lattice.

2.1.2.2 Atomic 3*d* orbitals

The common magnetic elements cobalt, nickel, and iron all feature a partially filled $3d$ shell. Ferromagnetism in these materials is caused by spatial overlap between these $3d$ electrons; the exchange interaction favours parallel spin alignment if electron wavefunctions overlap. Inspection of wavefunctions in crystals provides an intuitive understanding of crystalline anisotropy.

Electron wavefunctions are solutions to the Schrödinger equation, usually described as a set of quantum numbers $|n, l, m_l, m_s\rangle$. For the $3d$ shell $n = 3$, $l = 2$, $m_l = \{-2, -1, 0, 1, 2\}$, and $m_s = \{-1/2, +1/2\}$, forming a complete set of ten solutions or states. This particular set, ignoring the spin degree of freedom, consists of five eigenfunctions of the L_z operator, so that each solution has a well-defined and constant value of m_l. These solutions cannot be drawn on paper: they are not eigenfunctions of the x, y, and z position operators, which means their

spatial layouts must change in time. In fact, a well-defined non-zero magnetic moment *dictates* that the spatial part of a wavefunction must be rotating in time, as magnetic fields are created by moving charge.

The mentioned solutions are degenerate in absence of an external magnetic field or other perturbations. Linear combinations of the L_z eigenfunctions are therefore equally valid solutions. Making such linear combinations, it is possible to construct a complete set of five orthogonal solutions with $m_l = 0$, carrying no orbital magnetic moment. These *stationary* solutions are commonly referred to as the *3d orbitals*, and are presented in Fig. 2.3 as linear combinations of L_z eigenfunctions. Note that each combination is such that $L_z = 0$. The importance of this particular set of solutions will become clear in the next section.

2.1.2.3 Ligand field model

The set of stationary solutions presented in the previous section becomes all the more relevant if we introduce neighbouring atoms. In the so-called *ligand field model*, these neighbouring atoms (referred to as *ligands*) are introduced as point charges which act on the central atom only through Coulombic repulsion. Electrons experience an additional potential caused by neighbouring electron clouds; the *crystal field*. The Coulombic energy related to this potential is of the order of 1 eV; small compared to the tens of eVs related to the nuclear potential. The crystal field can thus be treated as a perturbation; the previously found wavefunctions are still valid but their energies are shifted.

The energy shift of each wavefunction depends on its proximity to neighbouring atoms, and thus on its spatial layout. This spatial layout is constant in time only for the set of stationary orbitals (see Fig. 2.3), indicating that these orbitals are eigenfunctions of the Hamiltonian in the presence a crystal field. Using these orbitals, the energy shift induced by the crystal field is easily demonstrated in a free-standing monolayer, as depicted in Fig. 2.4. The z-axis is chosen out-of-plane. The two in-plane d orbitals, d_{xy} and $d_{x^2-y^2}$, display a profoundly different overlap with ligand charges. In this classical picture, a Coulombic energy difference thus arises between orbitals, which is referred to as *crystal field splitting*. In a free-standing monolayer the crystal field splitting is smaller for the out-of-plane orbitals, since they do not significantly overlap with ligand charges. This observation is crucial to the understanding of interfacial anisotropy.

A second perturbation that needs to be taken into account is the spin-orbit

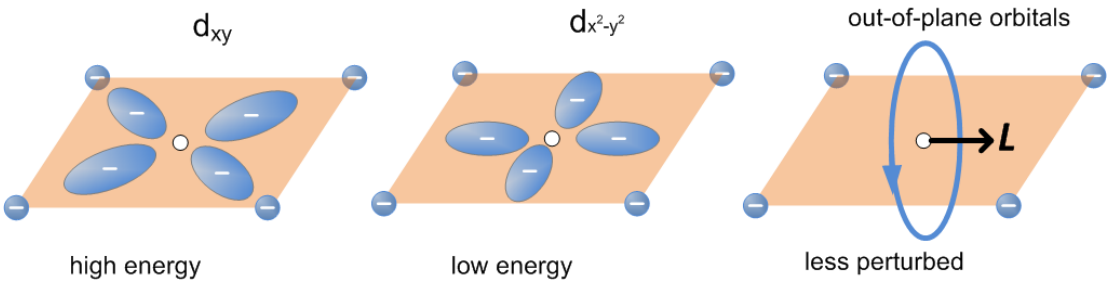

Figure 2.4: *Directional quenching of the orbital momentum by ligand field effects in a free-standing monolayer. The d_{xy} orbital strongly overlaps ligand charge clouds, raising it in energy compared to the $d_{x^2-y^2}$ orbital. This prevents mixing between the orbitals, quenching the out-of-plane orbital momentum. The three out-of-plane orbitals, on the other hand, are less perturbed by the ligand charges, and can still mix to create an in-plane orbital momentum.*

interaction, described in section 2.1.2.1. Due to this interaction, the energy of a wavefunction is reduced if the spin **S** aligns to the orbital momentum **L**. This energy reduction is of the order of 0.1 eV; significantly smaller than the crystal field splitting. In a crystal, spin-orbit coupling can thus be treated as a perturbation of the crystal field Hamiltonian eigenfunctions.

The existence of orbital momentum anisotropy can now be understood by taking into account both crystal field splitting and spin-orbit coupling. The eigenfunctions of the crystal field Hamiltonian are stationary orbitals, with $\mathbf{L} = 0$. The spin-orbit perturbation, however, can reduce the energy for states with finite **L**. This perturbation leads to *mixing*: the lowest energy solutions are linear combinations of stationary orbitals with some orbital momentum coupled to the spin. The relative size of the crystal field splitting and the spin-orbit coupling energy determines the amount of mixing: a large splitting prevents mixing and reduces the orbital momentum. If the crystal field splitting is anisotropic, as in the free-standing monolayer, the total orbital momentum is thus also anisotropic. This holds for any interface where the crystal environment is anisotropic.

Concluding, this simple ligand field model intuitively relates the anisotropy of the orbital momentum to the anisotropy of the crystal environment.

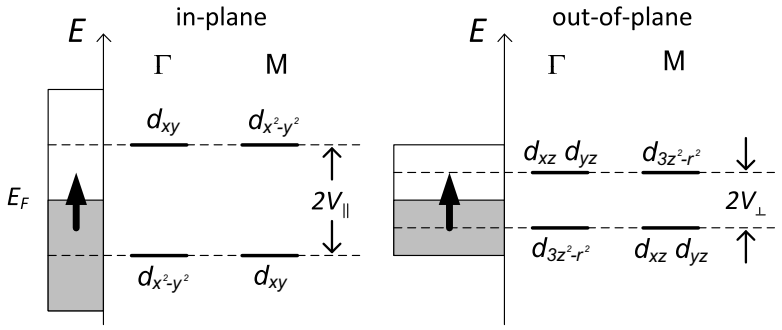

Figure 2.5: *Simplified density of minority spin states for a free-standing Co [100] monolayer. The band picture may be represented by a ligand field model where the average separation between filled and empty states is defined as $2V_{\|}$ and $2V_{\perp}$ for in-plane and out-of-plane orbitals, respectively. An average is performed over two points in the Brillouin zone (Γ and M) where the filled and empty d orbitals are exchanged. Adapted from [34].*

2.1.2.4 Band structure approximation

A complication to the simple model described in the previous section needs to be taken into account: in a metallic system, valence electrons are not isolated on a single atom but form wavefunctions that are superpositions of atomic orbitals. The energy of such a wavefunction depends on the phase difference between adjacent orbitals, expressed in the wave vector **k**, giving rise to *band structure*. The reader is referred to Appendix A for more information on band structure in the atomic orbital approach.

Following the approach of Stöhr [34], we approximate the band structure of a cobalt monolayer using the simplified density of states (DOS) depicted in Fig. 2.5. The majority band is assumed to be completely full, whereas the minority band is assumed to be half-filled, in agreement with band structure calculations for bulk and monolayer Co [35, 36]. The in-plane orbitals $d_{x^2-y^2}$ and d_{xy} are assumed to have the same DOS, with an average separation between filled and empty states of $2V_{\|}$. Similarly, the out-of-plane orbitals $d_{3z^2-r^2}$, d_{xz}, and d_{yz}, are assumed to have the same DOS, with an average separation between filled and empty states of $2V_{\perp}$. These assumptions are reasonable, based on the actual DOS depicted in Fig. A.2a. Averaging over the Brillouin zone is approximated by averaging over two points, labelled $\mathbf{k}_1$ and $\mathbf{k}_2$, where the density of states is highest. Based on

calculations by Wang *et al.* [36] these are chosen as the Γ and M points. It turns out that for a Co [100] monolayer, the order of the band states is inverted in those points, simplifying further calculations.

The key parameter in the model is the ratio $V_\perp/V_\parallel$, which describes the relative size of the out-of-plane and in-plane bonding strength. At interfaces, where the Co layer is in contact with other materials, the bonding of the out-of-plane Co d orbitals with the other material changes this ratio. For example, if the in-plane Co-Co bonding strength is normalized to 1, then the Co-X bonding strength is 1.53, 1.60, 1.38, 0.83 for X = Au, Pt, Pd, and Cu, respectively [36]. If $V_\perp > V_\parallel$ (for a Pt/Co/Pt sandwich, for example) one expects more quenching of the out-of-plane orbitals, which means that (remembering that mixing of in-plane orbitals causes out-of-plane angular momentum) such a film is expected to display perpendicular magneto-crystalline anisotropy.

2.1.2.5 Anisotropy calculation in the ligand field model

We now aim to calculate the magneto-crystalline anisotropy energy using the ligand field model and the simplified density of states presented in the previous section. Bruno has shown [30] theoretically that, under certain assumptions[1], the anisotropy of the spin-orbit energy is related to the anisotropy of the orbital moment as

$$\Delta E_{\mathrm{SO}} = \xi \left(\langle \mathbf{L} \cdot \mathbf{S} \rangle_{\mathrm{hard}} - \langle \mathbf{L} \cdot \mathbf{S} \rangle_{\mathrm{easy}} \right) = \frac{\xi}{4\mu_{\mathrm{B}}} \left(m_o^{\parallel} - m_o^{\perp} \right) \tag{2.6}$$

where ξ is the spin-orbit constant (see section 2.1.2.1) and m_o^α is the orbital magnetic moment in direction α. Using the elementary relation $m_o = -\frac{\mu_{\mathrm{B}}}{\hbar} \langle L \rangle$ this can be written as

$$\Delta E_{\mathrm{SO}} = \frac{\xi}{4\hbar} \left(\langle L^z \rangle - \langle L^x \rangle \right). \tag{2.7}$$

Computing the anisotropy energy thus becomes a task of computing expectation values for the orbital momentum along two axes. The crystal field splitting is assumed to be large compared to the spin-orbit coupling energy, so that the latter

[1] Notably, it is assumed in this simple picture that the exchange splitting is large compared to the crystal field splitting, so that there is no mixing between spin-up and spin-down states. In this case the effect of this spin-orbit coupling is that of an effective magnetic field acting only on the orbital magnetic moment.

may be computed using perturbation theory. The orbital momentum supplied by this spin-orbit perturbation is computed using the second order perturbation expression [37]:

$$\langle L^\alpha \rangle = \frac{2\xi}{\hbar^2} \sum_{n,m,j,\mathbf{k}} \frac{\langle \phi_n^j(\mathbf{k}) \left| L^\alpha \right| \phi_m^j(\mathbf{k}) \rangle}{\Delta_{nm}(\mathbf{k})} \left\langle \chi^j \left| S_z \right| \chi^j \right\rangle , \tag{2.8}$$

where the sum extends over filled states n, empty states m, spin directions j, and wave number $\mathbf{k}$. Note that the spin function χ is an eigenfunction of S_z, such that $\langle \chi^\pm \left| S_z \right| \chi^\pm \rangle = \pm\frac{1}{2}\hbar$. The appropriate basis states for Eq. 2.8 are the stationary $3d$ orbitals, so that the energy difference $\Delta_{nm}(\mathbf{k})$ between states $\phi_n^j(\mathbf{k})$ and $\phi_m^j(\mathbf{k})$ is determined by the crystal field splitting: $\Delta_{(xy)(x^2-y^2)} \equiv 2V_\parallel$ and $\Delta_{(yz)(3z^2-r^2)} \equiv 2V_\perp$. In the transition metals, the majority band is completely filled and therefore does not contribute to the angular momentum. Also, to first order, mixing between spin-up and spin-down states does not contribute to the orbital momentum [34]. The spin-down states can thus be left out of the summation in Eq. 2.8.

In a Co monolayer, Eq. 2.8 can be further simplified using some features of the simplified DOS depicted in Fig. 2.5. Brillouin zone averaging is performed over just two $\mathbf{k}$-points in the [100] fcc plane, Γ and M, in which the crystal field split levels are simply inverted (see section 2.1.2.4). The minority (spin-up) band is assumed half-filled, containing 2.5 electrons. The filled states are $d_{x^2-y^2}$ and $d_{3z^2-r^2}$ in the Γ-point and d_{xy}, d_{xz}, and d_{yz} in the M-point, as should be clear by inspection of Fig. 2.5. Evaluating Eq. 2.8 with these assumptions [2] yields the following expression for the MCA energy:

$$\Delta E_{\mathrm{SO}} = \frac{\xi^2}{8V_\parallel} \left(\frac{3}{R} + \frac{2}{R+1} - 4 \right) , \tag{2.9}$$

where $R \equiv V_\perp / V_\parallel$. The accuracy of this model can be tested by filling in some numbers. The spin-orbit coupling constant in Co is approximately $\xi = 0.07\,\mathrm{eV/atom}$ [32]. Based on the DOS for a Co monolayer (see Fig. A.2) we take the in-plane bandwidth to be $2V_\parallel = 2\,\mathrm{eV}$ and the out-of-plane bandwidth $2V_\perp = 1\,\mathrm{eV}$, so that $R = 0.5$. Then, for a free-standing Co monolayer, Eq. 2.9 gives $\Delta E_{SO} = 2.0 \times 10^{-3}\,\mathrm{eV/atom}$, close to the value of $\Delta E_{SO} = 1.5 \times 10^{-3}\,\mathrm{eV/atom}$ found by Daalderop *et al.* [35] using ab-initio simulations. For a Co mono-

[2] The orbital momentum operators for the $3d$ orbitals are listed in Appendix B

layer sandwiched between Au slabs, the out-of-plane bandwidth increases so that $R = 1.53$ [36]. We then find $\Delta E_{SO} = -0.7 \times 10^{-3}$ eV/atom, again close to the value of $\Delta E_{SO} = -1.0 \times 10^{-3}$ eV/atom found in the literature [38]. In conclusion, this simplified perturbation model appears to give reasonable values for the magneto-crystalline anisotropy induced by spin-orbit coupling.

2.2 Magnetic anisotropy manipulation by an electric field

After establishing the origin of magnetic anisotropy, we would like to predict the effects induced by an applied electric field. An instructive method of computing such effects is to incorporate a Fermi level shift in the ligand field model described in section 2.1.2.5. Such an extension to the model has been developed; the results are presented in the current section. More advanced first-principles calculations in the literature are also discussed. Finally, alternative techniques of voltage control of magnetism are briefly discussed.

2.2.1 Band filling model

The calculations described in section 2.1.2.5 can be extended to incorporate an electric field effect, in the form of a Fermi level shift. Such an extension to the model should provide an instructive picture of electric field effects, as well as provide an order of magnitude of the expected anisotropy modification.

The Fermi level shift is incorporated by filling the minority band with $2.5 + w$ electrons, where w is the number of added electrons per atom. These added (or removed) electrons are assumed to be distributed evenly over the orbitals at the Fermi level. For a Au/Co(1ML)/Au sandwich ($V_{\parallel} = 1$ eV, $R = 1.53$, $\xi = 0.07$ eV/atom) calculations result in the dependence shown in Fig. 2.6. The easy axis is found to lie out-of-plane (denoted by a negative MCA energy) for small values of w, as expected. Furthermore, the electric field effect is seen to reverse sign around $w = 0$. This can be explained from Eq. 2.8; most mixing occurs if the minority band is exactly half full, which is the case for $w = 0$ (cf. Fig. 2.5). The sharpness of the transition is a result of the simplified DOS; the amount of mixing between orbitals would change more gradually if the full band structure was taken into account. Experiments do not show a sign reversal (see for example Fig. 1.5); apparently the minority band filling in a real cobalt system deviates enough from 2.5 to make $\Delta E_{\mathrm{SO}}(w)$ a monotonous function.

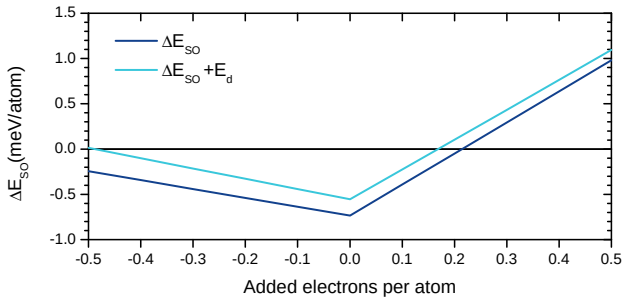

Figure 2.6: *Anisotropy energy resulting from the spin-orbit perturbation (dark line) and total anisotropy energy (including demagnetisation energy, light line), as a function of electrons added to a half-full minority band. By definition, a positive energy denotes an in-plane easy axis. The sharp change in slope around zero is caused by the simplified DOS: the anisotropy is largest if exactly half of the orbitals is filled (see Eq. 2.8).*

The demagnetisation energy can also be included in the model. As explained in section 2.1.1, the demagnetisation field for an out-of-plane magnetised thin film is given by $H_\mathrm{d} = -M$. The energy associated with this field equals $E_\mathrm{d} = -\frac{1}{2}\mu_0 H_\mathrm{d} M = \frac{1}{2}\mu_0 M^2$, where the factor $\frac{1}{2}$ is related to this being a form of self-energy. The energy per atom is found by multiplying by one atomic volume, equivalent to dividing by the material density n in atoms per m^3. As $M \equiv n\mu$, we find

$$E_\mathrm{d,atom} = -\frac{1}{2}\mu_0 n \mu^2, \tag{2.10}$$

with the effective magnetic moment per atom $\mu \approx 1.715\mu_\mathrm{B}$ for cobalt [31]. This magnetic moment depends on the band filling; it is maximum if the majority band is full and the minority band is empty, and zero if both bands are completely filled. We will assume here that μ scales linearly with w, with $\mu = 1.715\mu_\mathrm{B}$ for $w = 0$. Filling in the numbers, we find that the demagnetisation energy is a relatively small contribution to the total energy in this particular system; see Fig. 2.6. The easy axis for this system remains out-of-plane, despite the demagnetisation field. It should be stressed that this behaviour is only expected for ultrathin magnetic layers, as the relative contribution of the interfacial anisotropy is reduced with increasing layer thickness. The absolute value of the total anisotropy depends on the balance between the magneto-crystalline anisotropy and the shape anisotropy.

This has an important consequence: the *relative* electric field induced anisotropy modification is maximised for thin films that are near the in-plane to out-of-plane transition.

Finally, we calculate the expected order of magnitude of anisotropy modification in a typical device. To obtain an electric field at the Co interface, one side of the sandwich is replaced by a dielectric. This will of course affect the crystal field splitting, but this is ignored in this approximate calculation. For a voltage V applied across a dielectric of thickness d with dielectric constant ε, the number of added electrons per surface atom is:

$$w = \frac{1}{q_e}\alpha_{Co}^2 \varepsilon \frac{V}{d}, \tag{2.11}$$

with $\alpha_{\mathrm{Co}} = 0.25$ nm the interatomic distance and q_e the electron charge. For a typical dielectric (Al_2O_3, $\varepsilon \approx 20\,\varepsilon_0$) we thus find $w = 0.07$ electrons/atom per applied V/nm.[3] For the Co monolayer this amounts to a change in MAE of 0.24 meV/atom per applied V/nm; roughly 40% of total anisotropy. The Co monolayer, however, is an idealised system; all atoms are interface atoms so that the MCA and the band filling effect are at maximum. The thickness of the magnetic layer in a real device will typically be 1 nm, or roughly 5 monolayers. The effect of this is twofold: i) the carrier density is only affected at one interface, decreasing the voltage effect on the total anisotropy by a factor of 2, and ii) the relative interfacial contribution to the anisotropy energy per atom is reduced, by a factor of 5 in case of 5 monolayers. The electric field effect in 1 nm of Co is thus 10 times smaller than in the monolayer; 0.024 meV/atom per applied V/nm or $61.5\,\mathrm{fJV^{-1}m^{-1}}$. This order of magnitude corresponds well with available experimental data; Shiota *et al.* for example reported a value of $31.0\,\mathrm{fJV^{-1}m^{-1}}$ for a Au/FeCo(0.60 nm)/MgO system [15]. The developed extension to the ligand field model thus provides an accurate estimate for the effect of electric-field-induced anisotropy modification.

2.2.2 Ab-initio simulations

The band filling model described in the previous section is highly instructive, and gives an indication of the expected order of magnitude of electric field effects in thin films. The most important parameter, the anisotropic field splitting

[3] Note that all electrons are assumed to end up in the $3d$ band. The number of states at the Fermi level in the $4s$ band is relatively negligible.

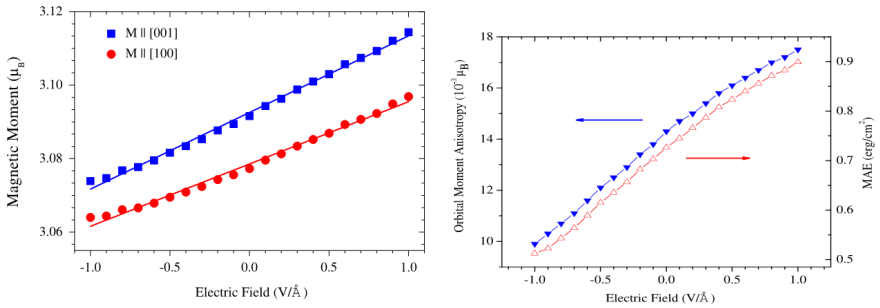

Figure 2.7: *Ab-initio calculation of electric field effect on a) the total magnetic moment in lying out-of-plane ([001 direction]) and in-plane ([100] direction) and b) the orbital moment anisotropy of a surface atom, in a 15 monolayers thick Fe slab. Figures taken from [39].*

ratio $V_\perp/V_\parallel$, is taken as an input for the model. To calculate this ratio, and other properties of solids, the detailed band structure must be evaluated through intricate simulations. Since crystals are essentially many-particle systems with many degrees of freedom, such simulations still rely heavily on approximations. A popular approach is the augmented plane wave method, based on the idea that crystal wavefunctions can be described as atomic functions near the ions and as plane waves in between. The energy landscape is often described by a so-called muffin-tin potential: spherical energy wells below a critical radius on each atom, and a constant potential in between. Properties such as the magneto-crystalline anisotropy have been computed using such simulations in the past decades, with a varying degree of success. Some results are presented here, particularly on the topic of electric field effects in transition metal systems.

The anisotropy of Fe and Ni was first calculated in pioneering simulations by Gay and Richter [40] in 1986, showing PMA for a free-standing Fe monolayer. Later simulations [41] showed PMA for an Fe layer sandwiched between Au, Ag, or Pd. The change of anisotropy as a function of band filling was computed in the 90s [42, 43], and was found to be anything but linear for large variations in electron density.

Results highly relevant to this report were presented by Duan *et al.* [39], who directly calculated electric field effects in transition metal films using the VASP package. They conclude that the effect originates from spin-dependent screening of the electric field (suggested by S. Zhang [44]), which leads to notable changes

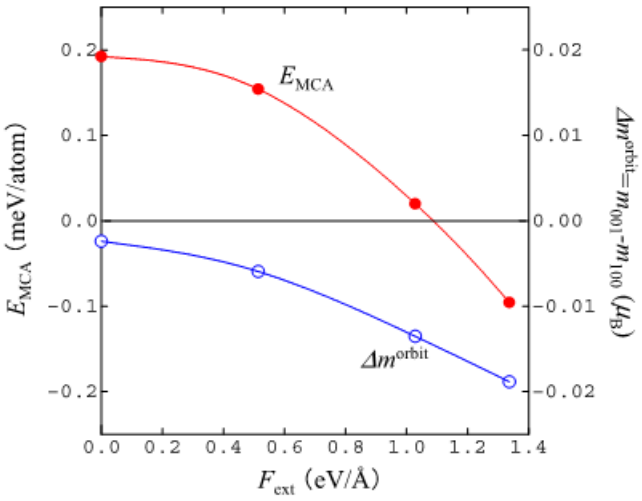

Figure 2.8: *Magnetic anisotropy energy and anisotropy of orbital moment as a function of electric field in a Fe(001) monolayer. Figure taken from [46].*

in the surface magnetization and the surface magnetocrystalline anisotropy. The field-dependence of both quantities is given in Fig. 2.7, and is found to be linear in the range of volts per nanometre. The magnitude and sign of the effect were found to depend on the density and spin polarization of the charge carriers near the Fermi level of the ferromagnetic metal film. Similar calculations carried out by Tsujikawa *et al.* [45] for an Fe/Pt surface yielded similar results.

A somewhat different result was reported by Nakamura *et al.* [46], who calculated electric field effects in the transition metal monolayers. Their result is presented in Fig. 2.8. The electric field effect is attributed to small changes in band structure, in which p orbitals play a key role. The effect is seen to be much stronger than reported by Duan *et al.*, which may be attributed to the much smaller slab thickness (1 vs 15 monolayers). According to Nakamura *et al.* the easy axis of a Fe monolayer can be rotated in-plane by application of roughly 10 V/nm. Note that the sign difference in the electric field effect between Nakamura and Duan is due to opposite definition of the positive field direction. A final observation from Fig. 2.8 is that Nakamura predicts an anisotropy modification of roughly -0.02 eV/atom per applied V/nm. The magnitude of this first-principles calculation thus agrees well with the band-filling ligand field model outcome presented in section 2.2.1.

2.2.3 Alternate methods of magnetisation manipulation by an electric field

Concluding the section on anisotropy modification by electric field, some alternate mechanisms to achieve such control are introduced to provide a broader perspective. It has long been realised that electric currents consume a large amount of energy relative to the thermal stabilization energy for magnetic bit information, which is often estimated as $(50 - 60) \times k_{\mathrm{B}}T$ [47]. Voltage is a much more promising candidate for future writing techniques, as the power consumption is drastically smaller. In conventional electronics, this is reflected by the success of complementary metal–oxide–semiconductor field-effect transistor technology. In spintronics, many experimental efforts have been made to achieve voltage control of magnetism, aside from anisotropy modification in ultrathin films. The current section briefly describes some of these alternate techniques.

Magnetostriction

Magnetic materials can deform mechanically under application of a magnetic field; a phenomenon known as *magnetostriction*. The effect can be inverted to allow for the manipulation of magnetism by mechanical strain. This mechanical strain can be introduced by means of the *inverse piezoelectric effect*; deformation of a crystal under application of an electric field caused by electric dipole moments in certain solids. Several devices have been proposed based on magnetostrictive effects, including an MRAM designed as early as 1982 [48]. Research efforts continue in more recent years [49] but practical applications remain to be demonstrated.

Multiferroics

Similar to ferromagnetic materials, *ferroelectric* materials exist exhibiting a stable and switchable electrical polarization. A very interesting class of materials is that of *multiferroics*, exhibiting both ferromagnetic and ferroelectric properties. Work in this area can be traced back to pioneering research in the 1950s and 1960s, but there has been a recent resurgence of interest driven by long-term technological aspirations [50, 51]. The reader is referred to the review article by Eerenstein *et al.* [52] for more background on multiferroics. A recent advance in this field that is worth noting was made by Sahoo *et al.* [53], who achieved a 20% coercivity change

via electrical control at room temperature in solid state ferroelectric-ferromagnetic heterostructures. Another interesting application is the transfer of domain wall patterns from ferroelectric to ferromagnetic materials demonstrated very recently by Lahtinen *et al.* [54].

Magnetic semiconductors

As mentioned in section 1.3.1, direct electric field control of ferromagnetism was first achieved in semiconductors [14]. The ferromagnetism in these materials is mediated by the carriers [55], and can thus be modified through application of a gate voltage. This has been shown to result in a change of Curie temperature [14], coercivity [56], and magnetic anisotropy [57], but the very low Curie temperature (<200 K) remains a serious shortcoming [26].

2.3 Magnetisation reversal

In the previous sections, the phenomenon of magnetic anisotropy has been discussed in detail. The current section aims to describe how this anisotropy affects a typical experiment, in which the magnetisation is reversed by application of a magnetic field. As explained in section 2.1, the total energy of a magnetic system contains four main contributions: the exchange energy, the demagnetisation energy, the magneto-crystalline anisotropy energy (MAE), and the Zeeman energy. The balance between these energies determines the local magnetisation within the sample. An applied electric field can change both the magnetic moment and the anisotropy, affecting all these energies.

Suppose now that we place a fully out-of-plane magnetised thin film in an external magnetic field, directed opposite to the magnetisation direction. Increasing the magnitude of this magnetic field raises the Zeeman energy ($\varepsilon_z = -\mu_\mathbf{0}\mathbf{M} \cdot \mathbf{H}$) across the sample. Minimisation of the total energy therefore requires the magnetisation to align to the external magnetic field; a process referred to as *switching* or *magnetisation reversal* if the magnetisation direction is rotated by 180°. This switching process can be frustrated by the other magnetic energies: the anisotropy energy, for example, is increased if the magnetisation is tilted away from the easy axis (Eq. 2.1). Magnetisation reversal therefore becomes a complex process, depending on the exact local balance between the various magnetic energies. Three limiting cases are discussed below: uniform switching,

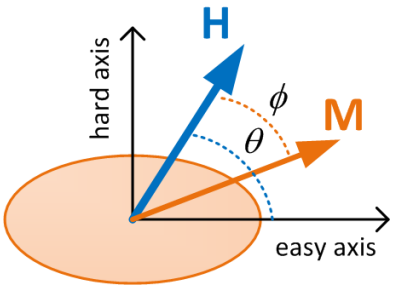

Figure 2.9: *Relevant vectors and angles in the Stoner-Wohlfarth model applied to a single-domain ellipsoid.*

domain nucleation, and domain wall motion. A specific form of thermally activated domain wall motion is finally discussed in more detail, as it is relevant to the experiments presented in this report.

2.3.1 Uniform switching

The most simple treatise of magnetisation reversal, known as the Stoner-Wohlfarth model [58], considers a single-domain ferromagnet. The magnetisation is described by a single *macrospin*, the orientation of which depends on the applied magnetic field and the anisotropy. Minimisation of the energy in such a system shows the expected magnetisation direction in equilibrium. Such a description is only valid for small magnetic particles, but it provides some insight into the switching behaviour of more complex systems.

There is no exchange energy in a single-domain system, as neighbouring spins are by definition all aligned. The shape and magneto-crystalline anisotropies are uniform and can be combined into an effective uniaxial anisotropy K_{eff}. The anisotropy energy density (Eq. 2.1) and the Zeeman energy density then describe the macrospin system energy density, given to first order by:

$$\varepsilon = K_{\text{eff}} \sin^2(\phi - \theta) - \mu_0 M_s H \cos(\phi), \tag{2.12}$$

where M_s is the saturation magnetisation of the sample, H is the magnitude of the applied magnetic field, θ is the angle between the applied field and the easy axis, and ϕ is the angle between the applied field and the magnetisation. The relevant angles and vectors are depicted in Fig. 2.9.

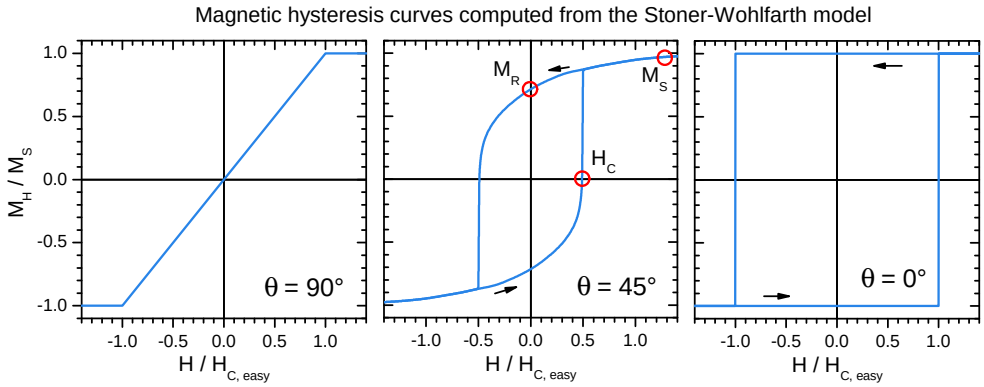

Figure 2.10: *Plots of the magnetisation as a function of applied magnetic field, as typically computed using the Stoner-Wohlfarth model for different angles ϕ between the applied field and the easy axis. Arrows indicate the direction of field incrementation. The magnetisation is plotted as the component M_{H} of the magnetisation along the applied field direction, normalised to the saturation magnetisation M_{S}, with $M_{\mathrm{H}}/M_S = \cos\phi$ in Eq. 2.12.*

Minimisation of Eq. 2.12 allows one to predict the magnetisation direction as a function of H for certain field angle θ if K_{eff} and M_s are known. Typical numerical results of this procedure are depicted in Fig. 2.10 for $\theta = 90°$ (field along the hard axis), $\theta = 45°$, and $\theta = 0°$ (field along the easy axis). Three quantities which are often presented in experimental results are indicated in the middle panel of Fig. 2.10. The *saturation magnetisation* M_S has already been mentioned; it is the maximum attainable magnetisation as the name suggests. The *coercive field* or *coercivity* H_C is the applied magnetic field required to reduce the magnetisation to zero (or flip it) after saturation. This quantity is strongly related to the magnetic anisotropy, as it depends on the energy required to rotate the magnetisation away from the easy axis. Finally, the *remnant magnetisation* M_R is the magnetisation that remains when reducing the applied field to zero after saturation. A more practical quantity is the *remanence* M_R/M_S, which is often given as a percentage.

Finally, it should be noted that the Stoner-Wohlfarth model can also be used to compute the anisotropy of a sample from experimental data. The mentioned energy minimisation procedure can be used to compute K_{eff} from $\phi(H)$ measurements at various angles θ, if M_s is known. Of course, this approach is only valid if the sample actually switches through a uniform rotation of the magnetisation, which is usually only the case for very large angles θ.

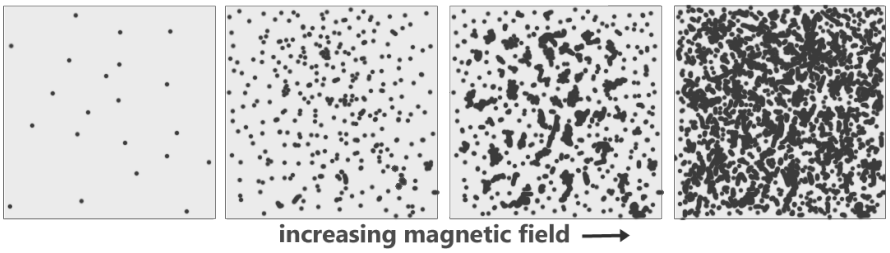

Figure 2.11: *Sketch of magnetisation reversal through domain nucleation. The easy axis points out of the sample plane; the dark dots in the figure represent reversed domains. If the propagation field is larger than the nucleation field, individual domains do not expand but can cluster together to form larger domains.*

2.3.2 Domain nucleation

In larger systems, including thin films, magnetisation reversal generally does not occur through a uniform switching process. Instead, reversal is initiated at points of reduced anisotropy arising from local defects or film edges. This process is referred to as *nucleation*, generating *domains* of different magnetic orientation. The magnetic field at which this first occurs is referred to as the *nucleation field* H_N. The boundary between two domains, commonly called a *domain wall* (DW), is very thin in perpendicularly magnetised materials: the magneto-crystalline anisotropy dominates over the exchange interaction, so that sharp changes in the magnetisation are favoured. Nucleation in perpendicularly magnetised materials thus creates well-defined domains, as illustrated in the first panel of Fig. 2.11.

After nucleation of the first reversed domains, the switching process can continue in two ways. Further domains can be nucleated, clustering together to form larger domains until the entire sample has switched. This type of magnetisation reversal is illustrated in Fig. 2.11. Another manner of switching involves growth of the nucleated domains, as discussed in the next section.

2.3.3 Domain wall motion

As magnetic domains change in size, the interfaces between them are displaced. One can thus view magnetic switching processes in terms of *domain wall motion*. This type of switching requires domains to grow beyond the low-anisotropy defects where they nucleated, with the advantage of costing less exchange energy than pure nucleation. The magnetic field required for domain wall motion is commonly

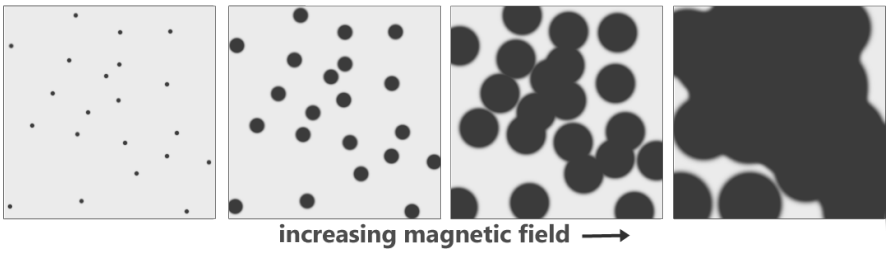

Figure 2.12: *Sketch of magnetisation reversal through domain wall motion. The easy axis points out of the sample plane; the dark dots in the figure represent reversed domains. If the propagation field is smaller than the nucleation field, individual domains expand after nucleation.*

referred to as the *propagation field* H_P. If $H_P \leq H_N$, magnetisation reversal will occur though domain wall motion after the initial nucleation of reversed domains, as illustrated in Fig. 2.12.

Domain wall motion can be induced by a magnetic field, but also by electric currents due to spin-transfer torque [59]. The latter mechanism makes DW motion suitable for technological applications; interesting logic [8] and storage [6] devices have been proposed and generated significant scientific interest.

The DW velocity depends on the driving force, be it a magnetic field or an electric current. The crucial mechanism underlying domain wall motion is the competition between an elastic force (tending to keep the wall straight) and a pinning force (tending to adjust the wall to local disorder) induced by impurities, thickness variations, etcetera. The elastic force in ferromagnets is the exchange interaction, favouring parallel spins and short domain walls. This tendency may be disturbed locally by disorder, creating preferred domain wall positions known as *pinning sites*. These local energy minima become more relevant if the driving force behind domain wall motion is relatively small, causing sections of the domain wall to move in small discrete steps. Domain wall transport is said to be in the *creep regime* in this case. For higher driving forces, the local disorder becomes less relevant and the domain wall velocity depends linearly on the driving force. Domain wall motion is then said to be in the *flow regime*. The transition between the two regimes, where the driving force is roughly equal to the pinning force, is referred to as the *depinning regime*. A theoretical velocity curve depicting the three regimes is shown in Fig. 2.13.

In the experiments described in this report, the driving force is small and DW

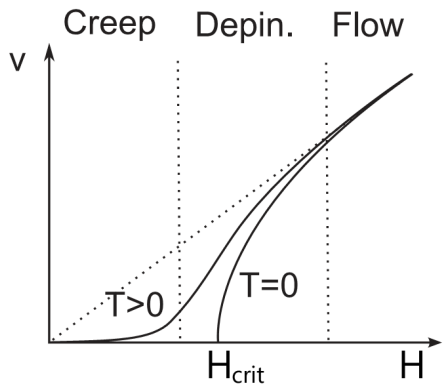

Figure 2.13: *Theoretical variation of the domain wall velocity v as a function of the driving field H for zero and finite temperature. Figure taken from [60].*

motion appears mainly to occur in the creep regime. The physics in this regime are discussed in the next section, leading to a derivation of the velocity curve in the creep regime depicted in Fig. 2.13.

2.3.4 Domain wall creep

The movement of a domain wall in the creep regime can be theoretically described using creep theory, which will be outlined here. The effect of an applied electric field on this motion will also be discussed.

Creep theory applies to a wide range of phenomena, and was originally developed to describe vortices in superconductors.[61] The basic idea is that movement of an interface occurs in small discrete steps of varying size. The system is described in general as a d-dimensional interface moving through a two-dimensional, weakly disordered medium in n transverse directions. Note that weak disorder implies a small spread in the pinning site energies. In our case, the magnetic medium is only about one nanometre thick, so that we can approximate the interface (DW) as a line ($d = 1$) moving in one transverse direction ($n = 1$).

We now consider a domain wall segment of length L, having some displacement u from the mean position of the domain wall, as depicted in Fig. 2.14. The free energy $\mathcal{F}(u, L)$ of this segment contains contributions from the elastic energy, pinning energy and Zeeman energy. These can be expressed as follows [62]:

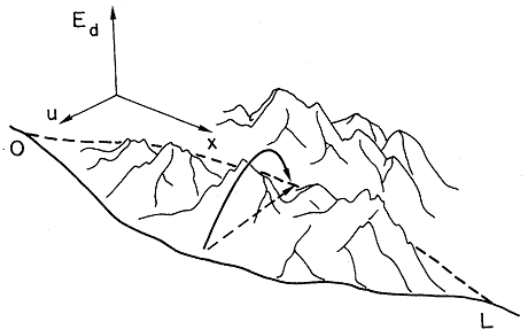

Figure 2.14: *Domain wall displacement though a disordered potential landscape. A segment of length L is displaced over a length u(L) between two low-lying metastable states. Figure taken from [61].*

$$\mathcal{F}(u,L) = \varepsilon_{\mathrm{el}}\frac{u^2}{L} - \sqrt{L\xi^2\Delta} - 2\mu_0 H M_s t L u. \tag{2.13}$$

The first term in this expression, the elastic energy, results from the exchange interaction. The domain wall energy density per unit length, $\varepsilon_{\mathrm{el}}$, can be calculated for Bloch type walls as $\varepsilon_{\mathrm{el}} = 4t\sqrt{AK}$, where A is the exchange stiffness, K the anisotropy constant, and t the film thickness. Clearly, the elastic force favours a straight wall with $u = 0$. The second term in 2.13 is the pinning energy, where ξ is the characteristic length of the disorder potential and Δ is a pinning strength scaling factor. This can further be expressed as $\Delta = f_{\mathrm{pin}}^2 n_i \xi$, with f_{pin} the local pinning force and n_i the surface density of pinning centres. Note that the pinning energy depends on *fluctuations* in the pinning site density, which is reflected by the square root dependence of L. Finally, the last term in 2.13 is simply the Zeeman energy with M_s the saturation magnetisation and H the applied magnetic field.

For a typical displacement between two pinning sites ($u = \xi$) we find $E_{\mathrm{el}} \approx E_{\mathrm{pin}}$ for a characteristic segment length L_c, known as the Larkin length:

$$L_c = \left(\varepsilon_{\mathrm{el}}^2 \xi^2 / \Delta\right)^{1/3}. \tag{2.14}$$

If a domain wall is narrower than L_c (i.e. in a narrow nanowire), it behaves as a zero-dimensional particle and may be described using a simple one-dimensional hopping model. At lengths $L > L_c$, the domain wall can adjust itself elastically to the potential landscape, and its behaviour must be described using creep theory. The wall may be seen as a succession of segments of length L_c that move

independently from one another. The effective pinning energy barrier U_c can then be expressed as the pinning energy of a segment of length L_c:

$$U_c = \left(\xi^5 f_{\text{pin}}^2 n_i \varepsilon_{\text{el}}\right)^{1/3}. \tag{2.15}$$

It is also possible to calculate the so-called critical field H_{crit}, which is the minimum required field for wall movement at $T = 0\,\text{K}$. Equating the Zeeman force to the pinning force for $L = L_c$ yields:

$$H_{\text{crit}} = \frac{\varepsilon_{\text{el}}\xi}{2\mu_0 M_s L_c^2 t}. \tag{2.16}$$

For finite temperatures, movement still occurs in the creep regime ($H \ll H_{\text{crit}}$) due to thermal activation. It is possible to derive an expression for the domain wall velocity in this regime; see for example [62] or [61] for a more thorough derivation. It is found that

$$v(H) \propto \exp\left[-\frac{U_c}{k_{\text{B}}T}\left(\frac{H_{crit}}{H}\right)^{\mu}\right], \tag{2.17}$$

where μ is related to the dimensionality of problem; in this case $\mu = 1/4$. This equation is known as the *collective creep law*.

Of course, the domain wall velocity depends on more than just the applied magnetic field. For this report, it is particularly interesting to look at the influence of the anisotropy K on the domain wall velocity, as this is the property we intend to modify using an electric field. The anisotropy affects two variables used in the previous discussion; ε_{el} and f_{pin}. It has already been noted that $\varepsilon_{\text{el}} \propto K^{1/2}$ for Bloch walls. A useful approximation for the role of anisotropy in the pinning force f_{pin} can be obtained by examining local variations. Following the approach by Lemerle *et al.* [62], we approximate these variations as steps between atomically flat terraces with thickness t_1 and t_2. The characteristic length ξ in this case is the step to step spacing. To first order, the local pinning force is given by:

$$f_{\text{pin}} = \frac{t_2\gamma_2 - t_1\gamma_1}{2\delta}, \tag{2.18}$$

where $\gamma_i = 4\sqrt{AK_i}$ is the Bloch wall energy density for thickness t_i and $\delta = \left\langle\sqrt{A/K_i}\right\rangle$ is the average of the domain wall thickness before and after the step.

The relation between the local anisotropy K_i and the macroscopic anisotropy K is not necessarily trivial. We can, for example, assume that pinning is caused

solely by thickness fluctuations so that $K_i = K$. Under this assumption, it is evident from 2.18 that $f_{\text{pin}} \propto K$. We then find that $L_c \propto K^{-1/3}$, $U_c \propto K^{5/6}$, and $H_{\text{crit}} \propto K^{7/6}$, so that $v(K) \propto \exp\left[-K^{9/8}\right]$.

Finally, it is interesting to express the domain wall velocity as a function of electric field. Based on recent experimental findings [18, 19, 15, 20, 21], it is reasonable to assume a linear relation between the anisotropy constant K and the applied voltage, at least in the experimentally accessible voltage regime. We can express this dependency as

$$K(V) = (1 + \alpha V)\, K_0, \tag{2.19}$$

where K_0 denotes the anisotropy constant for $V = 0$ and α is a newly introduced coefficient (unit V^{-1}). The local pinning force then becomes:

$$f_{\text{pin}}(V) = \frac{2t_2\sqrt{A(1+\alpha V)K_2} - 2t_1\sqrt{A(1+\alpha V)K_1}}{2\left\langle\sqrt{A/(1+\alpha V)K_i}\right\rangle} \propto (1 + \alpha V),$$

whereas $\varepsilon_{\text{el}} \propto (1 + \alpha V)^{1/2}$. It is then easily shown that $U_c \propto (1 + \alpha V)^{5/6}$ and $H_{\text{crit}} \propto (1 + \alpha V)^{7/6}$, so that $v(V) \propto \exp\left[-(1 + \alpha V)^{9/8}\right]$. Since the largest electric field effects reported in the literature are of the order of 10% [20], we can drop the exponent 9/8 for simplicity without causing a significant error (a few percent at most). The following relation is thus expected to be valid for experimentally obtained electric field effects:

$$v(H, V) \propto \exp\left[-C\,(1 + \alpha V)\, H^{-1/4}\right], \tag{2.20}$$

where all constants are absorbed into $C \equiv \frac{1}{k_{\text{B}}T} U_c H_{crit}^{1/4}$. This equation is the main result of the current section, and will prove to be very useful in the analysis of domain wall motion experiments (see Chapter 4).

Note that an applied electric field is also expected to affect the saturation magnetisation, since the Fermi level determines the amount of minority spins (see for example section 2.2.1). This directly affects H_{crit}, as can be seen from Eq. 2.16, so that $v(V) \propto \exp\left[-(1 + \alpha V)^{9/8}\,(1 + \beta V)^{-1/4}\right]$. This modification, however, can be absorbed into the linearisation approximation for small field effects, so that Eq. 2.20 still holds. Finally, the saturation magnetisation also affects the demagnetising field, modifying the effect anisotropy K. This does not

alter the calculation: all anisotropy modifications are absorbed into Eq. 2.19, which describes the effect of an applied voltage on the *total* anisotropy.

2.4 Summary

The presented theoretical work is now briefly summarised. The concept of magnetic anisotropy was introduced, distinguishing between shape and crystalline contributions. The origin of magnetic crystalline anisotropy was subsequently described in more detail. A discussion of atomic orbitals and spin-orbit coupling resulted in a ligand field model, relating interfacial magnetic anisotropy to anisotropy of the bonding environment. This ligand field model was extended to include a Fermi level shift, estimating the expected order of magnitude of a voltage-induced anisotropy modification. More advanced calculations in the literature were found to agree with the obtained result.

The process of magnetisation reversal in thin films was subsequently described in a broad fashion. A more detailed analysis of domain wall creep was presented, linking the domain wall propagation velocity to the magnetic anisotropy. This analysis finally led to an expression describing the domain wall velocity as a function of applied voltage and magnetic field.

Chapter 3

Methodology

The composition of samples and the fabrication process are discussed in this chapter, as well as the used measuring techniques. The sample fabrication is discussed in relative detail, explaining the choice of materials and describing fabrication to the point where experiments may be reproduced. The used measuring techniques, relying on the magneto-optic Kerr effect (MOKE), are discussed in a very general manner as a deeper understanding of the underlying physics is not relevant to the experiments discussed in this report.

3.1 Sample composition and fabrication

The primary experimental goal of this project is to modify interfacial magnetic anisotropy by changing the Fermi level in a thin magnetic layer. Samples should thus feature a ferromagnetic layer which also functions as a capacitor plate, allowing for the accumulation of charge at its surface. This desired geometry is sketched in Fig. 3.1. A dielectric layer is deposited directly on top of a thin ferromagnetic layer, followed by a top electrode. Applying a voltage across the electrodes should result in charge accumulation at the ferromagnetic/dielectric interface, affecting the interfacial magnetic anisotropy. An electric field cannot modify bulk material properties, as such a field is screened by valence electrons within a few monolayers. The ferromagnetic layer must thus be extremely thin, a few monolayers at most. The remainder of this section discusses the used materials and fabrication process.

3.1.1 Materials

Perpendicularly magnetised ferromagnetic layers are used in this project, as they promise advantages in technological applications as explained in section 1.2. Furthermore, the relative anisotropy modification induced by an applied electric field is expected to be largest for films near the in-plane to out-of-plane transition,

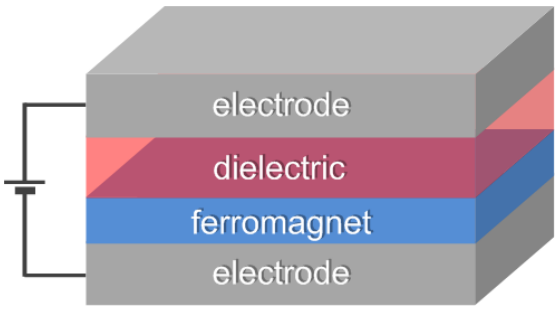

Figure 3.1: *Sketch of the capacitor-like structure that is used to obtain a Fermi level shift in a thin ferromagnetic layer.*

as explained in section 2.2.1. A material combination that shows perpendicular magnetic anisotropy (PMA) and contains a ferromagnetic/dielectric interface is Pt/Co/AlOx. This material is especially interesting to domain wall motion applications: high current-induced domain wall velocities were recently reported in Pt/Co/AlOx [28], possibly related to effects other than spin-transfer torque [29]. Another thin layer of Pt can function as a top electrode and capping layer, creating the capacitor structure depicted in Fig. 3.1 using Pt/Co/AlOx/Pt. Experiments were performed using this material stack, as well as some variations using similar materials.

3.1.2 Growth technique

Samples are fabricated using a DC magnetron sputtering process, which allows for thin layers to be grown with sub-nanometre precision. The CARUSO ultra-high vacuum (UHV) sputtering facility at the Physics of Nanostructures group features six deposition sources placed above a rotatable sample stage. This allows for moderately complex material stacks to be grown. The base pressure inside the system is roughly 3×10^{-8} mbar.

The sputtering technique is discussed extensively in the literature; only the basic idea is described here. Small discs of highly pure materials, referred to as targets, are loaded facing downward into a vacuum vessel. Just below each target is a ring-shaped anode. Samples are loaded facing upward onto a rotatable stage, about 20 cm below the targets. A small flow of argon gas is then admitted to the chamber, raising the pressure to roughly 1×10^{-2} mbar. A high voltage is applied between a target and its anode, accelerating argon ions towards the target surface.

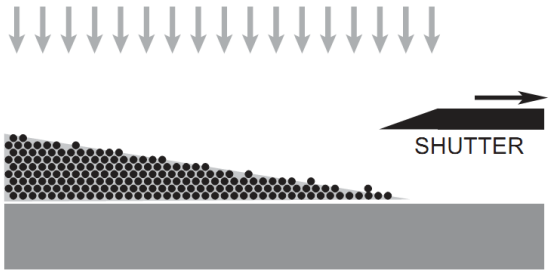

Figure 3.2: *Schematic illustration (not to scale) of the growth of wedge-shaped samples using a wedge mask. Figure taken from [63].*

These ions knock out single atoms of the target material, which whirl down and condense on a sample substrate. The growth rate is of the order of 1 Å/s, making this relatively simple technique suitable for depositions requiring sub-nanometre control of the layer thickness.

Samples can be structured during deposition by using masks; metal plates with cut-out patterns in close proximity to the substrate surface. A mask shields sections of the substrate from incoming atoms, so that deposition takes place in a predefined pattern. Two masks were used extensively during this research project: a *wedge mask* and a *junction mask*.

The wedge mask is basically a sharp-edged shutter which is moved along the substrate surface during deposition. This creates a thickness gradient in the deposited layer, as illustrated in Fig. 3.2. Samples containing such layers, referred to as *wedges*, are extremely useful in studying thickness-dependent material properties.

Actual capacitor-like stacks as depicted in Fig. 3.1 are fabricated using a junction mask, originally intended for magnetic tunnel junction fabrication. The junction mask is a 0.5 mm thick tungsten plate with a cut-out pattern of lines, as depicted in Fig. 3.3a. Each line is approximately 200 μm wide. The mask can be rotated in-situ by 90°, allowing for junction structures to be deposited in a two-step procedure as shown in Fig. 3.3b. Complete samples can thus be fabricated in a single vacuum, greatly simplifying the production process.

The masked sputtering procedure does have some drawbacks. In sputtering deposition, the mean free path of atoms is several times smaller than the source-substrate distance. As a result of scattering, atoms do not all arrive at the substrate at normal incidence. Instead, the amount of deposited material depends on the

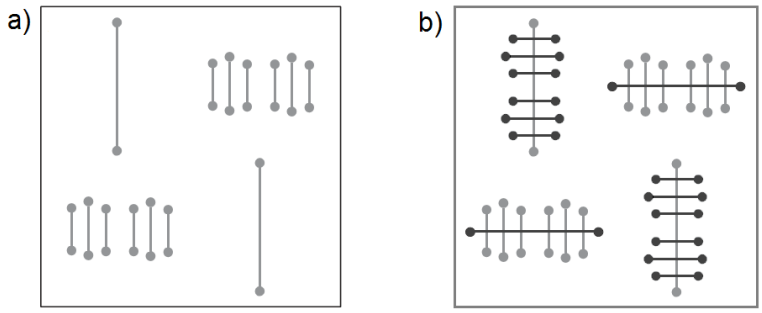

Figure 3.3: *a) Top view of junction mask layout. The mask measures 40x40 mm; the wires are approximately* 200 μm *wide. b) Top view of junction structures, obtained after the two-step deposition procedure.*

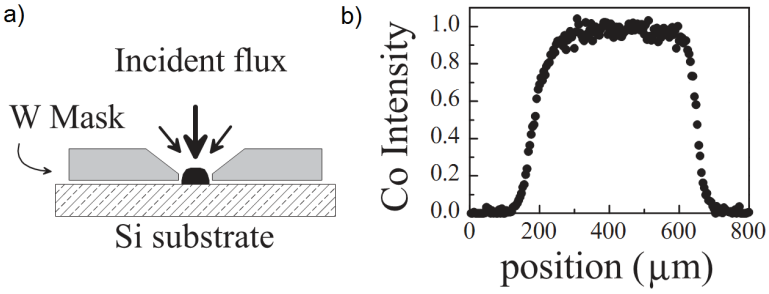

Figure 3.4: *a) Side view of the masked sputtering procedure (not to scale) and b) the resulting thickness profile for a 50 nm thick Co stripe, measured by EDX. Figure taken from [63].*

incident angle, roughly following a cosine dependence (see [63], section 3.2.1). This affects the masked sputtering process, as illustrated in Fig. 3.4. The amount of material deposited in the unmasked areas is reduced, especially close to pattern edges, because atoms incident at a small angle to the surface are blocked. This creates rounded edges in deposited structures, as seen in Fig. 3.4b, which will prove to be relevant in experiments. Furthermore, less material is deposited overall than calibration based on uniform film deposition suggests. Earlier measurements suggest this *tooling factor* is approximately 3/4 [63] in our set-up, but recent measurements contradict this result and suggest a tooling factor closer to unity. Layer thicknesses mentioned in this report are therefore *not* corrected for a tooling factor.

3.1.3 Oxidation procedure

A plasma oxidation chamber is attached to the sputtering system, allowing for controlled plasma oxidation of deposited layers without leaving the vacuum environment. The plasma oxidation chamber is also used to clean samples prior to deposition, by exposing the substrate to a reactive oxygen plasma for five minutes.

The base pressure in the oxidation chamber is approximately 1×10^{-9} mbar. Oxidation takes place in a pure oxygen environment, at a pressure of 1×10^{-1} mbar. A plasma oxidation process is used for all samples described in this report, increasing the oxygen penetration depth by ionising and accelerating oxygen molecules. Relevant operating parameters include a voltage limit of 2 kV, a steady current of 15 mA, and an oxidation time of 10 minutes.

3.1.4 Junction fabrication

Concluding the sample fabrication section, the production of a typical junction sample (in this case Pt/Co/AlOx/Pt) is now briefly discussed. A schematic overview of the produced structure is presented in Fig. 3.5. Fabrication starts by cutting and cleaning a 10x10 mm silicon substrate, covered with a thick oxide layer. The sample is then loaded into the CARUSO sputtering system and exposed to an oxygen plasma for five minutes to clean it. A 220 μm wide stripe of Pt (4 nm) and Co (~1 nm) is then deposited through the junction mask (Fig. 3.3a, top left pattern). A 1.5 nm thick layer of Al is subsequently deposited across the entire sample, completely covering the bottom electrode. Next, the sample is oxidised in the oxidation chamber, with the intention of creating an insulating AlOx layer. [1] This procedure is then repeated: another 1.5 nm thick layer of Al is deposited across the entire sample and subsequently oxidised. It was established in exploratory experiments that this second oxide layer significantly increases the dielectric layer resistance. Finally, 180 μm wide stripes of Pt (4 nm) are deposited through the junction mask (Fig. 3.3a, top right pattern) functioning as both top electrodes and junction capping layers. The sample is finally unloaded from the deposition machine. Exposure to air is expected to be of little consequence at this moment, as the sample is already covered in a heavily oxidised layer of aluminium. In many cases, samples were finally annealed (exposed to high temperature, say

[1] It should be noted that the implantation of oxygen increases the thickness of the Al layer; the thickness increase is estimated at 25% by comparing the densities of Al and Al_2O_3.

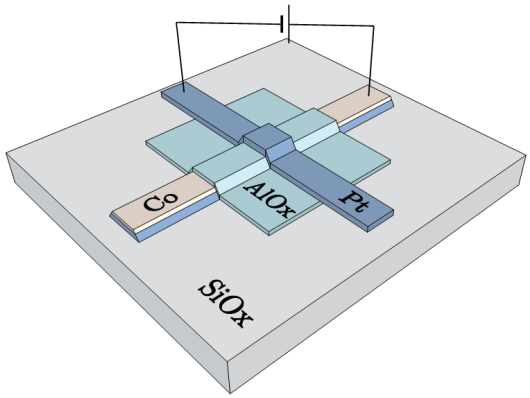

Figure 3.5: *Schematic overview of a Pt/Co/AlOx/Pt junction, not to scale. The bottom strip consists of a Pt layer covered by a Co layer. An AlOx layer is deposited on top of this strip, covering the entire substrate (shown here as a smaller region of material for clarity). A Pt crossbar is finally deposited on top.*

300 °C) at atmospheric pressure for 30 minutes, in absence of a magnetic field, to improve magnetic properties.

3.2 Magneto-optic Kerr effect

All magnetic measurements presented in this report were performed using the magneto-optic Kerr effect (MOKE) as a probing tool. In MOKE measurements, reflected polarised light is analysed to obtain a measure of the local surface magnetisation, as illustrated in Fig. 3.6. Linearly polarised light can be thought of as composed of equal parts of left- and right-circularly polarised light. Referring to the polar MOKE geometry depicted in Fig. 3.6, reflection at a magnetic surface is seen to change the balance between the two circular polarisation components, resulting in a change in polarisation angle and ellipticity. This change can easily be detected, and provides a measure of the local magnetisation at the position of the reflection.

Quantum-mechanically, the Kerr effect originates from coupling between the angular momentum of photons and electrons. The electron angular momentum is in turn dependent on the magnetisation through spin-orbit coupling, as explained in section 2.1.2.1. Classically, the interaction between photons and electrons in a conductor can be understood using the Lorentz force. The electric field component

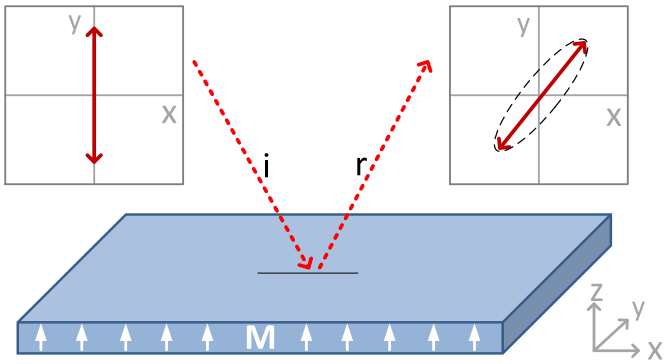

Figure 3.6: *Schematic overview of the magneto-optic Kerr effect. A linearly polarised incoming light beam (i) reflects from a magnetic surface, affecting the polarisation of the reflected beam (r). This particular geometry is referred to as polar MOKE, suitable for probing out-of-plane magnetisation. The angle of the incoming light beam is exaggerated; in actual polar MOKE applications light of normal incidence is used, which simplifies data analysis.*

of the incident light excites electron motion in the metal, which is affected by the local magnetic field through a Lorentz force. This rotational effect is observed in the polarisation of the reflected light.

The Kerr effect is usually employed to measure magnetisation reversal in an applied magnetic field, yielding $M(H)$ curves resembling the sketches depicted in Fig. 2.10. A highly focussed laser beam can be used in such measurements, which is especially useful to probe magnetic behaviour in samples containing lateral variations such as wedges. It is difficult to establish the absolute value of the magnetisation from MOKE data, but hysteresis loops provide useful information (see section 2.3.1), even if the magnetisation axis is not calibrated.

An alternative experimental technique employing MOKE is Kerr microscopy, providing a spatially resolved overview of a magnetic switching process. A Kerr microscope is essentially a conventional microscope with added polarisation filters, allowing for magnetic imaging using the Kerr effect. An Evico Kerr microscope was used in this research project, which contains a CCD camera allowing for digital acquisition of images at 16 frames per second. The magnetisation is visualised as a brightness variation, as depicted in Fig. 3.7. The combination of spatial resolution and time-resolved capabilities makes this technique especially useful in investigating domain nucleation and domain wall motion.

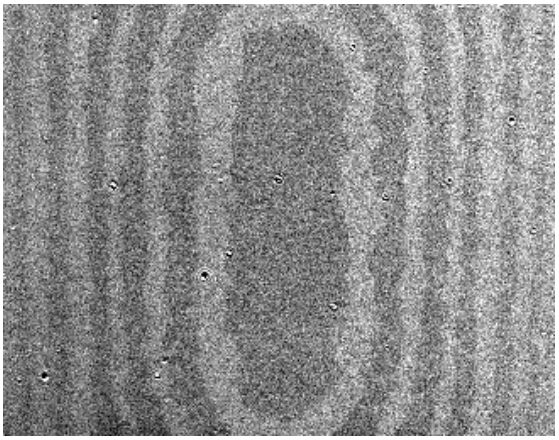

Figure 3.7: *A Kerr microscopy image, using polar MOKE to visualise out-of-plane domains in a magnetic sample as regions of different brightness. The darker areas in this image indicate an upward magnetisation (out of the paper plane), whereas the lighter areas indicate downward magnetisation.*

Chapter 4

Results

In the course of this research project, experiments were carried out aiming to demonstrate electric field effects in perpendicularly magnetised materials. After achieving this goal, the electric field effect was explored in new ways, providing exciting observations that will be presented in the current chapter.

The relevant experimental results are divided into seven sections. First, efforts were made to determine a suitable sample composition and fabrication procedure, the results of which are presented in section 4.1. After a successful stack composition and fabrication procedure were established, the magnetic behaviour of the samples under application of an electric field was examined using polar MOKE measurements. The resulting hysteresis loops are presented and discussed in section 4.2. More insight was subsequently gained using Kerr microscopy, providing a clear picture of the magnetic switching process as given in section 4.3. These measurements gave a spectacular view of the electric field effect on domain wall motion, previously unreported in the literature, as presented in section 4.4. The electric field is unambiguously identified as the cause of the observed effects in section 4.5. The effect of annealing is explored in section 4.6. Finally, first efforts were made to increase the magnitude of the electric field effect through device optimisation, the results of which are discussed in section 4.7.

Part of the work presented in this chapter has been accepted for publication in Nature Communications.

4.1 PMA in Pt/Co/Oxide samples

The initial aim of this project was to demonstrate electric field effects in thin magnetic films for the first time in the Physics of Nanostructures group. This required the fabrication of junctions displaying both perpendicular magnetic

anisotropy and a highly resistive dielectric barrier, as described in section 3.1. A variety of materials can be used to achieve such properties in a thin film stack. Initial efforts focussed on Pt/Co/AlOx, which has been shown [28, 29] to exhibit strong PMA and high domain wall velocities, making it interesting to technological applications. A dielectric material with a higher dielectric constant, TaOx, was also investigated. Experiments were also performed replacing pure Co with boron-doped Co ($Co_{68}B_{32}$) in an attempt to reduce the PMA, allowing for devices to function at smaller applied magnetic fields.

To determine the exact compositions exhibiting PMA, wedge samples were fabricated using various materials for both the magnetic and the dielectric layer, under variation of layer thicknesses and annealing temperature. This section describes the magnetic behaviour as a function of these parameters for the mentioned magnetic and dielectric layers, as probed by MOKE measurements.

4.1.1 Dielectric layer

A first step in creating perpendicular materials using an oxide layer is to establish an oxidation procedure. The choice was made to use a fixed oxidation time and intensity (10 minutes at 15 mA) and to adjust the dielectric layer thickness accordingly. To determine the optimal dielectric layer thickness, wedge samples were produced and analysed using polar MOKE measurements. In these experiments a 1 nm thick layer of cobalt is used as the magnetic layer, deposited on top of a 4 nm thick layer of platinum. The dielectric layer thickness is varied from 0 to 3 nanometres. Initial experiments used AlOx as a dielectric material, for reasons mentioned earlier. This material can be replaced by TaOx, which has a higher dielectric constant (roughly 30 for Ta_2O_5 [64] against 7 for Al_2O_3 [65]) and should thus produce higher electron concentrations at the same applied voltage. Results for both dielectrics are discussed below.

Aluminium

The magnetic characteristics under variation of the aluminium oxide (Al_2O_3) top layer thickness are presented in Fig. 4.1. Wedges are found to exhibit perpendicular magnetisation for a certain range of Al thicknesses. This is the result of the plasma oxidation process, as illustrated in Fig. 4.2. The sample does not display any magnetic properties below a top layer thickness of roughly 1.4

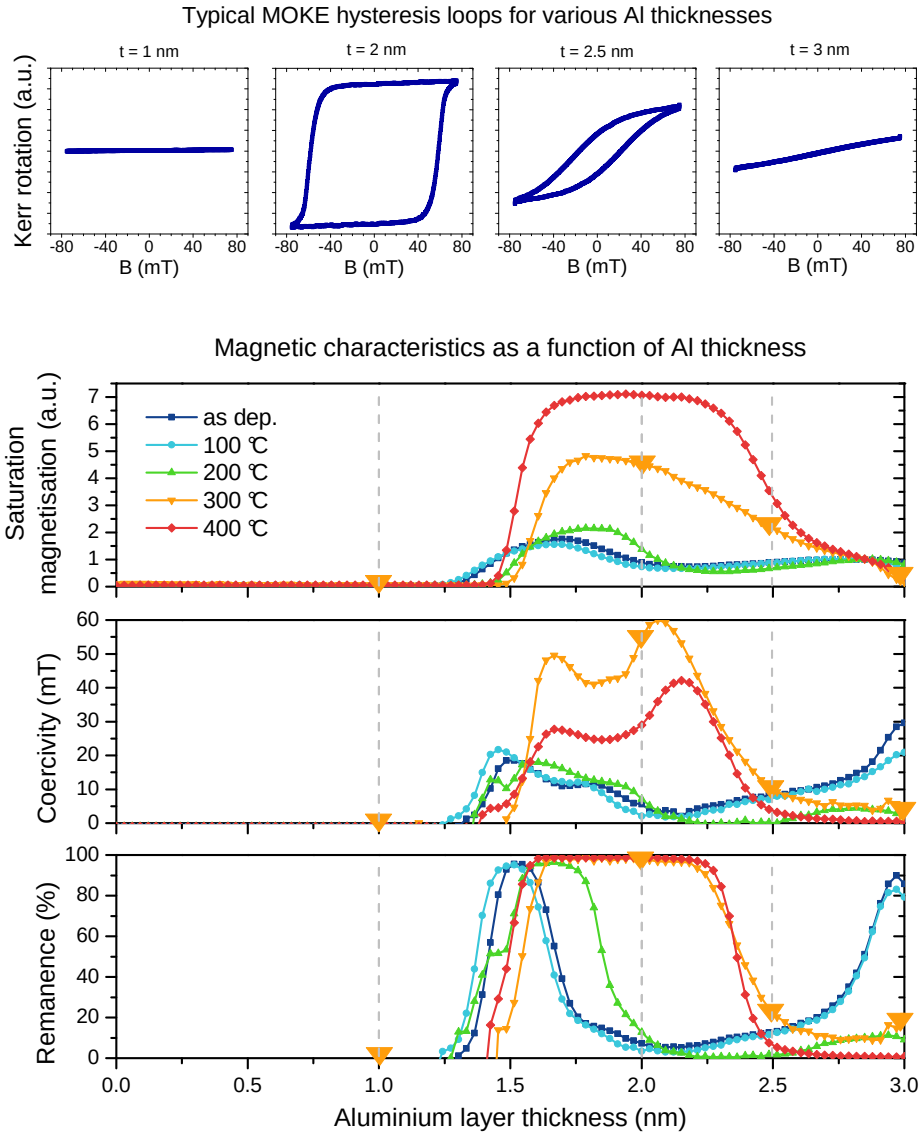

Figure 4.1: *Magnetic properties of oxidised Pt (4 nm) / Co (1 nm) / Al (0-3 nm) wedges annealed at various temperatures, obtained using polar MOKE measurements in an out-of-plane magnetic field. The top four panels show typical raw MOKE loops, in this case for the sample annealed at 300 °C, for four different Al thicknesses. Three key properties (saturation magnetisation, coercivity, and remanence, as described in section 2.3.1) are extracted from a series of such loops, and displayed as a function of Al layer thickness and annealing temperature in the three bottom panels. The dashed vertical lines indicate the position of the depicted raw MOKE loops. The large triangles emphasise the properties of the 300 °C trace at these points, which can be identified in the top panels.*

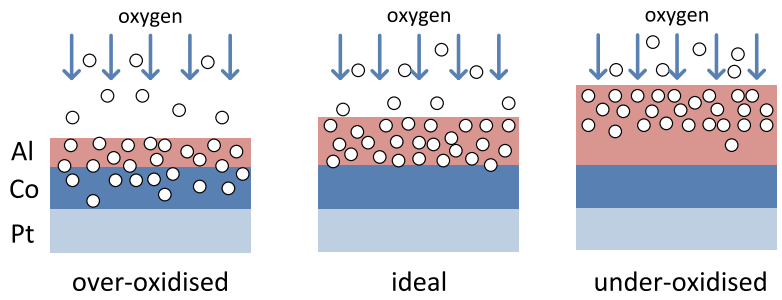

Figure 4.2: *Sketch of plasma oxidation in Pt / Co / Al for various Al layer thicknesses. If the Al layer is too thin, oxygen ions are implanted into the Co layer creating non-magnetic cobalt oxide. If the Al layer is too thick, oxygen ions cannot reach the critical Co/Al interface. Between these two extreme cases, a regime exists where a Co / AlOx interface is formed without destroying the Co layer.*

nm. The plasma oxidation process apparently destroys the magnetic layer: it is insufficiently shielded from the oxygen bombardment by the thin aluminium layer. Magnetic properties are not regained through annealing, indicating that oxygen does not migrate out of the cobalt layer even at high temperatures. After an initial peak at 1.5 nm, the out-of-plane anisotropy (reflected in the coercivity and remanence) decreases as a function of top layer thickness. This can be explained through excess shielding; the top layer captures many if not all of the oxygen atoms before they reach the Co/Al interface. The presence of oxygen atoms at this interface is known to be critical to the anisotropic bonding that causes PMA [66, 67, 68]. The interested reader is referred to the thesis by Knechten [69] for an extensive analysis of the plasma oxidation of Al. Both the coercivity and remanence are seen to improve by annealing at high temperatures, indicating a migration of oxygen atoms towards the interface. An annealing temperature of 300 °C is found to result in the best magnetic properties; higher temperatures are found to reduce the coercivity.

Perpendicular magnetic anisotropy is also observed for a very thick top layer, above 2.7 nm. This anisotropy is completely destroyed by annealing at temperatures above 200 °C. Apparently, a stack of Pt/Co/Al can also display PMA, possibly induced by the Pt/Co interface. This behaviour was not investigated further; an unoxidised metallic layer would shield electric field effects and is thus not of interest to this project.

The most important conclusion to draw from this measurement is that we

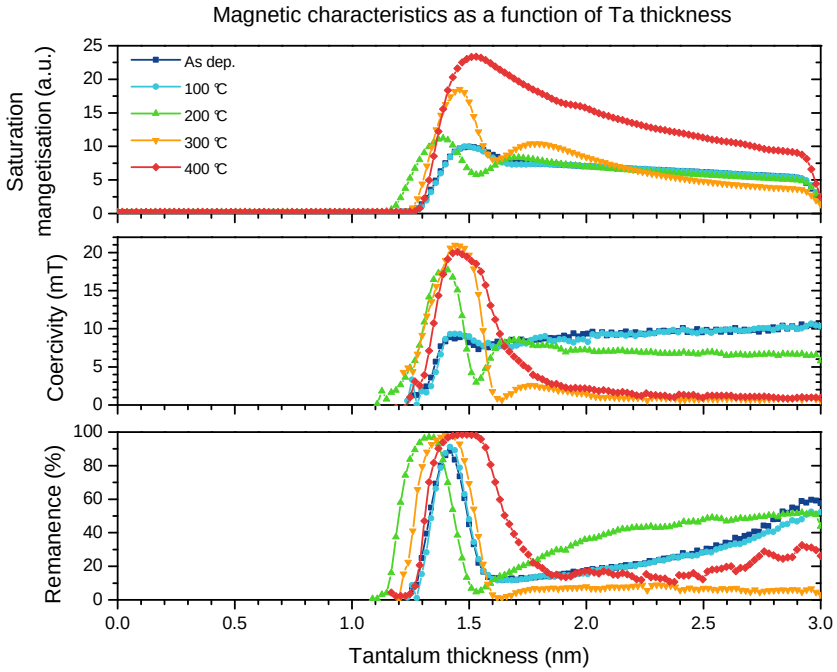

Figure 4.3: *Key magnetic properties of oxidised Pt (4 nm) / Co (1 nm) / Ta (0-3 nm) wedges annealed at different temperatures, extracted from polar MOKE measurements.*

can successfully create Pt/Co/AlOx samples displaying perpendicular magnetic anisotropy. Optimal magnetic properties are found for an Al layer thickness of 1.5 nm or more, and an annealing temperature of 300 °C. Note that 1.5 nm is the thickness of the Al layer after deposition; the layer will be thicker after oxidation. When fabricating resistive barriers, the thickness should be kept as close to 1.5 nm as possible to maximise the oxygen content and thus the resistivity of the barrier.

Tantalum

As mentioned before, replacing AlOx with TaOx (Ta_2O_5) should increase electric field effects at a certain voltage because of the increased dielectric constant. Measurements were performed on a Pt(4 nm)/Co(1 nm)/TaOx(0-3 nm) wedge to establish the optimal Ta thickness. The result of this experiment, presented in Fig. 4.3, is similar to that obtained for Al. The onset of PMA is found to be 1.4 nm for Ta, compared to 1.5 nm for Al. The highest coercivity in Pt/Co/TaOx

is found to be 10 mT (20 mT after annealing at 300 °C) which is roughly two times smaller than in Pt/Co/AlOx. The anisotropic bonding at the interface is thus found to depend on the dielectric material. The annealing process is still seen to improve magnetic properties in the perpendicular thickness regime. However, the width of this regime is hardly affected, whereas in Pt/Co/AlOx it could be extended significantly.

In conclusion, we have successfully fabricated Pt/Co/TaOx samples displaying perpendicular magnetic anisotropy. Using Ta rather than Al is found to reduce the coercivity, which can be useful in experiments. A complication is that the thickness of the Ta layer must be controlled within narrow bounds to sustain PMA.

4.1.2 Magnetic layer

The magnetic behaviour of the stack has been examined under variation of the magnetic material, layer thickness and annealing temperature. In these experiments a 1.4 nm thick oxidised layer of Ta is used as a top layer, based on the results presented in the previous section. Similar experiments using an Al top layer yielded inconsistent results, but are included in Appendix C for the sake of completeness.

The magnetic characteristics of a Pt(4 nm)/Co(0-2 nm)/TaOx (1.4 nm) wedge are depicted in Fig. 4.4. An out-of-plane magnetisation is found for a Co film thickness ranging roughly from 1.2 - 1.8 nm. By annealing at 300 °C, this range can be extended to 1.1 - 2.0 nm. Beyond this range, the sample remains magnetic but the easy axis turns in-plane. Interestingly, this seems to conflict with the wedge sample discussed in the previous section, where 1.0 nm of Co was found to display PMA using a Ta top layer thickness of 1.4 nm. This inconsistency could be caused by a small tooling factor introduced by the masking technique, as discussed in section 3.1.2.

The absence of any magnetic signal below a Co layer thickness of 1 nm is interesting. Extrapolation of the slope seen in the saturation magnetisation curve suggests that a substantial portion of the Co (roughly 0.7/0.5 nm for the as-deposited/annealed sample) is not magnetic at all.[1] A possible explanation for

[1]The same behaviour is seen when using an AlOx top layer (see Appendix C). Later experiments using a gentler oxidation procedure (3 minutes, 7.5 mA) on an otherwise identical wedge sample show PMA at a Co thickness as low as 0.3 nm. This finding supports the idea that lengthy high-powered oxidation creates a substantial cobalt oxide layer.

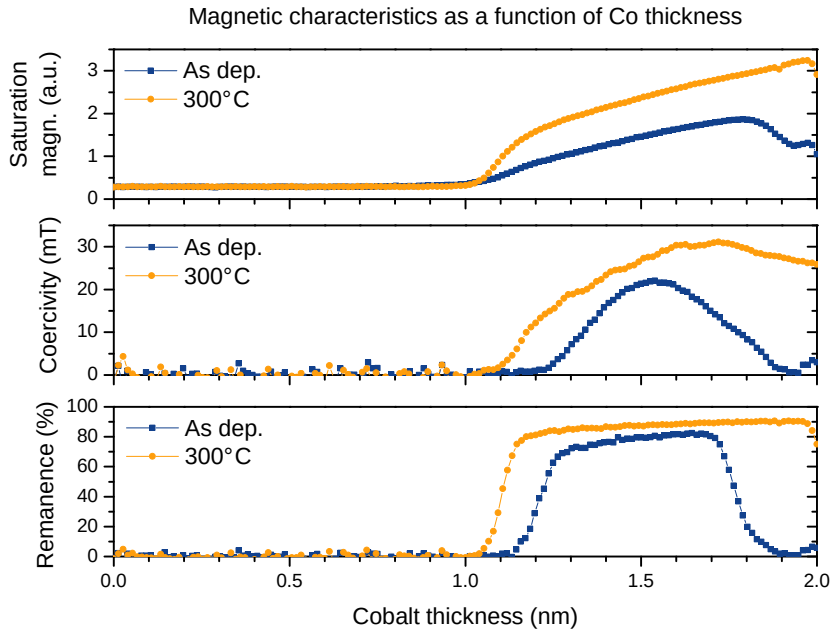

Figure 4.4: *Saturation magnetisation, coercive field, and remanence in an oxidised Pt (4 nm) / Co (0-2 nm) / Ta (1.4 nm) wedge.*

this is that oxygen atoms penetrate the Ta layer during the oxidation process, creating (non-magnetic) cobalt oxide up to a certain depth. This is not necessarily problematic in the experiments performed in this project; an over-oxidised sample can still display PMA and a high electrical resistivity.

The magnetic material itself was then changed, replacing pure cobalt with boron-doped cobalt ($Co_{68}B_{32}$) while maintaining a 1.4 nm thick TaOx top layer. The magnetic properties of a Pt(4 nm)/$Co_{68}B_{32}$(0-2 nm)/TaOx (1.4 nm) wedge are shown in Fig. 4.5. Comparison between the Co and $Co_{68}B_{32}$ magnetic layers (Fig. 4.4 vs Fig. 4.5) shows two main differences. The $Co_{68}B_{32}$ layer is seen to exhibit PMA over a different thickness range; roughly 0.7 - 1.2 nm for the as-deposited sample versus 1.2 - 1.8 nm found for a pure Co layer. The coercivity is also reduced significantly, providing an important experimental tool.

An important conclusion that can be drawn from this measurement is that experiments involving comparison between various magnetic materials are inherently difficult. Exchanging one material for the other affects the optimal thickness, so

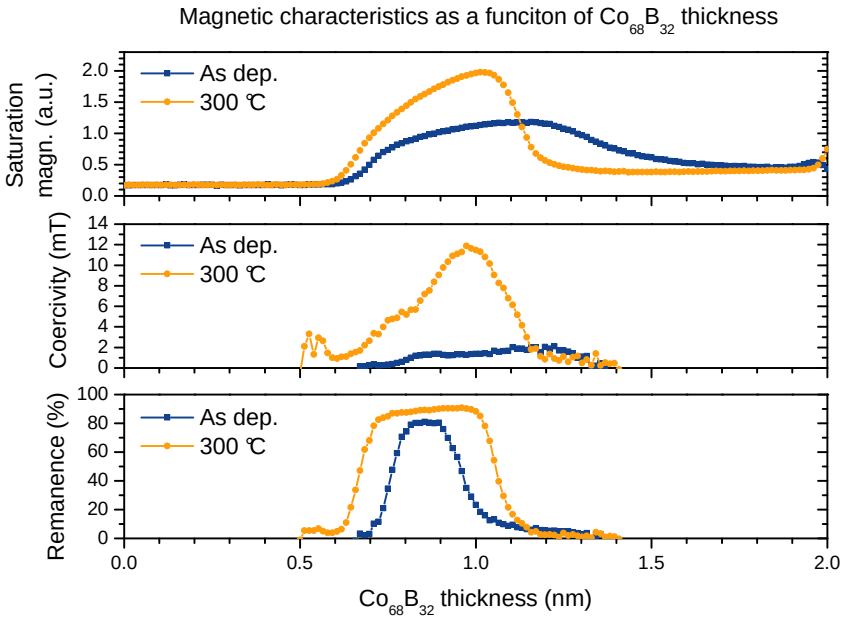

Figure 4.5: *Saturation magnetisation, coercive field, and remanence in an oxidised Pt (4 nm) / $Co_{68}B_{32}$ (0-2 nm) / Ta (1.4 nm) wedge.*

that a comparative study should be carried out over a range of layer thicknesses to produce meaningful results.

4.1.3 Conclusions

The most important conclusions drawn from this material research section are now summarised. Perpendicular magnetic anisotropy was observed in Pt/Co/AlOx, with optimal magnetic properties at an Al layer thickness of 1.5 nm and an annealing temperature of 300 °C. Making the Al layer thinner results in an oxidised magnetic layer, whereas a very thick Al layer prevents oxygen from reaching the magnetic interface, reducing the PMA. The aluminium can be replaced by tantalum, which has a larger dielectric constant. This substitution is found to reduce the coercivity, which can be useful in experiments. A complication is that the thickness of the Ta layer must be controlled within narrow bounds to sustain PMA.

The magnetic layer thickness is also important; an out-of-plane magnetisation is found for a Co film thickness ranging roughly from 1.2 - 1.8 nm. By annealing

at 300 °C, this range can be extended to 1.1 - 2.0 nm. Beyond this range, the sample remains magnetic but the easy axis turns in-plane. Data suggests that a substantial portion of the magnetic layer is oxidised during the plasma oxidation step, but this appears not to interfere with experiments. The coercivity of samples can be further reduced by replacing pure cobalt with boron-doped cobalt.

Exchanging one material for another affects the optimal thickness, so that a comparative study should be carried out over a range of layer thicknesses to produce meaningful results.

4.2 Demonstration of electric field effects using MOKE

After establishing stack compositions exhibiting a sizeable perpendicular magnetisation, junctions were fabricated to investigate electric field effects in such materials. The current-voltage characteristic of such a junction, presented in section 4.2.1, shows that the dielectric layer functions well as a highly resistive barrier. The magnetic switching process was probed by MOKE measurements, providing clear evidence for a voltage-induced effect as presented in section 4.2.2.

4.2.1 Junction current-voltage characteristic

Based on the performed material research, junctions exhibiting PMA were successfully produced using a Pt(4 nm)/Co(1 nm)/Al_2O_3(3.8 nm)/Pt (4 nm) stack. Note that the dielectric layer consists of 3 nm thick aluminium prior to oxidation. Upon oxidation, Al_2O_3 is expected to form from this pure Al. By comparing densities, the layer thickness is estimated to increase to 3.8 nm during the oxidation process. The current-voltage characteristic of such a junction, depicted in Fig. 4.6, clearly shows non-Ohmic behaviour. The junction resistance typically ranges from 100 kΩ to 1 MΩ for voltages between 0 V and 3 V, which is orders of magnitude higher than the contact resistance. Charges are thus expected to accumulate on either side of the dielectric barrier, with some losses occurring due to tunnelling or thermal activation.

4.2.2 Voltage-induced coercivity modification

The magnetic behaviour of a junction was explored by recording hysteresis curves under application of a varying out-of-plane magnetic field. The minimum field

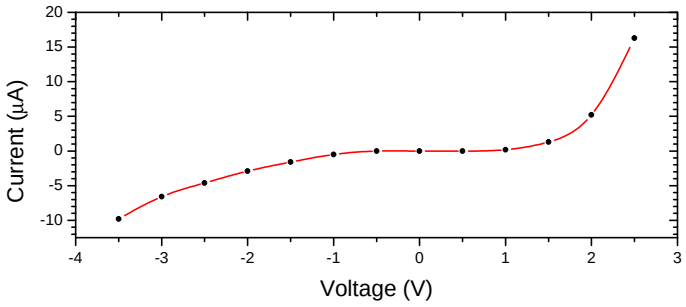

Figure 4.6: *Current as a function of voltage in a Pt(4 nm)/Co(1 nm)/Al_2O_3(3.8 nm)/Pt(4 nm) junction annealed at 300 °C. A positive voltage corresponds to a positive bias voltage on the bottom (magnetic) electrode. The resistance of the device is found to be non-Ohmic and asymmetric with respect to the applied voltage. It typically ranges from* 100 kΩ *to* 1 MΩ *for voltages between 0 V and 3 V.*

required to switch the magnetisation of the sample, referred to as the coercive field, is expected to depend on the magnetic anisotropy as shown in section 2.3.1. A voltage-induced modification of the anisotropy should thus be detectable as a change in coercivity with applied voltage.

Magnetic hysteresis curves as obtained through MOKE measurement under application of a voltage are presented in Fig. 4.7. The fabricated junction is seen to display strong perpendicular magnetic anisotropy: it displays a large remanence (near 100%) and a strong coercive field of roughly 85 mT. More importantly, clear evidence for an electric field effect on the magnetic properties of the sample is found. The application of a positive voltage is seen to reduce the coercivity, whereas a negative voltage increases the coercivity. We have thus demonstrated the modification of magnetic properties using an electric field; an important first step in our experimental efforts.

More quantitative information is acquired by plotting the relative change in coercivity as a function of the applied voltage, as in Fig. 4.8. The relative voltage-induced coercivity modification is found to be linear at a slope of $-0.76 \pm 0.02\,\%\mathrm{V}^{-1}$, which is quite small compared to values reported for other systems in the literature [20].

Two important questions may be raised at this point. First of all, can we confirm that the observed effect is a direct result of the applied electric field? The leakage current (see Fig. 4.6) might for instance induce thermal or magnetic

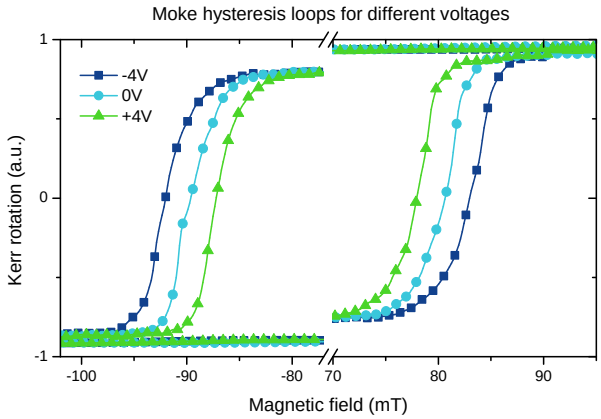

Figure 4.7: *Magnetic hysteresis curves for different applied voltages in a Pt(4 nm)/Co(1 nm)/Al_2O_3(3.8 nm)/Pt(4 nm) junction annealed at 300 °C, obtained through polar MOKE measurement using an out-of-plane magnetic field. A positive (negative) applied voltage is seen to decrease (increase) the coercivity.*

effects. The magnitude of this current, roughly 10 μA, is a first indication that such effects are not relevant. Furthermore, the sharp (non-Ohmic) increase in the current for higher voltages is not reflected in the coercivity modification (compare Fig. 4.6 and Fig. 4.8). More concise evidence that the observed effect is not current-related is presented in section 4.5.

The second question is whether the observed coercivity modification is a good measure for the underlying anisotropy modification. This distinction is generally not made in the literature, where the coercivity modification is often used as a quantification of the electric field effect [16, 20]. A well-defined relation between the coercive field and the anisotropy indeed exists in the Stoner-Wohlfarth model (see section 2.3.1), but this is essentially only valid for single-domain ferromagnets. As explained in section 2.3, magnetisation reversal in thin films can be a complex process involving domain nucleation and propagation, limiting the applicability of the concept of coercivity. Kerr microscopy has been employed to investigate the magnetisation reversal process in our samples, as described in the next section. This allows for a more quantitative picture of the electric field effect; a step forward from the initial observation presented in this section.

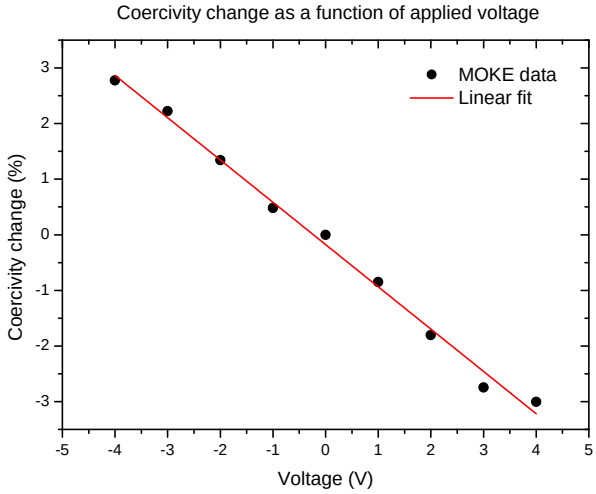

Figure 4.8: *Relative change in coercive field as a function of applied voltage. A linear fit through the data points yields a slope of* $-0.76 \pm 0.02\,\%\mathrm{V}^{-1}$.

4.3 Magnetic switching explored using Kerr microscopy

The MOKE measurements presented in section 4.2 provide clear evidence for a voltage-induced modification of magnetic properties. To obtain a more complete and quantitative picture of this electric field effect, the magnetisation reversal process was studied. Kerr microscopy (described in section 3.2) was employed to obtain a time-resolved broad overview of the magnetic switching in Pt(4 nm)/Co(1 nm)/Al_2O_3(3.8 nm)/Pt(4 nm) junctions annealed at 300 °C. A typical image as obtained during magnetisation reversal is presented in Fig. 4.9, and will be briefly discussed here to familiarise the reader with the various visible features.

The magnetisation of the sample is first saturated in the downward direction using a large negative magnetic field, after which the field is reduced to 0 mT. To enhance the magnetic contrast, recorded images show the differential signal intensity with respect to the 0 mT measurement. Magnetically switched areas show up as dark regions in the recorded image. The top Pt electrode is not magnetic, but shows up as a slightly lighter area due to its increased reflectivity. The magnetic wire is seen to be affected by the top electrode, possibly due to altered response to the annealing process. Most importantly, well-defined domain walls are clearly visible throughout the magnetic wire.

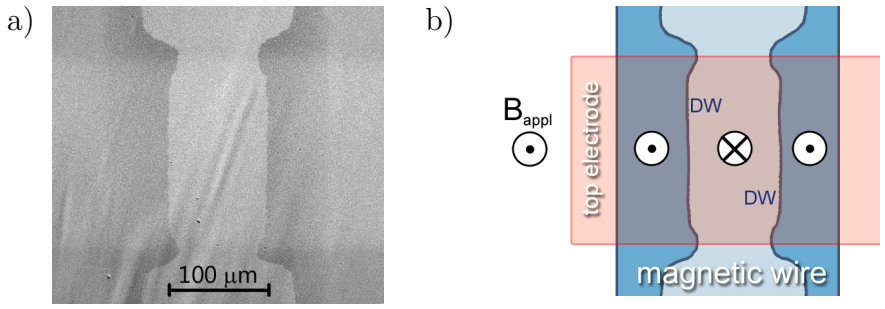

Figure 4.9: *a) Typical Kerr microscopy image of a junction during magnetisation reversal induced by an out-of-plane magnetic field. Details regarding the measurement procedure are given in the main text. b) Explanation of the different features visible in the Kerr microscopy image. The magnetic bottom electrode is seen as a broad vertical bar, showing regions of different magnetic orientation in different shades of grey. The outer domains have switched, and point in the (upward) direction of the applied magnetic field. The domain walls (DWs) separating these regions are well-defined and clearly visible. The top electrode is slightly visible as a broad horizontal bar of increased brightness.*

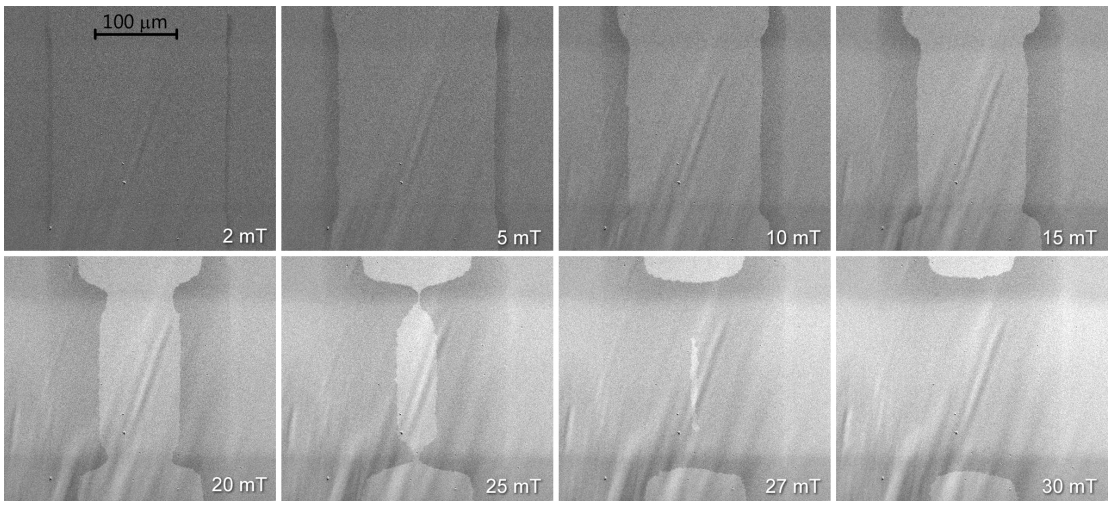

Figure 4.10: *Kerr microscopy images of magnetisation reversal in a junction achieved by sweeping the out-of-plane magnetic field. Magnetically reversed domains are seen to nucleate at the edges of the magnetic strip at small magnetic field, subsequently moving towards the centre of the junction. The general increase in brightness with increasing magnetic field (even for non-magnetic regions) is caused by Faraday rotation.*

The magnetisation in the junction is now saturated in the downward direction using a large magnetic field. The magnetic field is subsequently increased from 0 mT to 30 mT in the opposite direction. Several points in the recorded magnetisation reversal are depicted in Fig. 4.10, providing a detailed view of the switching process. A magnetically reversed domain is seen to nucleate at both edges of the magnetic strip at an applied field as small as 2 mT. These domains subsequently move towards the centre of the junction, accelerated by the increasing magnetic field. Magnetisation reversal in these samples is thus clearly the result of domain wall motion, rather than uniform reversal of the magnetisation or domain nucleation across the junction.

As shown in the literature, domain wall propagation at low velocities in Pt/Co/AlOx occurs through domain wall creep [28]. In the creep regime, domain walls can propagate in a constant magnetic field due to thermal activation. Complete reversal of the magnetisation, achieved at 30 mT in Fig. 4.10, can thus be reached at lower magnetic fields simply by allowing the domain walls more time to propagate. This phenomenon skews field-sweep results as presented in section 4.2 and in the literature. The expected effect on MOKE hysteresis loops is explored in Appendix D using a simple simulation. A more appropriate experiment is to record domain wall propagation at a fixed magnetic field, separating the time and field dependencies of the switching process.

A final interesting question regarding the observed switching process is *why* such straight domain walls are injected from the edges of the magnetic strip. The most likely explanation for this is related to the used deposition technique. Sputtering through a narrow slit mask is known to cause an inhomogeneous deposition profile, with significantly less material being deposited near the edges of thin wires [63], as illustrated in Fig. 3.4. The magnetic layer is thus expected to be thinner near the outer edges of the magnetic strip, allowing for magnetisation reversal using a relatively small coercive field.

4.4 Domain wall velocity modification by electric field

As demonstrated in section 4.3, magnetisation reversal in a typical junction sample occurs through propagation of domain walls from the edges of the magnetic material towards the centre. This feature is now used to study the effect of an applied electric field on domain wall motion. The magnetisation reversal process in a

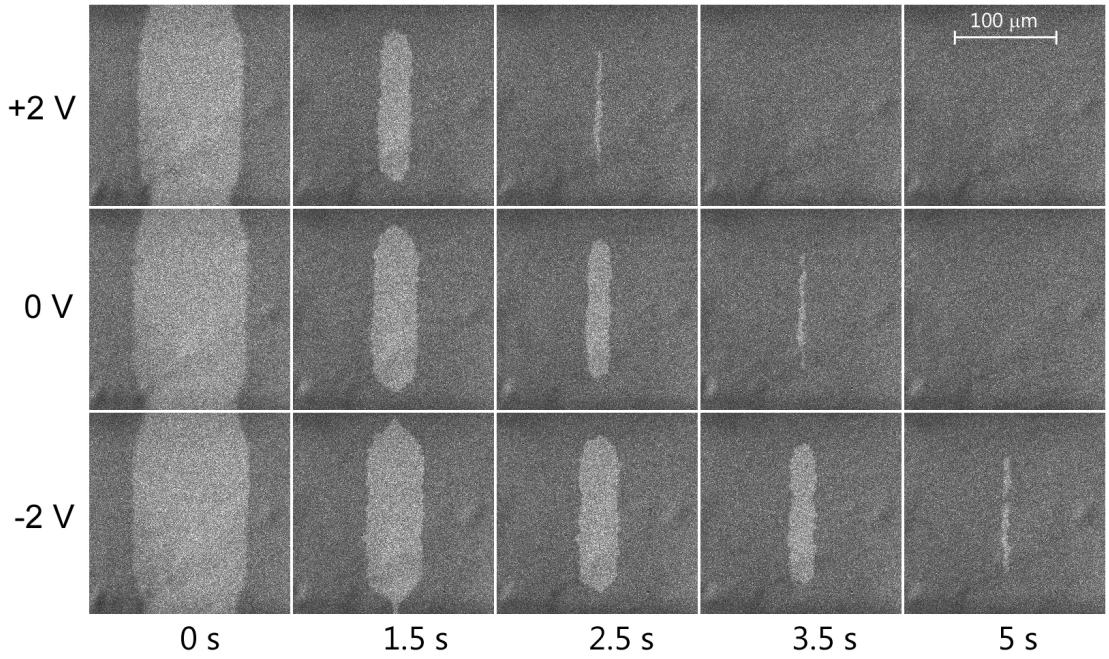

Figure 4.11: *Domain wall motion in a Pt(4 nm)/Co(1 nm)/Al_2O_3(3.8 nm)/Pt(4 nm) junction (annealed at 300 °C) under different bias voltages. The perpendicular magnetisation is saturated using a strong out-of-plane magnetic field prior to the measurement. A magnetic field of 23 mT in the opposite direction is suddenly applied at $t = 0$. A positive (negative) applied voltage is seen to significantly increase (decrease) the domain wall velocity. Note that the sign of the voltage is defined such that a positive bias voltage positively charges the magnetic electrode.*

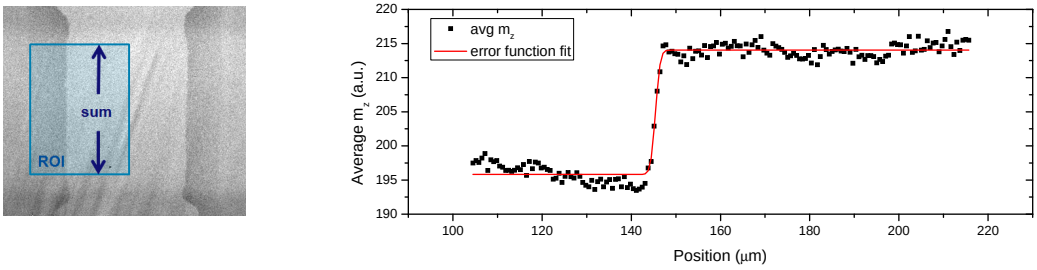

Figure 4.12: *Kerr image fitting procedure. a) A region of interest (ROI) is defined, spanning half the junction to include only one domain wall. Intensity data is summed along the indicated direction. b) Error function fit of the summed intensity data accurately indicates the domain wall position.*

steady magnetic field under application of different voltages is shown in Fig. 4.11. A positive (negative) applied voltage is seen to significantly increase (decrease) the domain wall velocity: complete switching requires 3.5 seconds at zero bias, 2.5 seconds at +2 V, and 5.0 seconds at -2 V. The domain wall velocity can thus be doubled by application of a few volts; a very significant effect, previously unreported in the literature. This effect is can be directly attributed to the electric field, as proved in section 4.5.

To quantify the domain wall velocity modification, Kerr microscopy videos (recorded at 16 frames per second) are analysed using MATLAB. The domain wall position is extracted from each video frame by fitting the intensity in a certain region of interest (ROI) with an error function, as illustrated in Fig. 4.12. The uncertainty in the resulting domain wall position data is estimated at ± 1 μm, based on the width of the error function.

Kerr microscopy videos of the magnetisation reversal process can thus be processed into quantitative data of domain wall position versus time. The domain wall velocity is obtained by taking the discrete derivative of this data. Such a discrete derivative requires significant displacement between adjacent data points, hence the raw data is divided into 5 μm wide bins. Typical plots of the obtained position and velocity data are shown in Fig. 4.13, extracted from the zero bias measurement shown in Fig. 4.11. The domain wall velocity is seen to decrease towards the centre of the junction, probably resulting from the deposition profile (see section 4.3).

The domain wall velocity across the junction can now be plotted for different

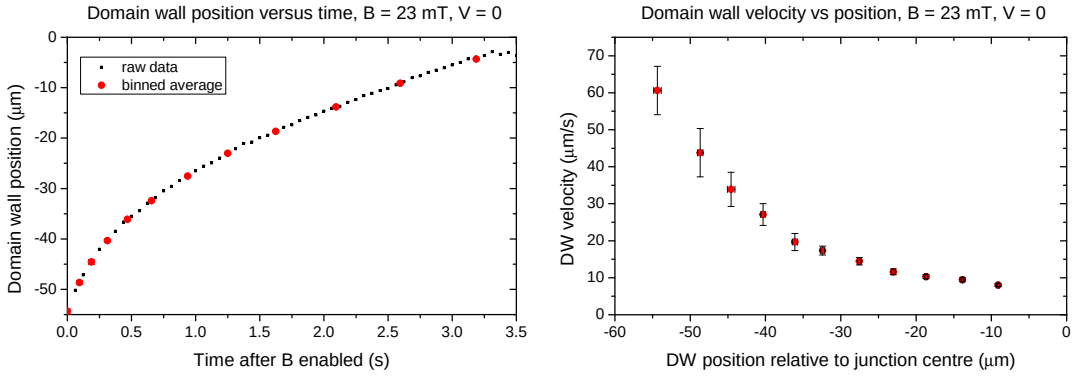

Figure 4.13: *Domain wall position versus time and domain wall velocity versus position as extracted from the zero bias measurement shown in Fig. 4.11. A binned average is computed from the raw position data to obtain a sizeable displacement between adjacent points. The domain wall position is defined relative to the junction centre.*

voltages, as shown in Fig. 4.14. This graph quantitatively confirms what was seen by eye in Fig. 4.11: a positive (negative) applied bias voltage significantly increases (decreases) the domain wall velocity. Application of 2 V (-2 V) is seen to increase (decrease) the domain wall velocity by as much as 40% (30%) across the entire junction.

The variation of the domain wall velocity across the junction is related to the deposition profile, and is not of interest here. A far more interesting quantity is the domain wall velocity at a certain point of the junction, measured as a function of the applied magnetic field and voltage. To establish this, curves like the ones shown in Fig. 4.14 were measured for a range of magnetic fields and voltages. A cross-section of this data at a certain position on the junction is shown in Fig. 4.15. The domain wall velocity is found to be a non-linear increasing function of both the magnetic field and the applied voltage.

We suppose now that domain wall transport at these low velocities is governed by creep dynamics. Careful analysis of the domain wall velocity v in this regime (see section 2.3.4) suggests that it depends on the applied magnetic field B and the voltage V as (see also Eq. 2.20):

$$v(B,V) = v_0 \exp\left[-C\left(1+\alpha V\right) B^{-1/4}\right] \tag{4.1}$$

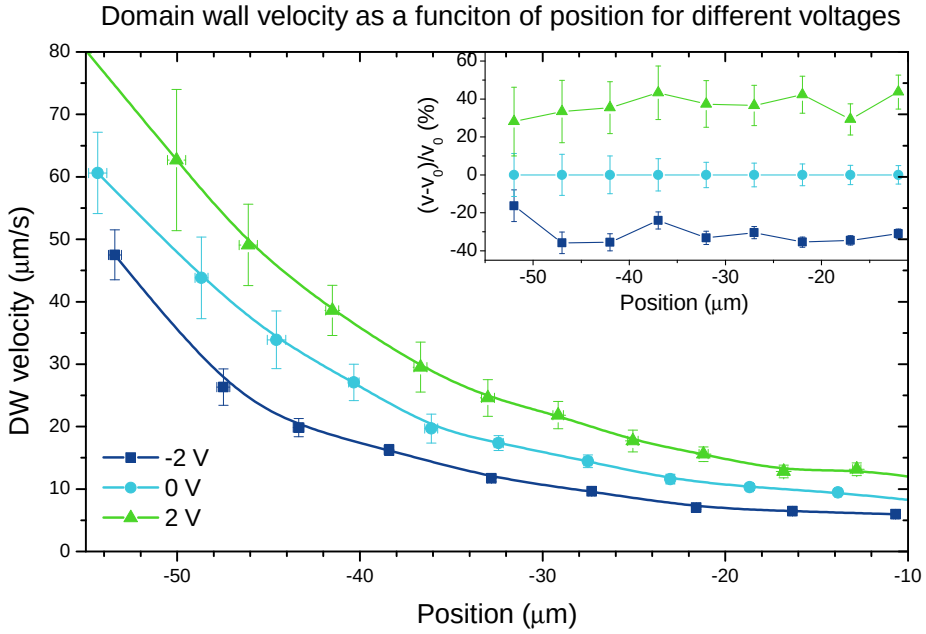

Figure 4.14: *Domain wall velocity across a typical junction, for different applied voltages, using an applied field of 23 mT. The position axis is defined relative to the junction centre. A positive (negative) bias voltage is seen to increase (decrease) the domain wall velocity across the sample. The inset shows the relative voltage-induced velocity modification, which is roughly uniform across the junction within the experimental error.*

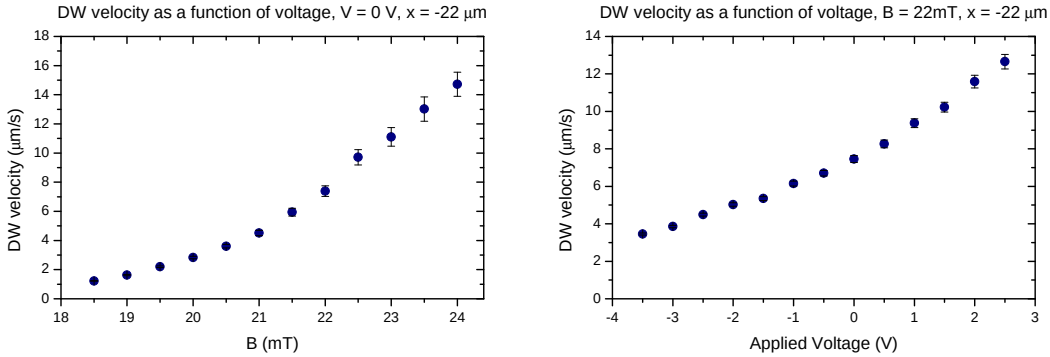

Figure 4.15: *a) Domain wall velocity as a function of applied magnetic field, without an applied bias voltage. b) Domain wall velocity as a function of bias voltage, using a magnetic field of 22 mT. Both graphs show the domain wall velocity at* $22\,\mu\mathrm{m}$ *from the junction centre; different positions yield similar curves.*

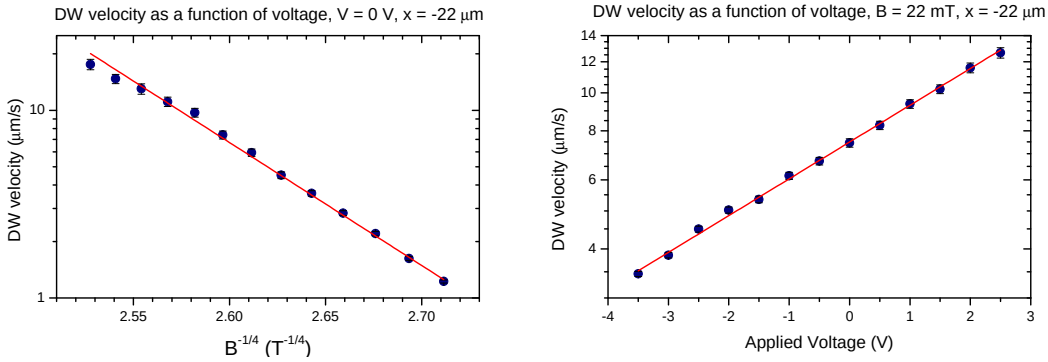

Figure 4.16: *a) Logarithm of domain wall velocity as a function of magnetic field, at zero bias voltage. b) Logarithm of domain wall velocity as a function of bias voltage, at a magnetic field of* 22 mT *or* 2.60 $\mathrm{T}^{-1/4}$. *The quality of the linear fits demonstrates the applicability of domain wall creep theory. The fitting procedure is described in the main text.*

with v_0 a scaling factor, C a general parameter and α a coefficient describing the linear scaling of the anisotropy with the applied voltage (see Eq. 2.19). If creep dynamics correctly describe the domain wall propagation in our experiments, the natural logarithm of v should thus depend linearly on V and $B^{-1/4}$. This hypothesis is tested in Fig. 4.16, and is found to be in good agreement with the measured data.

The experimental data can be fitted using a two-step fitting procedure. First, the magnetic field-dependent data at zero bias voltage is fitted using Eq. 4.1. At zero bias voltage α is eliminated, so that the slope and offset of $\ln(v)$ unambiguously yield C and v_0, respectively. With the parameter C established, the voltage-dependent data can then be fitted with Eq. 4.1 to give a value for α. This procedure yields, for the Pt(4 nm)/Co(1 nm)/Al_2O_3(3.8 nm)/Pt(4 nm) junction annealed at 300 °C discussed in this section, the value $\alpha = (-0.51 \pm 0.01)$ $\%\mathrm{V}^{-1}$. The other parameters are less relevant, but are included here for completeness: $C = (15.218 \pm 0.003)$ $\mathrm{T}^{1/4}$ and $v_0 = \exp[41.1 \pm 0.6]$ μm/s. Note that a single set of parameters can accurately describe both the voltage and magnetic field dependence, as demonstrated in Fig. 4.17. This graph also clearly shows that the velocity modification induced by a certain applied voltage does not depend on the applied magnetic field.

The magnetic anisotropy is thus determined to scale with the applied voltage

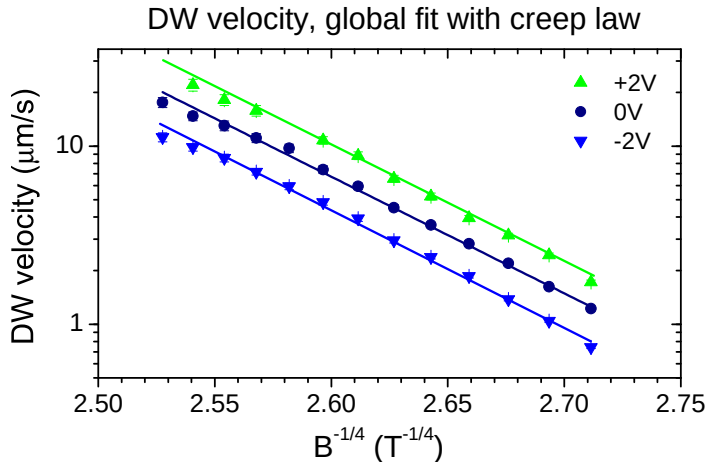

Figure 4.17: *Logarithm of domain wall velocity as a function of magnetic field in* $\mathrm{T}^{-1/4}$*, at three different bias voltages. A global fit with the creep law (Eq. 4.1) accurately describes the measured data using* $\alpha = (-0.51 \pm 0.01)\ \%\mathrm{V}^{-1}$*,* $C = (15.218 \pm 0.003)\ \mathrm{T}^{1/4}$*, and* $v_0 = \exp[41.1 \pm 0.6]$ m/s.

at $(-0.51 \pm 0.01)\ \%\mathrm{V}^{-1}$ for this particular sample. In order to compare this to literature values, it is convenient to convert the voltage to an electric field by dividing by the dielectric layer thickness. The anisotropy modification is thus estimated at $-1.9\ \%\mathrm{V}^{-1}\mathrm{nm}$, which means that an electric field of 1 V/nm alters the magnetic anisotropy by roughly -2%.

A further generalisation can be made by estimating the absolute anisotropy modification, rather than the relative effect. To this end, hard-axis MOKE measurements were carried out to determine the magnetic anisotropy of the sample (see Appendix E for an example of this procedure), yielding a value of $0.7 \pm 0.1\ \mathrm{mJ/m^2}$. The absolute electric-field induced modification of the magnetic anisotropy is thus determined to be $-14 \pm 2\ \mathrm{fJV^{-1}m^{-1}}$ for this particular sample. The order of magnitude of this value agrees well with the literature; Shiota *et al.* for example reported a value of $31.0\ \mathrm{fJV^{-1}m^{-1}}$ for a Au/FeCo(0.60 nm)/MgO system [15].

4.5 Exclusion of current-induced effects

An important question to raise at this point is whether the observed effect is actually directly caused by the applied electric field. There are three obvious

alternative mechanisms that could affect the coercivity, all related to the leakage current: Joule heating, Oersted fields, and spin-transfer torque (STT). Each of these mechanisms can individually be excluded as the source of the observed electric field effects:

- **Joule heating** cannot account for the increase in coercivity seen at negative voltages, as thermal activation aids the magnetisation reversal and can only decrease the coercivity.

- **Oersted fields** created by the small leakage current are negligible in size, as can be shown by a quick calculation using Ampère's law. Assume a current of 10 μA, running through a 200 μm wide wire. The geometry can be described as an infinite thin plate carrying a surface current of 0.05 A/m. Such a current generates a uniform magnetic field along the film surface with a strength of roughly 10 nT; a thousand times smaller than the Earth's magnetic field.

- **Spin-torque transfer** caused by the small leakage current is equally negligible. For a current of 10 μA, the current density in the magnetic electrode (width 200 μm, height 5 nm) is $10 \cdot 10^6$ A/m^2; many orders of magnitude smaller than the $10 \cdot 10^{10}$ A/m^2 typically required for STT switching of magnetic layers [70].

A more general argument to exclude current-related effects involves break-down of the dielectric barrier. If a sufficiently large voltage is applied to a junction, a sudden irreversible decrease in the resistance is observed, indicating breakdown of the dielectric barrier (i.e. pinhole formation). Whereas the current increases significantly after breakdown, the voltage-induced modification of the domain wall velocity slightly decreases as shown in Fig. 4.18. This is clear evidence that the observed voltage-dependent effect is not caused by leakage current related phenomena.

Finally, all magnetic field-like effects can be excluded using a symmetry argument. Both an increase and a decrease in domain wall velocity are observed, for positive and negative applied voltage, respectively. An induced magnetic field must point in the out-of-plane direction, if it is to explain this antisymmetric voltage dependence. If the externally applied out-of-plane magnetic field is reversed, the sign of a magnetic field-like effect is thus required to change with respect to the

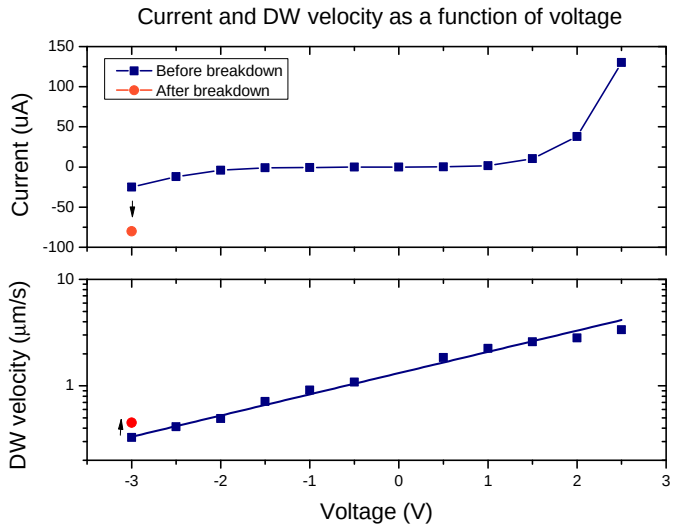

Figure 4.18: *Current and domain wall velocity (logarithmic) as a function of applied voltage. Data was recorded in increasing order of voltage magnitude. After breakdown of the dielectric barrier the current is seen to increase threefold, whereas the electric field effect on the domain wall velocity is reduced.*

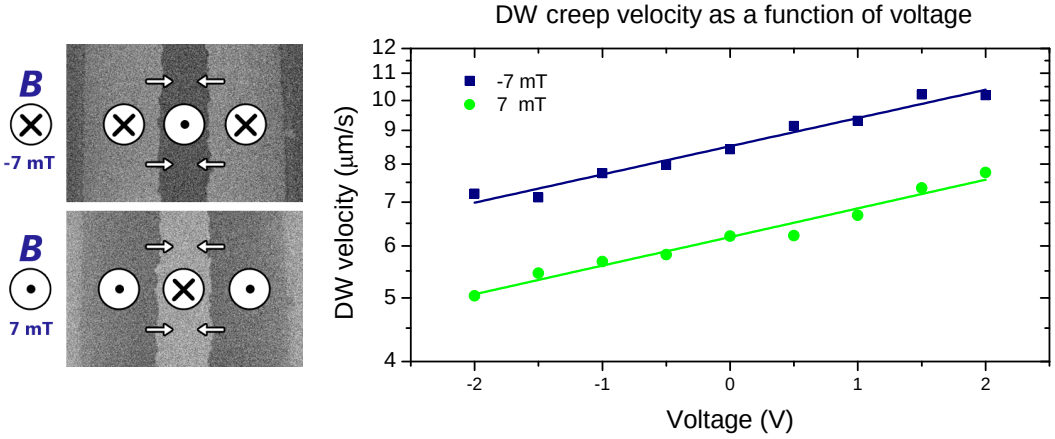

Figure 4.19: *Domain wall velocity as a function of voltage for two opposite directions of the applied magnetic field. The vertical offset is caused by inaccuracy in the magnetic field calibration. Fitting the data to the creep law (Eq. 4.1) yields a relative electric field effect of* $\alpha = (-0.33 \pm 0.02)\ \%\mathrm{V}^{-1}$ *for both measurements, demonstrating that the direction of the magnetic field does not affect the voltage-induced anisotropy modification.*

applied voltage. Such an experiment has been carried out in a Pt(4 nm)/Co(1 nm)/Al_2O_3(3.8 nm)/Pt(4 nm) junction, annealed at 300 °C for 30 minutes. The resulting voltage-induced effect on the domain wall velocity is shown in Fig. 4.19; no sign reversal is observed.

Concluding, based on the current magnitude and observed symmetries, heating and magnetic-field like effects can be excluded as the origin of the voltage-induced effect. The observed effects are therefore unambiguously attributed to the electric field.

4.6 The effect of annealing

The effect of annealing on magnetic properties was previously examined using MOKE measurements, as discussed in section 4.1. Annealing at 300 °C for 30 minutes was found to significantly increase the coercive field, remanence, and saturation magnetisation. This change is now studied in junctions, allowing for measurement of the dielectric barrier resistance and domain wall velocity before and after annealing. The result of this measurement is shown in Fig. 4.20.

Perhaps surprisingly, the annealing process is found to reduce the device resistance. A possible explanation is that annealing causes oxygen atoms to diffuse through the material. After plasma oxidation, most oxygen is expected to be present near the top of the dielectric layer. Annealing could cause the oxygen concentration to even out across the dielectric layer (and possibly the magnetic layer) through diffusion, reducing the series resistance of the stack.

In line with the observed increase in coercivity, annealing is found to significantly decrease the domain wall velocity. Referring to the discussion on domain wall creep (section 2.3.4) this drastic decrease can be explained by an increase in the anisotropy due to annealing, with $v(K) \propto \exp\left[-K^{9/8}\right]$.

Finally, the voltage-induced domain wall velocity modification before and after annealing is compared in Fig. 4.21. The annealing process is found to increase the relative anisotropy modification: $\alpha = (-0.82 \pm 0.05)\ \%\mathrm{V}^{-1}$ for the as-deposited sample and $\alpha = (-1.44 \pm 0.05)\ \%\mathrm{V}^{-1}$ for the annealed sample. As the absolute anisotropy was also found to increase through annealing, the absolute voltage-induced anisotropy modification is apparently enhanced by annealing. Many factors could contribute to this change; some examples include reduced interface roughness and changed oxygen concentration at the magnetic / dielectric interface.

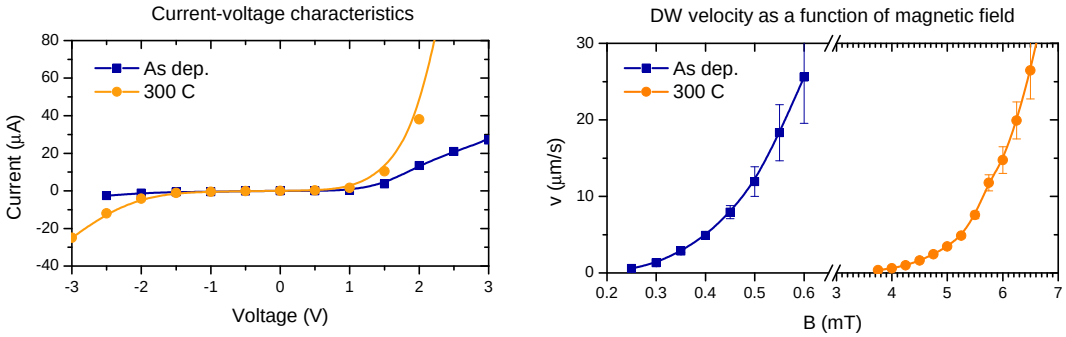

Figure 4.20: *Comparison between two Pt(4 nm)$C_{68}B_{32}$(1 nm)/Ta_2O_5(7 nm)/Pt(4 nm) junctions grown simultaneously, one of them annealed at 300 °C for 30 minutes. a) Current-voltage characteristics, demonstrating that the annealing process decreases the junction resistance significantly. Breakdown occurred at -3 V in both the as deposited and annealed junction. b) Domain wall velocities as a function of magnetic field, showing that the annealing process increases the driving field required to achieve a certain domain wall velocity. Notice the different scales on either side of the horizontal break.*

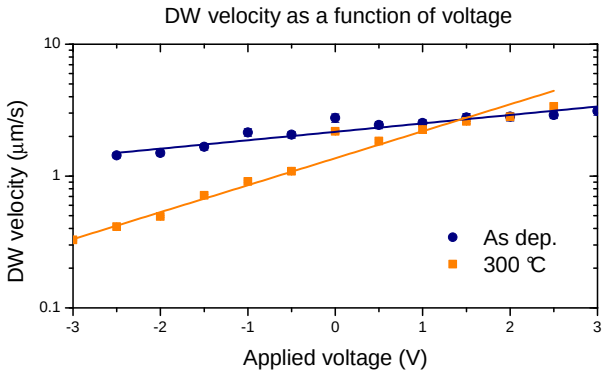

Figure 4.21: *Domain wall velocity as a function of voltage for two Pt(4 nm)/$C_{68}B_{32}$(1 nm)/Ta_2O_5(7 nm)/Pt(4 nm) junctions grown simultaneously, one of them annealed at 300 °C for 30 minutes. Measurements are performed at 0.6 mT for the as-deposited sample and 5.0 mT for the annealed sample. The annealing process is found to increase the relative anisotropy modification: fitting yields $\alpha = (-0.82 \pm 0.05)\ \%\mathrm{V}^{-1}$ for the as-deposited sample and $\alpha = (-1.44 \pm 0.05)\ \%\mathrm{V}^{-1}$ for the annealed sample.*

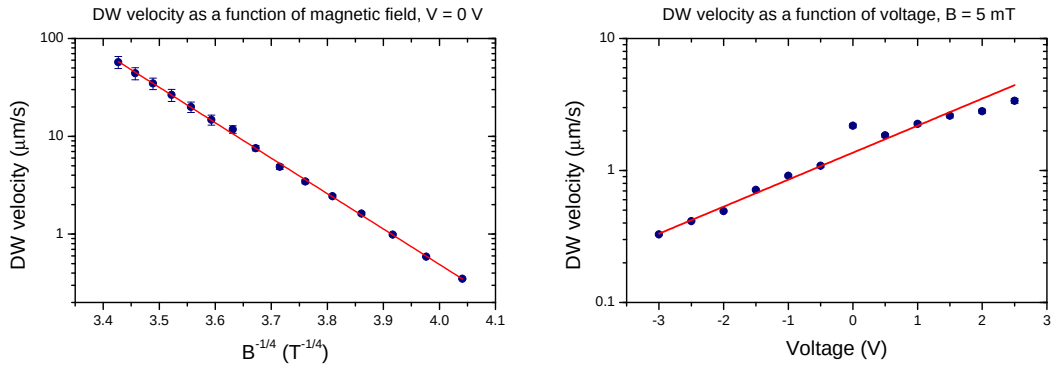

Figure 4.22: *Domain wall velocity in a Pt(4 nm)/$C_{68}B_{32}$(1 nm)/Ta_2O_5(7 nm)/Pt (4 nm) junction, as a function of a) magnetic field in $T^{-1/4}$ and b) bias voltage. Fitting using the domain wall creep law (Eq. 4.1) yields $\alpha = (-1.44 \pm 0.05)$ $\%V^{-1}$.*

4.7 Increasing the magnitude of the electric field effect

As discussed in section 4.4, first results were obtained for a Pt(4 nm)/Co(1 nm)/Al_2O_3(3.8 nm)/Pt(4 nm) junction. Through domain wall velocity measurements, the relative anisotropy modification in this sample was determined to be (-0.51 ± 0.01) $\%V^{-1}$ or -1.9 $\%V^{-1}$nm. By estimating the absolute anisotropy from hard-axis MOKE measurements, the absolute value of this effect was estimated at -14 ± 2 $fJV^{-1}m^{-1}$. The current section describes the first efforts undertaken to increase the absolute and relative magnitude of this electric field effect.

First of all, the AlOx was replaced with TaOx, as discussed in section 4.1.1. This raises the dielectric constant of the barrier, from roughly 7 for Al_2O_3 [65] to 30 for Ta_2O_5 [64], yielding a higher electron concentration at the magnetic/dielectric interface at the same applied voltage. This should thus increase the anisotropy modification per applied volt. Furthermore, the pure cobalt was replaced with boron-doped cobalt ($Co_{68}B_{32}$) to reduce the perpendicular magnetic anisotropy. Domain wall velocity modification results for a Pt(4 nm)/$C_{68}B_{32}$(0.8 nm)/Ta_2O_5(7 nm)/Pt(4 nm) junction are depicted in Fig. 4.22. Fitting this data using the creep law yields $\alpha = (-1.44 \pm 0.05)$ $\%V^{-1}$, or a relative anisotropy modification of -10 $\%V^{-1}$nm. This is a fivefold increase with respect to the Co(1 nm)/AlOx sample. By estimating the anisotropy from hard-axis MOKE measurements, this value was determined to correspond to a magnitude of -28 ± 4 $fJV^{-1}m^{-1}$; twice

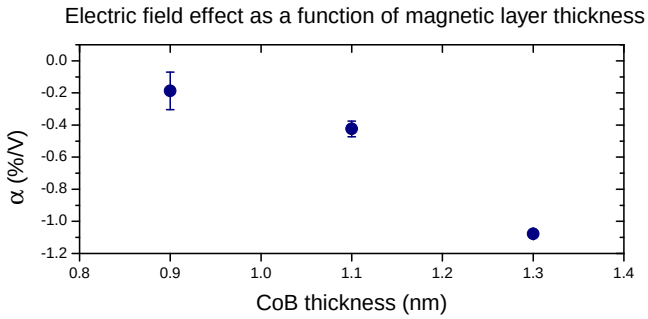

Figure 4.23: *Relative anisotropy modification per applied volt in three samples of varying magnetic layer thickness. The relative anisotropy modification α (see Eq. 4.1) is obtained by fitting magnetic field and voltage dependent domain wall velocity for each sample. The used samples consist of Pt(4 nm /$Co_{68}B_{32}$(x nm)/Ta_2O_5(7 nm)/Pt(4 nm), annealed at 300 °C for 30 minutes. The relative anisotropy modification is clearly seen to increase with increasing layer thickness.*

that found for Co(1 nm)/AlOx. Two effects expected from theory are confirmed by these findings: the electric field effect can be altered by choosing different materials, and the magnitude of the relative anisotropy modification can be increased by reducing the perpendicular magnetic anisotropy.

The magnitude of the electric field effect was also studied under variation of the magnetic layer thickness. This proved to be challenging using the available deposition technique, as each sample had to be grown in a separate run. Small fluctuations in the deposition process create thickness and quality variations between samples, making it difficult to compare ultrathin layers grown in different runs. Still, a small thickness series was successfully produced, as presented in Fig. 4.23. This small series still shows a clear trend: the relative anisotropy modification is increased with increasing magnetic layer thickness. [2] This is expected from Eq. 2.2: the magnitude of the perpendicular magnetic anisotropy is reduced for increasing layer thickness, so that the perpendicular anisotropy modification (an interfacial effect, not dependent on the layer thickness) is enhanced relatively.

Finally, it should be emphasised that the results obtained in this research

[2] It should be noted that the $Co_{68}B_{32}$ (1.0 nm) sample discussed earlier (see Fig. 4.22) does not fit into this thickness series at all. This sample was fabricated months earlier; changes in the deposition set-up (including relocation of the Ta target) are most likely the cause of this discrepancy.

project imply tremendous possibilities for voltage-controlled domain wall motion. The largest observed effect showed control of the domain wall velocity over an order of magnitude (Fig. 4.22) induced by an anisotropy modification of $-28 \pm 4\,\mathrm{fJV^{-1}m^{-1}}$. In the literature, anisotropy modification values are reported as large as $100\,\mathrm{fJV^{-1}m^{-1}}$ in Cu/Fe/MgO [71] and $196\,\mathrm{fJV^{-1}m^{-1}}$ in Pt/Fe/Pt/MgO [15]. Due to the exponential character of the creep law, an n-fold increase in the anisotropy modification implies an n-fold order of magnitude increase in the domain wall velocity modification. It is thus safe to say that voltage control of domain wall velocity over many orders of magnitude is feasible, creating exciting new possibilities for spintronics devices.

4.8 Summary

The presented experimental work is now briefly summarised. After a material research and optimisation process using wedge samples, junctions featuring both a perpendicularly magnetised thin film and a highly resistive dielectric barrier were successfully fabricated. Clear evidence of an electric field effect on the magnetic properties of such junctions was found using MOKE measurements. The coercive field could be decreased (increased) by application of a positive (negative) voltage. Heating and magnetic field-like effects were excluded as the origin of the observed effect, which was therefore attributed unambiguously to the electric field.

The magnetisation reversal process was subsequently investigated using Kerr microscopy. Switching was found to occur through domain wall creep motion. Application of a positive (negative) voltage was shown to increase (decrease) the domain wall velocity across the entire junction area. Voltage control over domain wall motion was thus demonstrated; a phenomenon previously unreported in the literature. This mechanism can account for the observed coercivity change in MOKE measurements, as confirmed through a simple simulation.

The obtained data could be fitted using relations derived from creep theory. The magnetic anisotropy was thus confirmed to vary linearly as a function of the applied voltage. In Pt/Co(1 nm)/Al_2O_3(3.8 nm)/Pt, an electric field of 1 V/nm was thus determined to change the magnetic anisotropy by -1.9 %. This was determined to correspond to an electric field induced anisotropy modification of $-14 \pm 2\,\mathrm{fJV^{-1}m^{-1}}$ by calculating the total anisotropy from hard-axis MOKE measurements.

First efforts were made to increase the magnitude of the observed electric field effect. Analysis of the domain wall velocity in a $Pt/Co_{68}B_{32}(0.8nm)/Ta_2O_5(7$ nm)/Pt junction yielded a relative anisotropy modification of $-10\,\%V^{-1}nm$, corresponding to a magnitude of $-28 \pm 4\,fJV^{-1}m^{-1}$. This modification allowed for the domain wall velocity to be varied over an order of magnitude by applying a few volts. Comparison to electric field effects reported in the literature suggests that voltage control of domain wall motion over many orders of magnitude is feasible, creating exciting new prospects for spintronics applications.

Chapter 5

Conclusions

Experiments and theoretical analysis were performed on the subject of electric field control of magnetic anisotropy in thin films. The phenomenon of interfacial magnetic anisotropy in thin films was related to the crystal bonding environment using a ligand field model. This ligand field model was extended to include a Fermi level shift, estimating the expected order of magnitude of a voltage-induced anisotropy modification. More advanced calculations in the literature were found to agree with the obtained result. This electric field effect was subsequently linked to a domain wall velocity modification using domain wall creep theory.

Before experiments could be carried out on such electric field effects, suitable samples had to be fabricated. Junctions featuring both a perpendicularly magnetised thin film and a highly resistive dielectric barrier were successfully produced using a Pt/Co/AlOx/Pt stack. The magnetic properties could be adjusted by varying the magnetic layer thickness and the annealing temperature.

Magnetic hysteresis curves were obtained through magneto-optic Kerr effect (MOKE) measurements under application of a voltage across the dielectric barrier. Clear evidence of an electric field effect on magnetic properties was found: a positive (negative) voltage was seen to reduce (increase) the coercivity. Based on the leakage current magnitude and symmetry arguments, heating and magnetic field-like effects were excluded as the origin of the observed effect, which was therefore attributed unambiguously to the electric field.

Kerr microscopy was employed to investigate the magnetic switching process. Magnetisation reversal in our samples was found to be dominated by domain wall motion, rather than uniform rotation of the magnetisation or domain nucleation across the junction. The observed velocities suggest that domain wall motion takes place in the creep regime, which is governed by thermal activation. Using a simple simulation, this was shown to have a profound effect on MOKE measurements.

Domain wall motion was subsequently studied under application of an electric field. Application of 2 V (-2 V) was seen to increase (decrease) the domain

wall velocity by as much as 40% (30%) across the entire junction area. Voltage control over domain wall motion was thus demonstrated; a phenomenon previously unreported in the literature.

The obtained data could be fitted using a relation between the domain wall velocity and the magnetic anisotropy derived from creep theory. The magnetic anisotropy varies linearly as a function of the applied voltage, at $-1.9\,\%$ per applied V/nm for a Pt/Co(1 nm)/Al_2O_3(3.8 nm)/Pt junction. This corresponds to an electric field induced anisotropy modification of $-14 \pm 2\,\mathrm{fJV^{-1}m^{-1}}$. This observed order of magnitude corresponds well with similar data reported in the literature.

First efforts were made to increase the magnitude of the observed electric field effect. Analysis of the domain wall velocity in a Pt/CoB(0.8nm)/Ta_2O_5(7 nm)/Pt junction yielded a relative anisotropy modification of $-10\,\%\mathrm{V^{-1}nm}$, corresponding to a magnitude of $-28 \pm 4\,\mathrm{fJV^{-1}m^{-1}}$. This anisotropy modification allowed for control of the domain wall velocity over an order of magnitude. In the literature, anisotropy modifications five or ten times as large are reported for different materials, implying that voltage control of domain wall motion should be possible over many orders of magnitude. This creates exciting new prospects for spintronics applications.

Chapter 6

Outlook

One can safely state that electric field effects in magnetic thin films have attracted significant scientific interest in a short amount of time. The reason for this is probably the technological applicability; the demonstrated effects promise new possibilities while being fully compatible with contemporary solid state technology.

In the immediate future, the FNA research group could perform several interesting experiments on electric field effects. In this project, first efforts were made to increase the magnitude of the electric field effect, but much room for improvement remains. Significantly larger modifications of the perpendicular magnetic anisotropy were reported in the literature. The electric field effect could be studied in many more magnetic materials and alloys, both experimentally and through ab-initio simulations. Furthermore, approaching the out-of-plane to in-plane anisotropy transition should significantly increase the observed (relative) anisotropy modification, which is interesting for device applications. Also, the unique experimental capabilities of the research group could be used to, for example, study ultra-fast magnetisation dynamics under application of an electric field.

On the long term, the combination of thin film magnetism with electric fields has tremendous potential for technological applications. First demonstrations of technological implementations of the electric field effect have already been reported. These include improvements to existing technologies such as hard-disk drives [23] and magnetic tunnel junctions [26]. Moreover, extremely power-efficient memory devices can be created by switching magnetic layers using pulsed electric fields, as recently demonstrated by Shiota *et al.* [10]. This promising achievement justifies extensive further research into the electric-field control of thin film magnetism.

The electric field effect can also be combined with other recent discoveries in spintronics, to allow for exciting and unique device concepts. An interesting idea that came about during this research project, for example, is based on the recently demonstrated [72] perpendicular switching of a single ferromagnetic layer

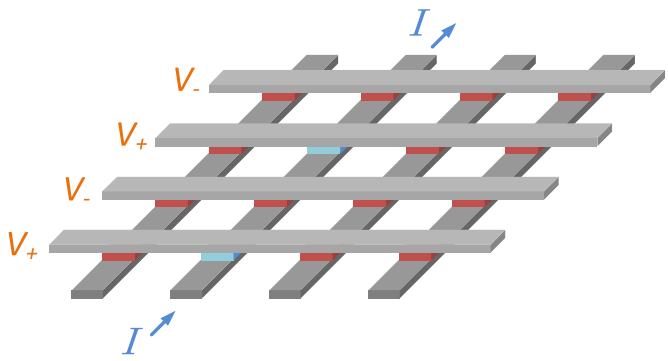

Figure 6.1: *MRAM concept using in-plane current injection to switch magnetic bits. Each junction is a TMR stack, with perpendicularly magnetised layers. A bias voltage supplied to the top leads is used to control which bits are switched: a positive (negative) bias voltage decreases (increases) the magnetic anisotropy to allow (prohibit) switching. All bits on a current line can be selectively switched simultaneously. Read-out is performed using the TMR effect.*

induced by in-plane current injection. Combining this switching mechanism with voltage-induced anisotropy modification creates a promising new MRAM, depicted in Fig. 6.1. Each junction is a perpendicularly magnetised tunnel junction; the magnetic state can be read using the TMR effect. Writing is performed using an in-plane current pulse, the magnitude of which is just below the threshold required for switching. Using the electric field effect, the anisotropy is reduced in selective bits so that they are switched by the in-plane current. To increase stability, the anisotropy in all other bits can be increased by applying an opposite voltage. No substantial current flows through the dielectric barrier at any point in time, making this a unique MRAM application.

Magnetic domain wall motion devices could also greatly benefit from electric field effects, as shown in this thesis. Voltage control of the domain wall velocity over an order of magnitude was demonstrated. Comparison to the literature suggests that control over many orders of magnitude is feasible. This offers exciting new possibilities to the field of spintronics, clearing the way for novel device concepts utilising domain wall motion. The memory device sketched in Fig. 1.7, for example, could revitalise research into racetrack memory.

Bibliography

[1] M. N. Baibich, J. M. Broto, A. Fert, F. Nguyen Van Dau, F. Petroff, P. Etienne, G. Creuzet, A. Friederich, and J. Chazelas. Giant magnetoresistance of (001)Fe/(001)Cr magnetic superlattices. *Phys. Rev. Lett.*, 61:2472--2475, Nov 1988.

[2] G. Binasch, P. Grünberg, F. Saurenbach, and W. Zinn. Enhanced magnetoresistance in layered magnetic structures with antiferromagnetic interlayer exchange. *Phys. Rev. B*, 39:4828--4830, Mar 1989.

[3] Masahiko Nakayama, Tadashi Kai, Naoharu Shimomura, Minoru Amano, Eiji Kitagawa, Toshihiko Nagase, Masatoshi Yoshikawa, Tatsuya Kishi, Sumio Ikegawa, and Hiroaki Yoda. Spin transfer switching in TbCoFe/CoFeB/MgO/CoFeB/TbCoFe magnetic tunnel junctions with perpendicular magnetic anisotropy. *Journal of Applied Physics*, 103(7):07A710, 2008.

[4] W. J. Gallagher and S. S. P. Parkin. Development of the magnetic tunnel junction MRAM at IBM: From first junctions to a 16-Mb MRAM demonstrator chip. *IBM Journal of Research and Development*, 50(1):5 --23, Jan 2006.

[5] S. A. Wolf, A. Y. Chtchelkanova, and D. M. Treger. Spintronics; a retrospective and perspective. *IBM Journal of Research and Development*, 50(1):101--110, jan. 2006.

[6] Stuart S. P. Parkin, Masamitsu Hayashi, and Luc Thomas. Magnetic domain-wall racetrack memory. *Science*, 320(5873):190--194, 2008.

[7] L. Thomas and S. Parkin. Current induced domain-wall motion in magnetic nanowires. *Handbook of Magnetism and Advanced Magnetic Materials*, 2(9-12):1363--1367, 2007.

[8] D. A. Allwood, G. Xiong, C. C. Faulkner, D. Atkinson, D. Petit, and R. P. Cowburn. Magnetic domain-wall logic. *Science*, 309(5741):1688--1692, 2005.

[9] T. Maruyama, Y. Shiota, T. Nozaki, K. Ohta, N. Toda, M. Mizuguchi, A.A. Tulapurkar, T. Shinjo, M. Shiraishi, S. Mizukami, Y. Ando, and Y. Suzuki. Large voltage-induced magnetic anisotropy change in a few atomic layers of iron. *Nat. Nano*, 4:158--161, 2009.

[10] Y. Shiota, T. Nozaki, F. Bonell, S. Murakami, T. Shinjo, and Y. Suzuki. Induction of coherent magnetization switching in a few atomic layers of FeCo using voltage pulses. *Nat. Mater.*, 11:39--43, 2012.

[11] A.D. Kent. Spintronics: Perpendicular all the way. *Nat. Mater.*, 9:699--700, 2010.

[12] J.C. Slonczewski. Current-driven excitation of magnetic multilayers. *Journal of Magnetism and Magnetic Materials*, 159(1-2):L1--L7, 1996.

[13] I.L. Prejbeanu, M. Kerekes, R.C. Sousa, H. Sibuet, O. Redon, B. Dieny, and J.P. NoziÃšres. Thermally assisted MRAM. *Journal of Physics Condensed Matter*, 19(16), 2007.

[14] H. Ohno, D. Chiba, F. Matsukura, T. Omiya, E. Abe, T. Dietl, Y. Ohno, and K. Ohtani. Electric-field control of ferromagnetism. *Nature*, 408:944--946, December 2000.

[15] Yoichi Shiota, Shinichi Murakami, Frédéric Bonell, Takayuki Nozaki, Teruya Shinjo, and Yoshishige Suzuki. Quantitative evaluation of voltage-induced magnetic anisotropy change by magnetoresistance measurement. *Applied Physics Express*, 4(4):043005, 2011.

[16] Martin Weisheit, Sebastian Fahler, Alain Marty, Yves Souche, Christiane Poinsignon, and Dominique Givord. Electric field-induced modification of magnetism in thin-film ferromagnets. *Science*, 315(5810):349--351, 2007.

[17] Yoichi Shiota, Takuto Maruyama, Takayuki Nozaki, Teruya Shinjo, Masashi Shiraishi, and Yoshishige Suzuki. Voltage-assisted magnetization switching in ultrathin $Fe_{80}Co_{20}$ alloy layers. *Applied Physics Express*, 2(6):063001, 2009.

[18] T. Nozaki, Y. Shiota, M. Shiraishi, T. Shinjo, and Y. Suzuki. Voltage-induced perpendicular magnetic anisotropy change in magnetic tunnel junctions. *Applied Physics Letters*, 96(2):022506, 2010.

[19] M. Endo, S. Kanai, S. Ikeda, F. Matsukura, and H. Ohno. Electric-field effects on thickness dependent magnetic anisotropy of sputtered $MgO/Co_{40}Fe_{40}B_{20}/Ta$ structures. *Applied Physics Letters*, 96(21):212503, 2010.

[20] C Fowley, K Rode, K Oguz, H Kurt, and J M D Coey. Electric field induced changes in the coercivity of a thin-film ferromagnet. *Journal of Physics D: Applied Physics*, 44(30):305001, 2011.

[21] F. Bonell, S. Murakami, Y. Shiota, T. Nozaki, T. Shinjo, and Y. Suzuki. Large change in perpendicular magnetic anisotropy induced by an electric field in FePd ultrathin films. *Applied Physics Letters*, 98(23):232510, 2011.

[22] Mikhail Zhernenkov, M. R. Fitzsimmons, Jerzy Chlistunoff, Jaroslaw Majewski, Ioan Tudosa, and E. E. Fullerton. Electric-field modification of magnetism in a thin CoPd film. *Phys. Rev. B*, 82:024420, Jul 2010.

[23] Tiejun Zhou, S. H. Leong, Z. M. Yuan, S. B. Hu, C. L. Ong, and B. Liu. Manipulation of magnetism by electrical field in a real recording system. *Applied Physics Letters*, 96(1):012506, 2010.

[24] S.P. Parkin, C. Kaiser, A. Panchula, P.M. Rice, B. Hughes, M. Samant, and S. Yang. Giant tunnelling magnetoresistance at room temperature with MgO(100) tunnel barriers. *Nat. Mater.*, 3:862--867, 2004.

[25] S. Yuasa, T. Nagahama, A. Fukushima, Y. Suzuki, and K. Ando. Giant room-temperature magnetoresistance in single-crystal Fe/MgO/Fe magnetic tunnel junction. *Nat. Mater.*, 3:868--871, 2004.

[26] W. Wang, M. Li, S. Hageman, and C.L. Chien. Electric-field-assisted switching in magnetic tunnel junctions. *Nat. Mater.*, 11:64--68, 2012.

[27] C. Burrowes, D. Ravelosona, C. Chappert, S. Mangin, Eric E. Fullerton, J. A. Katine, and B. D. Terris. Role of pinning in current driven domain wall motion in wires with perpendicular anisotropy. *Applied Physics Letters*, 93(17):172513, 2008.

[28] T. A. Moore, I. M. Miron, G. Gaudin, G. Serret, S. Auffret, B. Rodmacq, A. Schuhl, S. Pizzini, J. Vogel, and M. Bonfim. High domain wall velocities induced by current in ultrathin Pt/Co/AlOx wires with perpendicular magnetic anisotropy. *Applied Physics Letters*, 93(26):262504, 2008.

[29] I.M. Miron, T. Moore, H. Szambolics, L.D. Buda-Prejbeanu, S. Auffret, B. Rodmacq, S. Pizzini, J. Vogel, M. Bonfim, A. Schuhl, and G. Gaudin. Fast current-induced domain-wall motion controlled by the Rashba effect. *Nat. Mater.*, 10:419--423, Jun 2011.

[30] P. Bruno. *Magnetismus von Festkörpern und grenzflächen*. Forschungszentrum Jülich, 1993. Physical origins and theoretical models of magnetic anisotropy.

[31] J. Stöhr and H.C. Siegmann. *Magnetism, from fundamentals to nanoscale dynamics*. Springer, 2006.

[32] G. H. O. Daalderop, P. J. Kelly, and M. F. H. Schuurmans. First-principles calculation of the magnetocrystalline anisotropy energy of iron, cobalt, and nickel. *Phys. Rev. B*, 41:11919--11937, Jun 1990.

[33] J. H. van Vleck. On the anisotropy of cubic ferromagnetic crystals. *Phys. Rev.*, 52:1178--1198, Dec 1937.

[34] J. Stöhr. Exploring the microscopic origin of magnetic anisotropies with X-ray magnetic circular dichroism (XMCD) spectroscopy. *Journal of Magnetism and Magnetic Materials*, 200(1-3):470--497, 1999.

[35] G. H. O. Daalderop, P. J. Kelly, and M. F. H. Schuurmans. Magnetic anisotropy of a free-standing Co monolayer and of multilayers which contain Co monolayers. *Phys. Rev. B*, 50:9989--10003, Oct 1994.

[36] Ding sheng Wang, Ruqian Wu, and A.J Freeman. Magnetocrystalline anisotropy of interfaces: first-principles theory for Co-Cu interface and interpretation by an effective ligand interaction model. *Journal of Magnetism and Magnetic Materials*, 129(2-3):237--258, 1994.

[37] Patrick Bruno. Tight-binding approach to the orbital magnetic moment and magnetocrystalline anisotropy of transition-metal monolayers. *Phys. Rev. B*, 39:865--868, Jan 1989.

[38] B. Újfalussy, L. Szunyogh, P. Bruno, and P. Weinberger. First-principles calculation of the anomalous perpendicular anisotropy in a Co monolayer on Au(111). *Phys. Rev. Lett.*, 77:1805--1808, Aug 1996.

[39] Chun-Gang Duan, Julian P. Velev, R. F. Sabirianov, Ziqiang Zhu, Junhao Chu, S. S. Jaswal, and E. Y. Tsymbal. Surface magnetoelectric effect in ferromagnetic metal films. *Phys. Rev. Lett.*, 101:137201, Sep 2008.

[40] J. G. Gay and Roy Richter. Spin anisotropy of ferromagnetic films. *Phys. Rev. Lett.*, 56:2728--2731, Jun 1986.

[41] Chun Li, A. J. Freeman, H. J. F. Jansen, and C. L. Fu. Magnetic anisotropy in low-dimensional ferromagnetic systems: Fe monolayers on Ag(001), Au(001), and Pd(001) substrates. *Phys. Rev. B*, 42:5433--5442, Sep 1990.

[42] G. H. O. Daalderop, P. J. Kelly, and M. F. H. Schuurmans. Magnetocrystalline anisotropy and orbital moments in transition-metal compounds. *Phys. Rev. B*, 44:12054--12057, Dec 1991.

[43] Kentaro Kyuno, Jae-Geun Ha, Ryoichi Yamamoto, and Setsuro Asano. First-principles calculation of the magnetic anisotropy energies of Ag/Fe(001) and Au/Fe(001) multilayers. *Journal of the Physical Society of Japan*, 65(5):1334--1339, 1996.

[44] Shufeng Zhang. Spin-dependent surface screening in ferromagnets and magnetic tunnel junctions. *Phys. Rev. Lett.*, 83:640--643, Jul 1999.

[45] Masahito Tsujikawa and Tatsuki Oda. Finite electric field effects in the large perpendicular magnetic anisotropy surface Pt/Fe/Pt 001: A first-principles study. *Phys. Rev. Lett.*, 102:247203, Jun 2009.

[46] Kohji Nakamura, Riki Shimabukuro, Yuji Fujiwara, Toru Akiyama, Tomonori Ito, and A. J. Freeman. Giant modification of the magnetocrystalline anisotropy in transition-metal monolayers by an external electric field. *Phys. Rev. Lett.*, 102:187201, May 2009.

[47] Y. Suzuki, H. Kubota, A. Tulapurkar, and T. Nozaki. Spin control by application of electric current and voltage in FeCo-MgO junctions. *Phil. Trans. R. Soc. A*, 369:3658--3678, 2011.

[48] Klaus Schröder. Stress operated random access, high-speed magnetic memory. *Journal of Applied Physics*, 53(3):2759--2761, 1982.

[49] V. Novosad, Y. Otani, A. Ohsawa, S. G. Kim, K. Fukamichi, J. Koike, K. Maruyama, O. Kitakami, and Y. Shimada. Novel magnetostrictive memory device. *Journal of Applied Physics*, 87(9):6400--6402, 2000.

[50] J. Hemberger, P. Lunkenheimer, R. Fichtl, H.-A. Krug von Nidda, V. Tsurkan, and A. Loidl. Relaxor ferroelectricity and colossal magnetocapacitive coupling in ferromagnetic $CdCr_2S_4$. *Nature*, 434:364--367, 2005.

[51] N. Hur, S. Park, P. A. Sharma, J. S. Ahn, S. Guha, and S-W. Cheong. Electric polarization reversal and memory in a multiferroic material induced by magnetic fields. *Nature*, 429:392--395, 2004.

[52] W. Eerenstein, N. D. Mathur, and J. F. Scott. Multiferroic and magnetoelectric materials. *Nature*, 442:759--765, 2006.

[53] Sarbeswar Sahoo, Srinivas Polisetty, Chun-Gang Duan, Sitaram S. Jaswal, Evgeny Y. Tsymbal, and Christian Binek. Ferroelectric control of magnetism in $BaTiO_3Fe$ heterostructures via interface strain coupling. *Phys. Rev. B*, 76:092108, Sep 2007.

[54] Tuomas H. E. Lahtinen, Kévin J. A. Franke, and Sebastiaan van Dijken. Electric-field control of magnetic domain wall motion and local magnetization reversal. *Sci. Rep.*, 2, 2012.

[55] T. Dietl, H. Ohno, F. Matsukura, J. Cibert, and D. Ferrand. Zener model description of ferromagnetism in zinc-blende magnetic semiconductors. *Science*, 287(5455):1019--1022, 2000.

[56] D. Chiba, M. Yamanouchi, F. Matsukura, and H. Ohno. Electrical manipulation of magnetization reversal in a ferromagnetic semiconductor. *Science*, 301(5635):943--945, 2003.

[57] D. Chiba, M. Sawicki, Y. Nishitani, Y. Nakatani, F. Matsukura, and H. Ohno. Magnetization vector manipulation by electric fields. *Nature*, 455:515--518, 2008.

[58] E. C. Stoner and E. P. Wohlfarth. A mechanism of magnetic hysteresis in heterogeneous alloys. *Phil. Trans. R. Soc. Lond. A*, 240(826):599--642, 1948.

[59] L. Berger. Exchange interaction between ferromagnetic domain wall and electric current in very thin metallic films. *Journal of Applied Physics*, 55(6):1954--1956, 1984.

[60] P. J. Metaxas, J. P. Jamet, A. Mougin, M. Cormier, J. Ferré, V. Baltz, B. Rodmacq, B. Dieny, and R. L. Stamps. Creep and flow regimes of magnetic domain-wall motion in ultrathin Pt/Co/Pt films with perpendicular anisotropy. *Phys. Rev. Lett.*, 99:217208, Nov 2007.

[61] G. Blatter, M. V. Feigelman, V. B. Geshkenbein, A. I. Larkin, and V. M. Vinokur. Vortices in high-temperature superconductors. *Rev. Mod. Phys.*, 66:1125--1388, Oct 1994.

[62] S. Lemerle, J. Ferré, C. Chappert, V. Mathet, T. Giamarchi, and P. Le Doussal. Domain wall creep in an ising ultrathin magnetic film. *Phys. Rev. Lett.*, 80:849--852, Jan 1998.

[63] P.R. LeClair. *Fundamental aspects of Spin Polarized Tunneling*. PhD thesis, Technische Universiteit Eindhoven, 2002.

[64] Susumu Shibata. Dielectric constants of Ta_2O_5 thin films deposited by r.f. sputtering. *Thin Solid Films*, 277(1-2):1--4, 1996.

[65] M Voigt and M Sokolowski. Electrical properties of thin rf sputtered aluminum oxide films. *Materials Science and Engineering B*, 109(1-3):99--103, 2004.

[66] S. Monso, B. Rodmacq, S. Auffret, G. Casali, F. Fettar, B. Gilles, B. Dieny, and P. Boyer. Crossover from in-plane to perpendicular anisotropy in Pt/CoFe/AlOx sandwiches as a function of al oxidation: A very accurate control of the oxidation of tunnel barriers. *Applied Physics Letters*, 80(22):4157--4159, 2002.

[67] A. Manchon, C. Ducruet, L. Lombard, S. Auffret, B. Rodmacq, B. Dieny, S. Pizzini, J. Vogel, V. Uhlíř, M. Hochstrasser, and G. Panaccione. Analysis of oxygen induced anisotropy crossover in Pt/Co/MOx trilayers. *Journal of Applied Physics*, 104(4):043914, 2008.

[68] Farid Fettar, Houmed Garad, Luc Ortega, Aline Y. Ramos, Bartosz Zawilski, Philippe Plaindoux, Stephane Auffret, Bernard Rodmacq, and Bernard Dieny. Investigation of metallic/oxide interfaces in Pt/Co/AlOx trilayers by hard x-ray reflectivity. *IEEE Transactions on Magnetics*, 45(10):3905--3908, 2009.

[69] C.A.M. Knechten. *Plasma Oxidation for Magnetic Tunnel Junctions*. PhD thesis, Technische Universiteit Eindhoven, 2005.

[70] Chun-Yeol You. Critical current density for spin transfer torque switching with composite free layer structure. *Current Applied Physics*, 10(3):952 -- 956, 2010.

[71] Manish K. Niranjan, Chun-Gang Duan, Sitaram S. Jaswal, and Evgeny Y. Tsymbal. Electric field effect on magnetization at the fe/mgo(001) interface. *Applied Physics Letters*, 96(22):222504, 2010.

[72] Ioan Mihai Miron, Kevin Garello, Gilles Gaudin, Pierre-Jean Zermatten, Marius V. Costache, Stephane Auffret, Sebastien Bandiera, Bernard Rodmacq, Alain Schuhl, and Pietro Gambardella. Perpendicular switching of a single ferromagnetic layer induced by in-plane current injection. *Nature*, 476:189--193, 2011.

[73] Francis J. Arlinghaus and Ruth A. Reck. Calculations of the electronic spin and orbital magnetic moments and g' in ferromagnetic nickel. *Phys. Rev. B*, 11:3488--3490, May 1975.

Acknowledgements

Here, I would like to thank some people who have supported me throughout this project, both scientifically and on a personal level.

First of all, I would like to thank my daily supervisor, Sjors Schellekens, for all his invaluable help. Your intuitive grasp of physics, combined with your patient and helpful nature, make you an excellent mentor. I've greatly enjoyed our many discussions, on topics of varying scientific degree. Thank you also for shaping this project and writing an excellent paper based on our work, which will surely prove to be of high impact.

Second, I would like to express my gratitude to Bert Koopmans for supervising this project. Your feedback during key stages helped to keep the research on track, and your expertise in many areas of solid state physics was crucial in designing and understanding experiments. The same is true for Henk Swagten, who continuously showed great interest in my work and was always available for comments and advice. Thank you both, also, for creating a great atmosphere for research at FNA.

I've had the pleasure of discussing many scientific topics with various other member of the group. Jeroen Franken was always willing to share some of his knowledge on domain wall motion. I'd like to thank Jürgen Kohlhepp for providing useful advice in the areas of materials research and experimental techniques. Thanks also to Pascal Haazen, for many interesting discussions and sharing some griefs. Also, I'd like to thank all other members of the FNA research group, especially my fellow graduate students, for good times both inside and outside the university.

Special thanks to Jeroen Francke and Gerrie Baselmans, for keeping the equipment running and helping me with practical issues.

Finally, many thanks to my family and friends for supporting me during my graduation. I would like to show my appreciation for my parents, for their warmth and encouragements. I can never thank you both enough. Also, thank you Simone, for being so kind and optimistic.

Appendix A

Band structure

The ligand field model discussed in section 2.1.2.3 describes only one atom in terms of its orbitals; the orbital structure of ligands is neglected. Furthermore, orbitals are regarded merely as spatial charge distributions, whereas orbitals are in fact electron wave functions carrying a sign and a phase. A more appropriate way of describing interacting valence electrons is the *molecular orbital model*, which is an ab-initio model that describes overlap and mixing of bonding electron wavefunctions.

Valence electrons in metals experience a periodic potential extending over the entire lattice, rather than a single radial potential caused by the atomic nucleus. In a *tight binding* approach, the electron wavefunctions are approximated as superpositions of atomic orbitals with a periodically varying phase. In one dimension, such a *Bloch function* is mathematically described as

$$\phi_j(k) = \sum_n d_j^{(n)} \cdot e^{i \cdot n \cdot k \cdot a},$$

where a is the interatomic distance and $d_j^{(n)}$ is a specific orbital d_j (e.g. d_{xy}) on atom n. From this formula it is evident that electrons states with $k = 0$ consist of in-phase atomic orbitals, whereas states with $k = \pi/a$ (the edge of the Brillouin zone) consist of 180º out-of-phase neighbouring orbitals.

Recalling that atomic orbitals consist of positive and negative lobes, a 180º phase shift implies switching the sign of each lobe. This phase shift is visualised in Fig. A.1 for a one-dimensional chain of $d_{3z^2-r^2}$ orbitals. The $k = 0$ Bloch function is a *bonding* state: overlapping lobes are of the same sign, and the total energy is reduced due to the increased electron density between the nuclei. The $k = \pi/a$ superposition, on the other hand, is an *anti-bonding* state: overlapping lobes are of opposite sign, and the total energy is increased due to the decreased electron density between the nuclei. Similar k-dependencies arise for the Bloch functions of other atomic orbitals, giving rise to *band structure*.

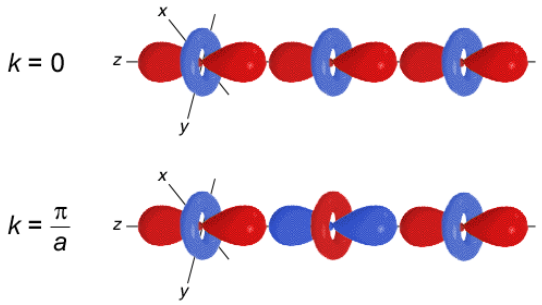

Figure A.1: *Chain of $d_{3z^2-r^2}$ orbitals along the z axis. The blue (red) colouring depicts positive (negative) sign of the wavefunction.*

Full calculation of the two- or three-dimensional band structure is a complex task, requiring full quantum-mechanical evaluation of wavefunction energies in a periodic potential (see section 2.2.2). Here, the band structure for a free-standing Co monolayer is taken from the literature [35], shown in Fig. A.2b. The wave vector is varied along lines connecting characteristic points in the first Brillouin zone (BZ) for a two-dimensional hexagonal lattice: Γ (centre of BZ), K (hexagon corner point), and M (middle of hexagon edge). Both the majority and minority spin bands are depicted; the majority band is nearly filled as almost all states lie below the Fermi level. Note that the depicted DOS is for the Co [111] plane, which is slightly different from the Co [100] DOS mentioned in section 2.1.2.4.

More insight is gained by reviewing the density of states (DOS), separated into orbital contributions, as shown in Fig A.2a. It turns out that first-principles band structure calculations support the idea of anisotropic bonding: clearly, the 'out-of-plane' orbitals $d_{3z^2-r^2}$, d_{xz}, and d_{yz} have a narrow bandwidth compared to the 'in-plane' orbitals $d_{x^2-y^2}$ and d_{xy}.

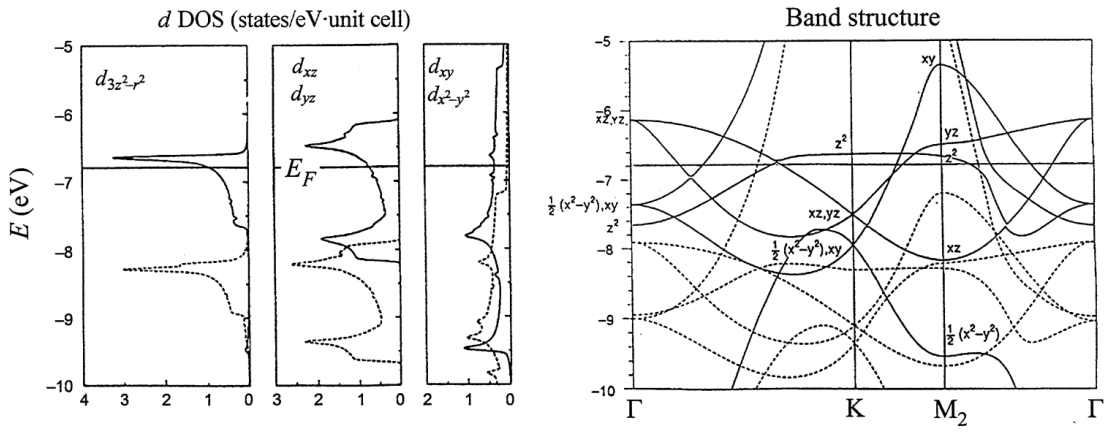

Figure A.2: *Density of states and band structure of a free-standing Co [111] monolayer, as calculated by Daalderop et al. [35]. The Fermi level is indicated by a solid line. (a) Orbital projected density of states for majority spins (dashed) and minority spins (solid). The 'out-of-plane' orbitals $d_{3z^2-r^2}$, d_{xz}, and d_{yz} have a narrow bandwidth compared to the 'in-plane' orbitals $d_{x^2-y^2}$ and d_{xy}. (b) Band structure for majority (dashed) and minority (solid) spins.*

Appendix B

Orbital momentum operators

The orbital momentum operators for the 3d orbitals were taken from [73]. Define the following basis of $3d$ orbitals:

$$\begin{bmatrix} d_{xy} \\ d_{yz} \\ d_{xz} \\ d_{x^2-y^2} \\ d_{3z^2-r^2} \end{bmatrix}. \tag{B.1}$$

The orbital momentum operators are then given by:

$$\hat{L_x} = \hbar \begin{bmatrix} 0 & 0 & -i & 0 & 0 \\ 0 & 0 & 0 & -i & -i\sqrt{3} \\ i & 0 & 0 & 0 & 0 \\ 0 & i & 0 & 0 & 0 \\ 0 & i\sqrt{3} & 0 & 0 & 0 \end{bmatrix}, \tag{B.2}$$

$$\hat{L_y} = \hbar \begin{bmatrix} 0 & i & 0 & 0 & 0 \\ -i & 0 & 0 & 0 & 0 \\ 0 & 0 & 0 & -i & i\sqrt{3} \\ 0 & 0 & i & 0 & 0 \\ 0 & 0 & -i\sqrt{3} & 0 & 0 \end{bmatrix}, \tag{B.3}$$

$$\hat{L_z} = \hbar \begin{bmatrix} 0 & 0 & 0 & 2i & 0 \\ 0 & 0 & i & 0 & 0 \\ 0 & -i & 0 & 0 & 0 \\ -2i & 0 & 0 & 0 & 0 \\ 0 & 0 & 0 & 0 & 0 \end{bmatrix}. \tag{B.4}$$

Appendix C

Pt / Co wedge / AlOx results

The effect of changing the dielectric layer on the thickness-dependent properties of the magnetic layer has been examined. The magnetic characteristics of the fabricated Pt (4 nm) / Co (0-2 nm) / Al_2O_3 (1.5 nm) wedge are presented in Fig. C.1. Comparison between the Al and Ta top layers (Fig. C.1. vs Fig. 4.4) raises several problems:

- The range over which the sample exhibits PMA is decreased considerably by using Al as a top layer. Furthermore, the onset of magnetic behaviour is shifted towards a lower Co thickness by approximately 0.2 nm. A possible explanation for this is that 1.4 nm of Ta is less effective at shielding oxygen atoms during the oxidation process than 1.5 nm of Al, making the effective intact magnetic layer thinner. This does, however, seem to contradict the results shown in section 4.1.1.
- Replacing Ta with Al significantly decreases the coercivity and remanence, especially in the as-deposited sample. Again, this contradicts the conclusions drawn from the dielectric wedges (section 4.1.1).
- The particular point Pt (4 nm) / Co (1 nm) / Al_2O_3 (1.5 nm) also occurs in the dielectric layer thickness experiment, but comparison between Fig. 4.1 and Fig. C.1 shows significant differences in magnetic behaviour.

The explanation for these discrepancies is twofold. First, the samples were deposited in different runs, months apart, so changes in the condition of the sputtering system could have affected precise the layer thickness and quality. Second, it is possible that interactions within the wedge affect the experimental outcomes. Domain wall motion, for instance, may lead to underestimation of the coercivity. For this reason, wedge results can show inconsistencies when compared to different wedges, uniform films, or junctions. Due to the substantial inconsistencies between this particular dataset and other results, it has been excluded from the analysis in section 1.3.1.

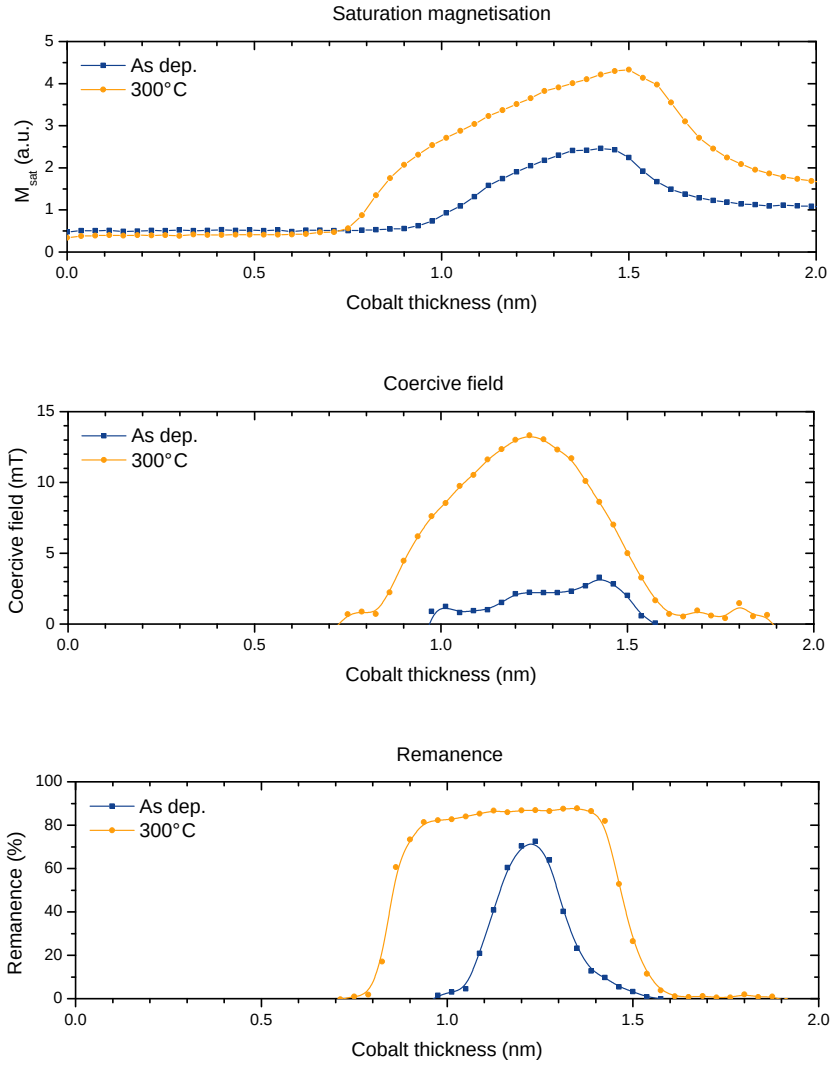

Figure C.1: *Magnetic properties of a Pt (4 nm) / Co (0-2 nm) / Al_2O_3 (1.5 nm) wedge (sample C1111027).*

Appendix D

Domain wall motion MOKE curve simulation

A phenomenon frequently observed in hysteresis loops measured using laser MOKE is *slanting*. The magnetisation is seen to switch gradually, causing easy-axis hysteresis loops to look like parallelograms rather than squares. Interestingly, the amount of slanting was found to depend on the applied voltage in some measurements, as shown in Fig. D.1. This effect can also been seen in several publications by other researchers [21, 56, 19, 53], but has not been explained before.

After establishing that magnetisation reversal in our samples occurs through domain wall creep, it was suspected that this process causes the observed slanting. Analysis of this domain wall motion yields a detailed relation between the domain wall creep velocity and the applied electric and magnetic field, as described in section 4.4. This information was subsequently used as input for a simple one-dimensional numerical model, simulating the observed MOKE signal during magnetisation reversal.

The perpendicular magnetization m_z of the sample is assumed to depend solely on the domain wall position x, where $-w/2 \leq x \leq w/2$ with $w = 120\,\mu$m the width of the magnetic region in a specific sample, so that reversal of the junction is simplified to a one-dimensional problem. The basics of this one-dimensional model are depicted in Fig. D.2. Domain walls appear as error functions propagating from either side of the junction towards the centre. The irregularity of the domain wall is expressed in the width of this error function. For each time step, the velocity $v(x, B, V)$ is given by the DW creep law (Eq. 4.1 with $c = c(x)$), using parameter values derived directly from experiments. The resulting MOKE signal is simulated by multiplying $m_z(x)$ with a Gaussian laser spot and integrating over x. The laser spot is given a full-width-at-half-maximum of 15 μm and is centred around $x = 0$, similar to real experiments.

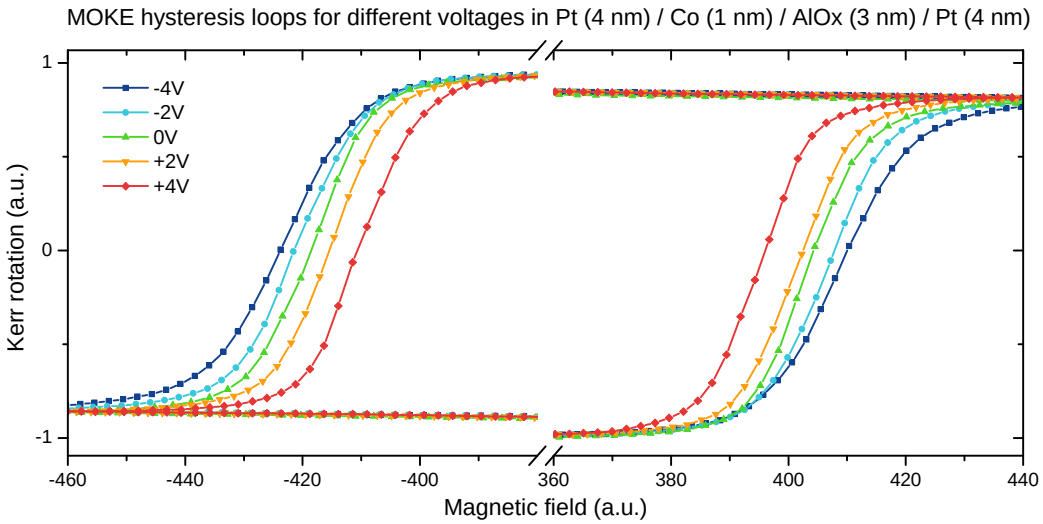

Figure D.1: *Magnetic hysteresis curves measured using a magnetic field at a small angle to the sample surface. An positive (negative) applied voltage is clearly seen to decrease (increase) the coercivity. Furthermore, the amount of slanting increases with increased coercivity.*

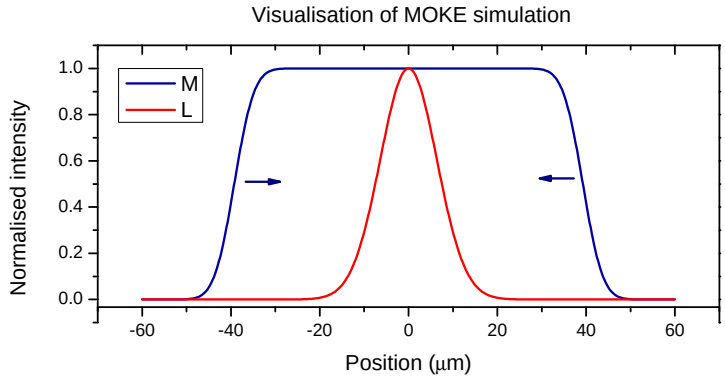

Figure D.2: *Graphical representation of the developed MOKE simulation. The magnetisation M varies between 0, switched, and 1, not switched. Two domain walls are represented as error functions, where the width represents the irregularity of the wall over the integrated dimension. The velocity of the domain walls is given by an empirical function $v(x, B, V)$ based on the creep law and the experimentally observed velocity profile across the junction. The laser spot is represented by a Gaussian function L. Note that the integral of a 2D Gaussian over one dimension is also a Gaussian.*

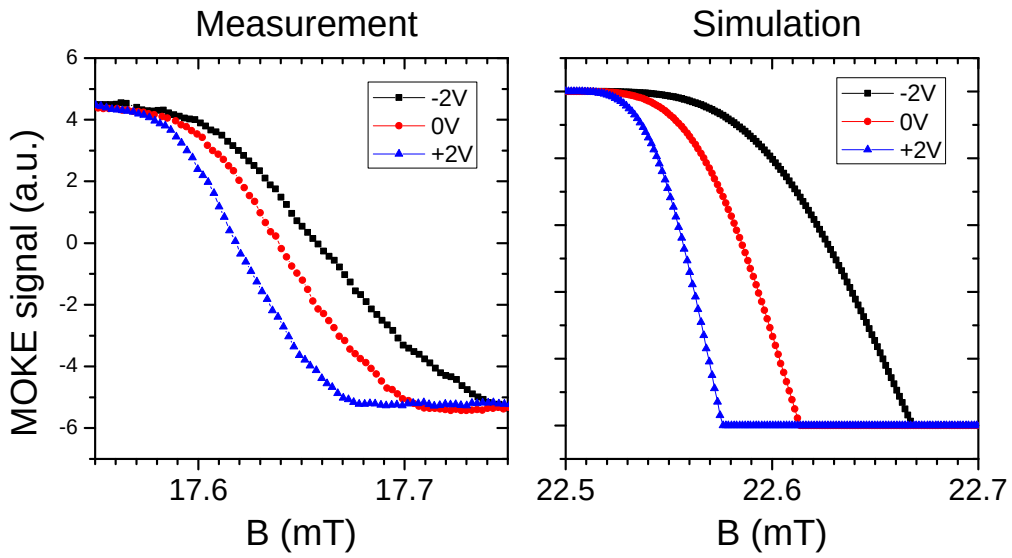

Figure D.3: *Magnetic switching process as measured using MOKE in a typical junction, compared to a simulation of this switching using the described model.*

Typical switching curves obtained in an experiment are compared to the simulation result in Fig. D.3. The observed voltage-induced coercivity modification and slanting are clearly reproduced. The mismatch in coercive field is caused by the domain wall nucleation process, which is difficult to account for in the model. Also, the transition is much sharper in the simulation; the one-dimensional error function description does not describe the annihilation process of the two walls correctly.

The observed MOKE trace can be modified by varying the experimental parameters of the simulation. The observed coercivity, voltage-induced coercivity modification, and the amount of slanting all depend on the magnetic field sweeping procedure and the position of the laser spot on the sample.

The effect of changing the magnetic field sweeping *rate* is demonstrated in Fig. D.4. The coercivity is seen to decrease with decreasing sweep rate. This is due to domain wall creep motion: in a constant (or slowly increasing) magnetic field, switching still occurs if the system is given enough time due to thermal activation. The magnetic state is thus a function of both the applied magnetic field and the elapsed time, making the coercive field a poor observable.

The effect of changing the magnetic field sweeping *range* is demonstrated in Fig. D.5. In a typical experiment, it is tempting to reduce the field sweep

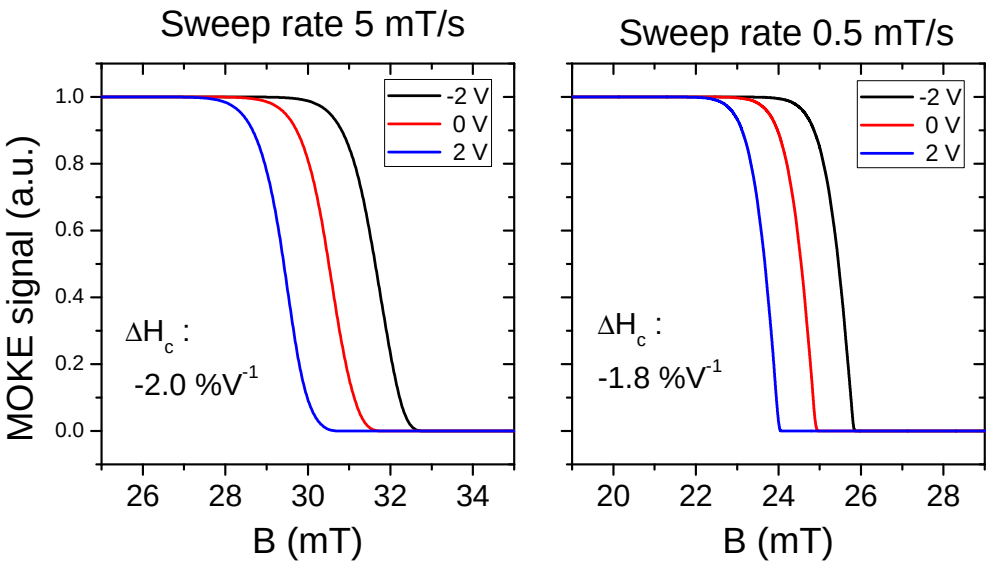

Figure D.4: *Simulated MOKE curves for two different magnetic field sweeping rates. The observed coercivity is seen to decrease with decreasing sweep rate. The magnitude of the relative electric field induced coercivity modification is also slightly affected.*

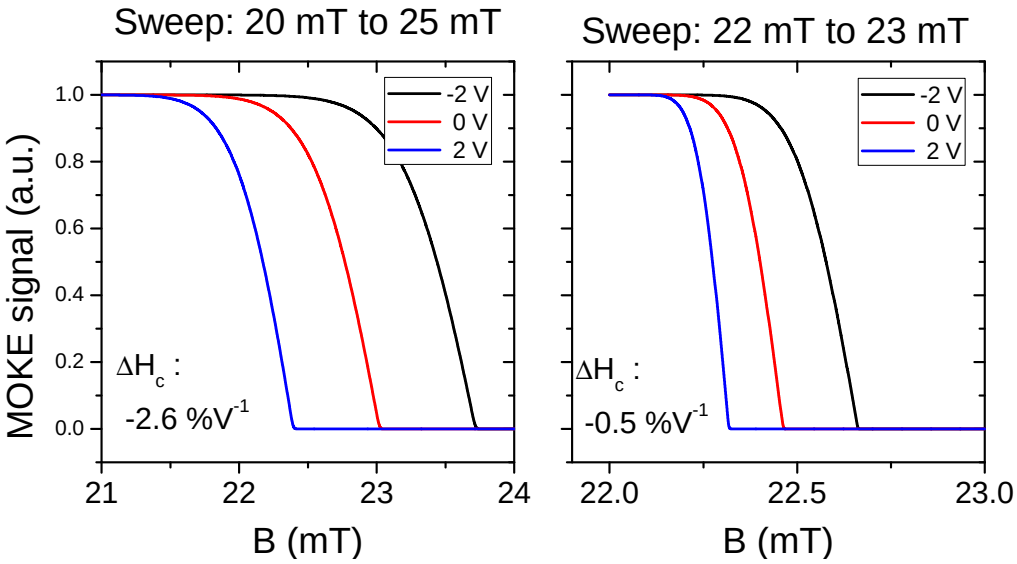

Figure D.5: *Simulated MOKE curves for two different magnetic field sweeping ranges. Reducing the sweeping range has a profound effect on the observed voltage-induced coercivity modification: it becomes much smaller and non-linear with respect to the applied voltage.*

range to a narrow window around the coercive field, to increase the resolution and decrease measurement times. However, adjusting the sweep range is seen to have a strong impact on the observed switching behaviour. Complete reversal of the magnetisation can be observed in any arbitrary field window, if one simply waits long enough for domain walls to propagate across the junction due to thermally activated creep motion. Changing the magnetic field sweeping range thus changes the observed coercivity. The magnitude of the apparent electric field effect is also strongly affected. Furthermore, the observed coercivity modification becomes asymmetric with respect to the applied voltage due to the slanting effect. All these effects indicate that the magnetic state is a function of both the applied magnetic field and the elapsed time. If such effects are seen in a MOKE measurement, the coercivity should not be used as a quantitative characteristic of the magnetisation reversal process.

Appendix E

Stoner-Wohlfarth fitting example

The magnetic anisotropy of a sample can be computed from MOKE measurements using the Stoner-Wohlfarth model as described in section 2.3.1. This method was employed to estimate the anisotropy in several samples. A typical measurement is shown in Fig. E.1, in this case for the Pt (4 nm) / CoB (1 nm) / TaOx (7 nm) / Pt (4 nm) junction (not annealed) described in section 4.6. The data can be fitted with reasonable accuracy, yielding a value for the total anisotropy constant K_{eff}.

The MOKE measurement is found to deviate from Stoner-Wohlfarth behaviour for smaller angles (where the applied field is closer to easy axis), which is caused by an increasingly large Faraday rotation (a non-linear background effect). Note that samples with a higher magnetic anisotropy are more difficult to analyse; a smaller portion of the curve can be recorded due to magnetic field strength limitations.

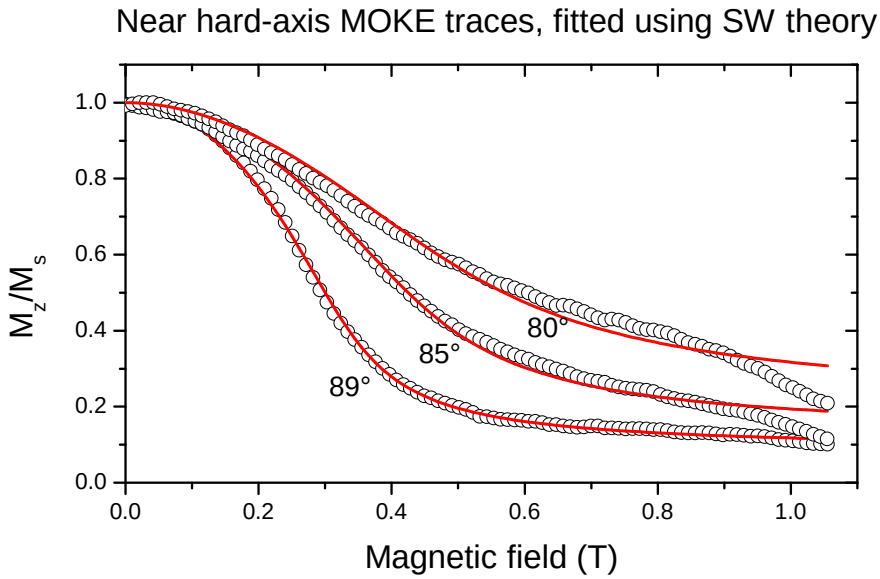

Figure E.1: *Normalised magnetisation as a function of applied magnetic field, as measured using polar MOKE (open circles) and fitted using the Stoner-Wohlfarth model (red lines). The angle of the applied field relative to the (out-of-plane) easy axis is indicated for each trace. The fit is seen to be most accurate for the largest angle.*